University of Pisa

SCUOLA DI DOTTORATO IN SCIENZE CHIMICHE E DEI MATERIALI

XXIX CICLO

Ph.D. Thesis
Carbon nanomaterials for sensing of volatile amines

Tutor:
Dr. Fabio Di Francesco

Candidate:
Clara Paoletti

External referees:
Prof. Timothy M. Swager
Prof. Abdelhamid Errachid

Table of Contents

Abbreviations

°C	degree Celsius
Å	Ångström
a_1	unit vectors along the zigzag carbon bond of the hexagon lattice of the graphene sheet
a_2	unit vectors along the zigzag carbon bond of the hexagon lattice of the graphene sheet
AFM	atomic force microscopy
C	carbon
C_h	chiral vector
$CHCl_3$	chloroform
cm	centimeter
CNMs	carbon nanomaterials
CNTs	carbon nanotubes
Co	cobalt
Cu	copper
CVD	chemical vapor deposition
DF	degree of functionalization
DGU	density gradient ultracentrifugation
DMA	dimethylamine
DMF	dimethylformamide
DWCNTs	double-walled carbon nanotubes
F	fluorine

FA	formaldehyde
f-CNTs	functionalized carbon nanotubes
Fe	iron
f-G	functionalized graphene
f-MWCNTs	functionalized multi-walled carbon nanotubes
f-rGO	functionalized reduced graphene oxide
f-SWCNTs	functionalized single-walled carbon nanotubes
FT-IR	fourier transform infrared spectroscopy
G	graphene
H_2SO_4	sulfuric acid
HCl	hydrochloric acid
HNO_3	nitric acid
HOMO	highest occupied molecular orbital
HRTEM	high-resolution transmission electron microscopy
I_D	intensity of the D-band
I_G	intensity of the G-band
ITO	indium tin oxide
IUPAC	international union of pure and applied chemistry
K	Kelvin
L	liter
LUMO	lowest unoccupied molecular orbital
m	number of hexagons crossed by the vector
MeOH	methanol

MgSO$_4$	magnesium sulfate
min	minute/minutes
MWCNTs	multi-walled carbon nanotubes
n	number of hexagons crossed by the vector
N	Newton
N$_2$	nitrogen (molecular)
NaBH$_4$	sodium borohydride
NaN$_3$	sodium azide
NaOH	sodium hydroxide
NH$_3$	ammonia
Ni	nichel
nm	nanometer
NMP	N-methyl-2-pyrrolidone
NMR	nuclear magnetic resonance
O	oxygen
o-DCB	1,2-dichlorobenzene
PAH	polyaromatic hydrocarbons
p-CNTs	pristine carbon nanotubes
p-G	pristine graphene
ppm	part per million
p-MWCNTs	pristine multi-walled carbon nanotubes
p-rGO	pristine reduced graphene oxide
p-SWCNTs	pristine single-walled carbon nanotubes

R	resistance
r.t.	room temperature
RFID	Radio-Frequency IDentification
rGO	reduced graphene oxide
RH	relative humidity
rpm	revolutions per minute
s	second/seconds
SEC	size exclusion chromatography
SEM	scanning electron microscope
SiC	silicon carbide
sq	square
SWCNTs	single-walled carbon nanotubes
T	temperature
TEM	transmission electron microscopy
TEWL	transepidermal water loss
TGA	thermogravimetric analyses
TLC	thin-layer chromatography
TMA	trimethylamine
TMAO	trimethylamine N-oxide
TPa	terapascal
TVB-N	total volatile basic nitrogen compounds
UV-Vis-NIR	ultraviolet-visible-near infrared spectroscopy
V	voltage

v	volume
VLUs	venous leg ulcers
wt.	weight
XPS	X-ray photoelectron spectroscopy
θ	chiral angle
Ω	Ohm

N.B. The terms "sample" and "compound" are used alternatively in the text and they have the same meaning.

Introduction

Carbon nanomaterials (CNMs) possess outstanding mechanical and electrical properties. In this thesis, pristine and functionalized carbon nanotubes (CNTs), graphene (G) and reduced graphene oxide (rGO) were exploited to realize resistive chemical sensors for the detection of gaseous ammonia (NH_3) and trimethylamine (TMA).

Pristine CNTs, G and rGO (p-CNTs, p-G and p-rGO, respectively) and functionalized CNTs, G and rGO (f-CNTs, f-G and f-rGO, respectively) were characterized by using different analytical techniques as Raman, TGA, XPS, UV-Vis-NIR, FT-IR, Fluorescence and SEM.

The performance of pristine and functionalized CNMs toward ammonia and trimethylamine detection were evaluated by drop-casting aliquots of CNMs dispersions on glass or FR4 substrates equipped with gold electrodes and then measuring the electrical changes upon exposure of different concentrations of NH_3 or TMA. The changes in resistance of the sensitive materials were quantified and compared with each other.

The necessity to develop a resistive sensor for the detection of ammonia and trimethylamine originates from the exponential growth of the fish trading as a consequence of the impressive consumption of fish and fishery products all over the world occurred in the last few years. In addition to the contribution to the economic activity, the worldwide commercialization of fish considerably improved the request of quality seafood products.

In the European Union (EU), a standard method to assess the freshness of fish was established in 1995 (95/149/EC). After the approval of a regulation for food traceability, which implies the need to assess quality and identify the responsibility of the correct storage along the whole food chain, fisheries industries looked for rapid methods to evaluate real-time freshness of fish and seafood products. In this framework, we aimed to develop a system to monitor the freshness of fish and seafood products basing the research on the development of chemiresistive portable sensors. Fish is among the most perishable flesh food and

the odor is a first indication for freshness, since fish flesh releases increasing amounts of characteristic volatile compounds during degradation, such as ammonia (NH_3) and trimethylamine (TMA). In particular, TMA can be considered a marker for the determination of fish freshness. In fact, when fresh, the nitrogenous compound is present in the fish flesh in the form of trimethylamine N-oxide (TMAO); when the bacterial and enzimatic activity takes place, TMAO is degraded to TMA, dimethylamine (DMA) and formaldehyde (FA) [1]. A general approach to evaluate the freshness of fish is the quantification of the total volatile basic nitrogen compounds (TVB-N) using different methods. The standard method approved by the European Union for the assessment of the freshness of fish is based on the determination of TVB-N levels in fish tissue samples by extracting the volatiles bases by a perchloric acid solution; then the extract is steam distilled, collected in boric acid and titrated against standard HCl. Although this method is reliable and efficient, it is destructive, time-consuming and requires appropriate instrumentation and highly qualified personnel to be performed. Due to the large variability in the spoilage attitude among different species, harvests and fishes of a same catch, the fishing industry and agencies for the food safety have always shown interest in methods for the fast evaluation of fish freshness. Accurate portable devices are needed to measure NH_3 and TMA in the field, as they would help to prevent the degradation of products and allow quality controls at each transfer of product between different actors of the distribution chain. Although ammonia is present even in fresh fish, the TVB-N content produced during the spoilage is very close to that of TMA [2].

When fresh, fish releases up to 10 ppm of TMA, whereas concentrations between 10 and 50 ppm indicate a preliminary rot and concentrations over 60 ppm a rotten product [3,4].

The efforts carried out for the realization of resistive chemical sensors able to detect gaseous amines in real-time led to win a project (MIT-UNIPI Project) titled "Functional Nanomaterials for the Detection of Volatile Amines (FUNDUS)" which was a collaboration between the University of Pisa and the Massachusetts Institute of Technology (Cambridge, MA, USA). Therefore, in this

thesis and in the MIT-UNIPI Project, single-walled carbon nanotubes (SWCNTs), multi-walled carbon nanotubes (MWCNTs), G and rGO were covalently functionalized in order to obtain different materials sensitive to the detection of different concentrations of volatile amines as NH_3 and TMA. Very interesting was the comparison of the performance of the different carbon-based nanomaterials toward two different kind of covalent functionalization carried out exploiting the nitrene and diazonium chemistry and the following submission to gas sensing tests. SWCNTs were also functionalized by non-covalent functionalization and their sensing performance were evaluated.

Appendix I was instead dedicated to the description of a side work carried out in collaboration with the Scuola Superiore Sant'Anna (Pisa, Italy) and the Department of Dermatology, University of Pisa (Pisa, Italy). The work took part within the SWAN i-Care European project. SWAN-iCARE aimed at developing an integrated autonomous device for the monitoring and the personalized management of chronic wounds, mainly diabetic foot ulcers and venous leg ulcers. The core of the project was the fabrication of a conceptually new wearable negative pressure device equipped with Information and Communication Technologies.

Concerning the project, my group was in charge of developing four sensors to be included in the device: A transepidermal water loss (TEWL) sensor, a pH sensor, a temperature sensor and a pressure sensor.

TEWL sensor: The permeability of the skin to water is an important factor in the maintenance of water and heat balance in the human body. When damaged, skin loses its barrier function and normal rates of TEWL are compromised. Water vapor flows through the skin in an abnormal way losing the thermoregulation effect. Under the wound dressing, the perilesional skin is prone to maceration resulting from the prolonged exposure to exudate or moisture, so this measurement is important to verify both the wound management and the healing process [5].

pH sensor: The pH of normal skin ranges from about 4.8 to 6.0 in relation to the presence of the so-called "acid mantle", while the interstitial fluid shows

neutral values. When affected by infection, pH values in chronic venous leg ulcers and in pressure ulcers shift to alkaline or neutral values if compared with the normal surrounding skin [6]. An accurate measurement of the pH of the wound can indicates the stage of the ulcer, which moves toward acid pH during the healing process [7].

Temperature sensor: Inflammation is the first stage of the wound-healing process. Unlike normal wounds, chronic wounds remain in the state known as early inflammation for a long period, i.e. six weeks or more. The local increase of temperature is one of the signs indicating the starting of the chronic state. Monitoring the temperature is important to detect perfusion variations [8].

Pressure sensor: Patients suffering in venous insufficiency or venous leg ulcers (VLUs) are commonly treated with compression therapy. Compression therapy consists in applying a bandage on the lower limb of the leg in order to improve venous return and to reduce oedema.

Depending on the severity of the wound, different sub-bandage pressures are recommended. The application of excessive pressure can in fact damage the skin and increase ankle stiffness, thus reducing the patient's mobility. Low pressure levels instead threaten the effectiveness of the treatment. Common clinical guidelines do not consider the pressure distribution exerted along the length of the leg. However, in order to achieve an effective treatment, pressure should be uniform over time [9]. To date, pressure monitoring is usually being carried out using sensors that present considerable drawbacks, such as single point instead of distributed sensing, no shape conformability, bulkiness and constraints on patient's movements. In our work, a matrix textile sensor was developed using as responding material a commercial polypyrrole-based polymer. The matrix technology was exploited for its ability to measure the sub-bandage pressure with a suitable temporal and spatial resolution. The flexibility of the sensor allowed a good and comfortable fit of the sensor on the leg. Experimental tests performed on three human volunteers using two different bandage types, revealed the effectiveness of our system in monitoring the sub-bandage pressure over the entire limb of the leg affected by the compression

treatment. The continuous monitoring of the pressure gave dynamic information about the effectiveness of the compression bandage application.

Summarizing, Chapter 1 gives a very brief and general overview about the state of the art of chemical sensors and their applications.

Chapter 2 and Chapter 3 describe the general properties of carbon nanotubes and graphene, respectively.

In Chapter 4 are discussed the chemical results obtained by the covalent functionalization of carbon nanosubstrates. Chapter 5 describes the non-covalent functionalization of SWCNTs.

Chapter 6 summarizes the results obtained by the sensing tests performed delivering on the carbon nanomaterials different concentrations of NH_3 and TMA. Appendix I, as mentioned previously, deals with a side work concerning the development of a pressure sensor to be used for the mapping of the sub-bandage pressure applied during the compression treatment for patients affected by venous insufficiency or VLUs.

CHAPTER 1

Sensor - General definition
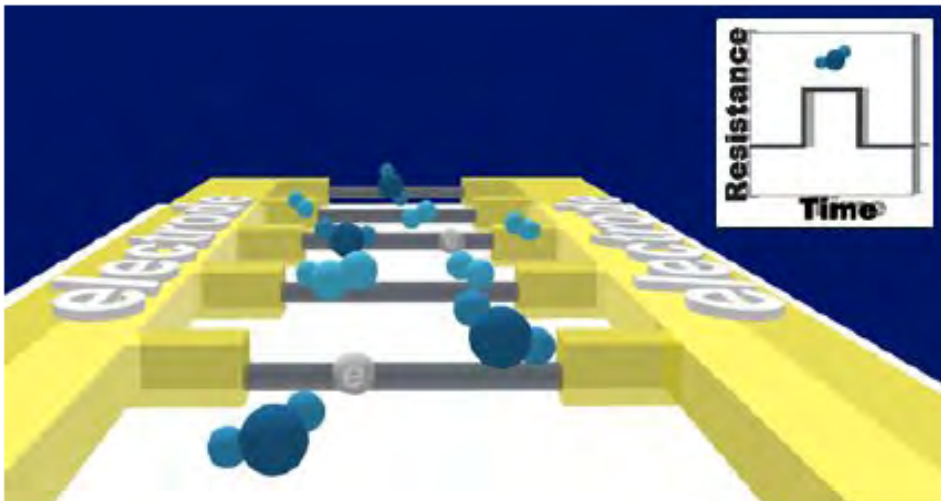
1.1 Sensors

Gas sensors can be developed using different transduction principles based on changes in their electrical or optical properties, mass-sensitivity, etc. IUPAC [10] defines a sensor as "a device that transforms chemical information, ranging from the concentration of a specific sample component to total composition analysis, into an analytically useful signal. The chemical information, mentioned above, may originate from a chemical reaction of the analyte or from a physical property of the system investigated".

According to the operating principle of the transducer, chemical sensors may be classified in: Mass sensitive, Optical, Electrochemical, Electrical.

In this thesis, electrical sensors, and in particular, resistive chemical sensors or chemiresistors, were developed. The chemiresistive approach is based on the changes of the electrical resistance of a chemiresistor, in response to changes in the nearby chemical environment. In a chemiresistive sensor, a direct interaction between the sensing material and the analyte takes place. This interaction leads to a change in the resistance reading. The chemical interaction between the sensing material and the analyte can occur by covalent bonding, donor-acceptor interaction, van der Waals interaction, etc. A basic configuration of a chemiresistive sensor is depicted in Figure 1 and, with some slight variations, it represents the configuration employed in this work.
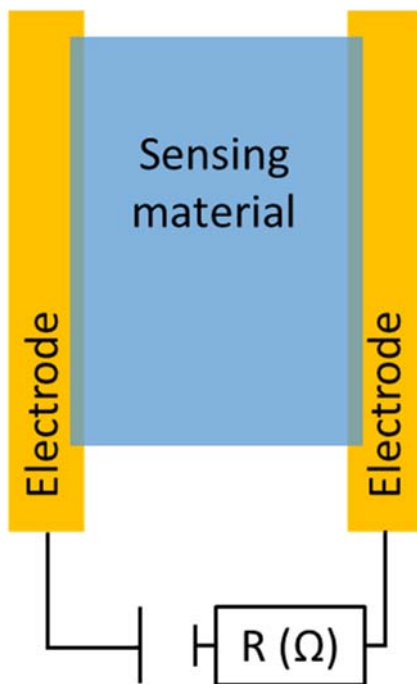
Figure 1: Device concept of a resistive chemical sensor (chemiresistor).

Common sensing materials used for chemiresistors are metal oxides, conductive polymer and recently carbon nanotubes (CNTs) and graphene. In the last few years, carbon nanotubes and graphene have become the most studied carbon nanomaterials for developing gas sensors. The reason of this explosion of interest may be explained considering the high aspect ratio of these materials in comparison with the other nanosized carbon-based molecules. Focusing on the gas sensing of ammonia (NH_3) and trimethylamine (TMA) to date, several chemical sensors have been investigated. Most of them involved the use of metal oxides working at temperatures above 200 °C [11–13]. Recently, researchers have started combining the properties of metal-oxides and carbon nanomaterials[14], for example by decorating the surface of CNTs or graphene with metal-oxides nanoparticles [15]. However, good results were only obtained at high temperatures and/or high concentrations of analyte [16, 17]. Although pristine carbon nanotubes (p-CNTs) change their conductivity upon the interaction with

gas molecules [18–20] the sensitivity and selectivity of these materials toward gas analytes is poor.

Covalent or non-covalent modification of carbon nanomaterials is an effective strategy to obtain compounds with modulated functionalities [21] and increased sensor response. Abdulla et al. [22] showed that the modification of multi-walled carbon nanotubes (MWCNTs) with a conductive polymer enhanced their sensing properties toward NH_3 detection. In that effort, several conductive polymers compositions, e.g. polyaniline, polypyrrole, and poly(3,4-ethylenedioxythiophene)-poly(styrene-sulfonate), were studied for the non-covalent functionalization of CNTs. Among the possible covalent functionalizations, *Pistone et al*. [23] covalently functionalized MWCNTs with benzoic acid groups and then decorated the surface of MWCNTs with different Fe_3O_4 loading. The material were tested for ammonia sensing at 80 and 50 °C in an ammonia concentration range of 250-4000 ppm. In this study, covalent and non-covalent functionalization of carbon nanotubes and graphene was performed, aiming to investigate the sensing performances of the synthesized materials toward the detection of gaseous analytes.

CHAPTER 2

Carbon nanotubes - General properties
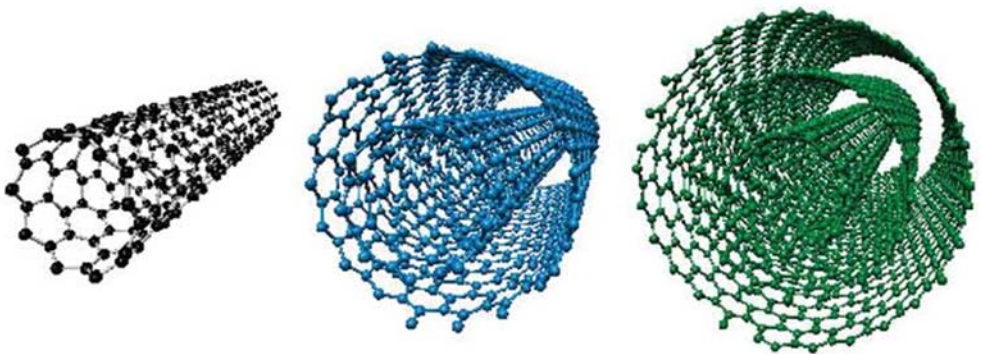
2.1. Carbon nanotubes: Introduction

Carbon nanotubes are a new allotropic form of carbon brought to light by the pioneering work of Iijima in 1991 [24]. Carbon nanotubes (CNTs) exist as single layer (single-walled carbon nanotubes, SWCNTs), double-layer (double-walled carbon nanotubes, DWCNTs) or multi-layer (multi-walled carbon nanotubes, MWCNTs). Structurally, single-walled carbon nanotubes can be described as a single graphene sheet, which is a planar-hexagonal arrangement of sp^2 hybridized carbon atoms distributed in a honeycomb lattice, rolled up into a cylindrical tube with diameter ranging from 0.7 to 2 nm and some micrometers in length. The concentric assembly of two or more single-walled carbon nanotubes generate double-walled carbon nanotubes (DWCNTs) and multi-walled carbon nanotubes (MWCNTs), respectively. DWCNTs and MWCNTs are characterized by larger average diameters than SWCNTs (Figure 2)
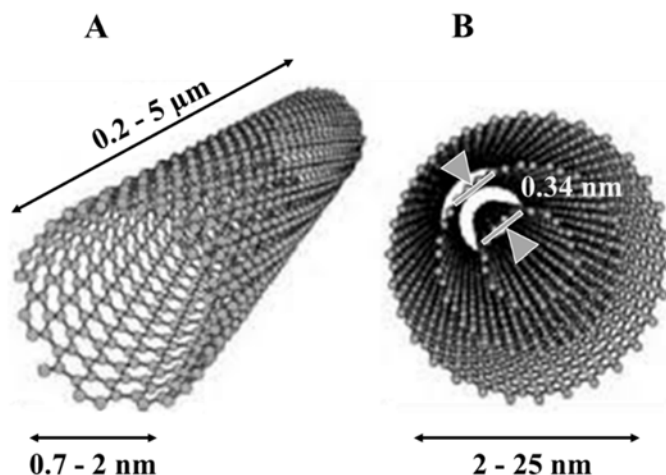
Figure 2. 3D structure of (A) single-walled carbon nanotubes (B) and multi-walled carbon nanotubes.

The structure of CNTs can be described in terms of tube chirality, which is defined by the chiral vector C_h and the chiral angle θ (Figure 3). The chiral vector represents the direction in which the hypothetical graphene plane is rolled-up to

form the nanotube. In other words, CNTs are formed by connection of the head and tail of the chiral vector.

The chiral vector can be decomposed in two components as shown in the equation reported below:

$C_h = n\ a_1 + m\ a_2$

Where a_1 and a_2 are the unit vectors along the zigzag carbon bond of the hexagon lattice of the graphene sheet, and *n* and *m* are the number of hexagons crossed by the vector [25].

SWCNTs are divided in three mainly subgroups depending on the orientation of the tube axis relative to the carbon network. According to the *n* and *m* values of the components of the chiral vector, when *m* is equal to zero (*m*=0) CNTs appears in the zigzag form, when n=m they show armchair arrangement and when n≠m they are chiral.

Figure 3: Schematic representation of rolling graphene sheet to create CNTs in a zigzag, chiral and armchair arrangement.

The different arrangement of the aryl rings lead SWCNTs to have different electrical properties: Armchair SWCNTs show metallic conductivity, whereas zigzag or chiral SWCNTs behave as semiconductors.

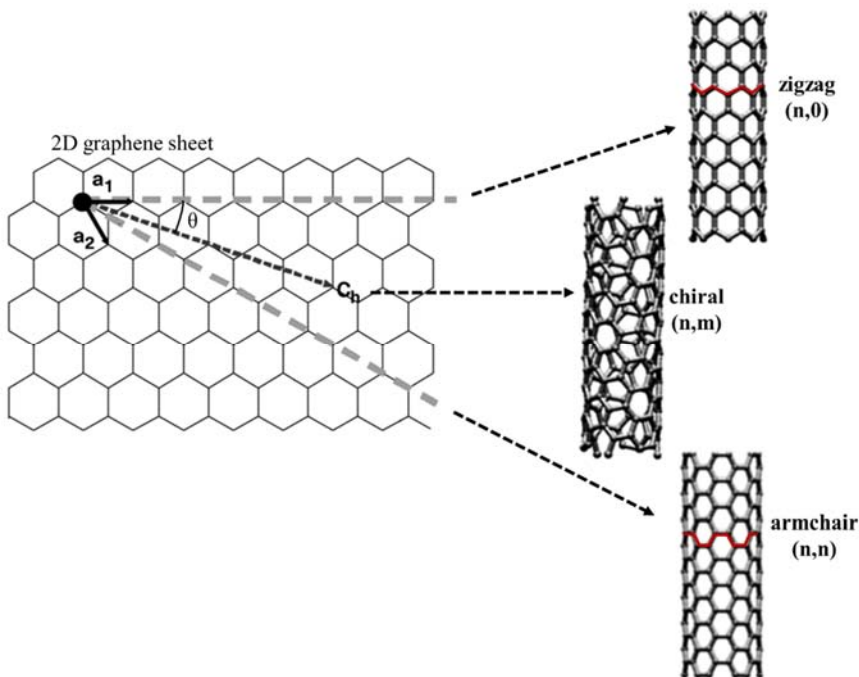For simplicity, CNTs are usually depicted as open-ended tubes, however, in reality, their extremities are capped with fullerene-types hemisphere. The different curvature of the caps with respect to the sidewalls of CNTs causes a different reactivity of these two regions toward chemical functionalization. Moreover CNTs are not ideal structures. They present defects which in turn make addition reactions more favored in these positions [26].

The chemical structure of CNTs skeleton is composed entirely of sp^2 bonds, similar to those of graphite. These bonds, which are stronger than the sp^3 bonds found in alkanes and diamond, provide CNTs with their unique strength.

Moreover carbon nanotubes are characterized by a very high aspect ratio (typically ~300-1000) which make them suitable for a large range of applications as additives, catalyst and sensors. The following sections will be providing an overview about the excellent electrical, mechanical and thermal properties of CNTs [27, 28].

2.1.1. Carbon nanotubes: Electrical properties

We have seen that CNTs, in particular SWCNTs, can have metallic or semiconducting behavior depending on the coefficient values *n* and *m* of the chiral vector C_h. If the solution of the equation $2 \cdot (n + m)$ is an integer number multiple of three, SWCNTs show metallic properties instead of a nonmetallic/semiconductor behavior. Some examples of band gaps in different types of CNTs are reported in Figure 4 [29].
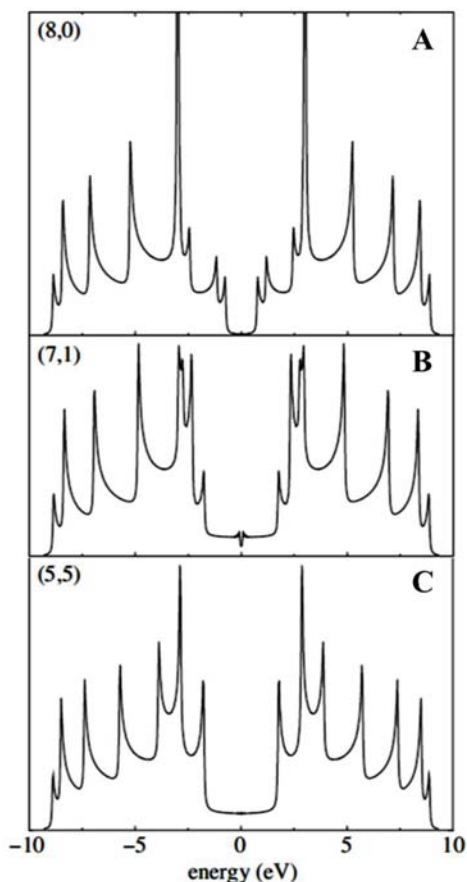
Figure 4: Electronic densities of state for (A) zigzag carbon nanotubes, (B) chiral nanotubes and (C) armchair CNTs.

These considerations are valid for SWCNTs. On the other hand, conductivity in MWCNTs is quite complex. The CNTs' band gap, in fact, decreases with increasing diameter. Moreover, the interwall interactions in MWCNTs can redistribute the current over individual tubes non-uniformly. Even though the interaction between two adjacent cylinders, namely two SWCNTs coaxially rolled up, is small, it cannot be overlooked. As MWCNTs are made up of some coaxial SWCNTs, they cannot be strictly considered as one dimensional conductors. Their electrical behavior is closer to that of graphite as they have a band structure very rich [30].

Moreover, the strong π interaction between CNTs walls, generated by the extended sp^2 hybridization of carbon atoms constituent the skeleton of carbon nanotubes, cause the spontaneously formation of "ropes" of CNTs. The resistivity of SWCNTs ropes was estimated to be in the order of 10^{-4} ohm-cm at 27°C. This means that SWCNTs ropes are the most conductive carbon fibers known.

In this work commercial MWCNTs and SWCNTs were used. They were used in bulk, so their electric performances were considered as the average of all species statistically formed during the production process. Statistically, SWCNTs produced by any method used for large scale synthesis [31, 32] are 1/3 metallic and 2/3 semiconducting. Thus, for SWCNTs, was taken the weighted average response of metallic and semiconducting species. Moreover, semiconducting SWCNTs are mainly p-type tubes. MWCNTs were considered metallic.

The electrical behavior of pristine and functionalized CNTs as function of interaction with gas molecules will be discussed later, in Chapter 6.

2.1.2. Carbon nanotubes: Mechanical properties

CNTs are expected to be high-strength fibers. The honeycomb lattice of the rolled graphene sheet forming CNTs is constituted by covalently bonded carbon atoms. The strong bonds make the elastic modulus of CNTs the largest of any known material. SWCNTs are stiffer than steel and are very resistant to damage from physical forces thanks to their good flexibility due to the ability of bending of sp^2 carbon network by changing hybridization when the surface is curved. However, quantify the Young's modulus, which defines the relationship between stress (force per unit area) and strain (proportional deformation) in a material, is challenging. As CNTs show good ability in bending, a Young's modulus of about 1.8 TPa was determined using the atomic force microscope (AFM) technique [33]. The unanchored ends of a freestanding nanotube can be pushed out of their equilibrium position and the force required to push the nanotube can be thus measured. Other values significantly higher than that reported above have also been measured. These differences probably arise through different experimental

measurement techniques employed. Theoretical studies have shown that the Young's modulus depends on the size and chirality of SWCNTs and they have calculated a Young's modulus of 1.09 TPa for a generic nanotube. However, when working with different MWCNTs, others have noted that the modulus measurements of MWCNTs using AFM techniques do not strongly depend on the diameter. They argue that the modulus of the MWCNTs correlates to the amount of disorder in the nanotube walls. Not surprisingly, when MWCNTs break, the outermost layers break first.

2.1.3. Carbon nanotubes: Thermal properties

Carbon nanotubes show thermal conductivity with anisotropic character as for graphite crystal. In graphite, thermal conductivity dramatically changes along different crystal axis. Bundles of CNTs experience the same phenomenon. The high thermal conductivity of CNTs is comparable to that of diamond crystal and to that of the in-plane graphene sheet [34].

Due to technological difficulties of synthesizing high-quality and well-ordered nanotubes, it is still challenging to perform thermal conduction measurements. Often, it is necessary to observe theoretical predictions of the thermal conductivity of CNTs and the influence of various defects present on them. However, several experimental results can be found in literature. Mizel *et al.* studied the thermal behavior of MWCNTs and ropes of SWCNTs in the range of temperature 1<T<200 K. MWCNTs showed a specific-heat similar to that of graphite, mostly due to the similar structure of the two materials. Conversely, ropes of SWCNTs showed a strong temperature dependence and specific-heat data very large in magnitude.

Thermal conductivity of CVD-grown MWCNTs measured from 4 to 300 K [35] was found

to varied as T^2, similar to that of graphite. Similar behavior was observed in the measurements of the temperature-dependent thermal conductivity of bundles of SWCNTs from 8 to 350 K [36].

2.1.4. Carbon nanotubes: Methods for large scale production

To date, numerous routes for producing carbon nanotubes are continuously being studied and developed. However, the three most important techniques employed so far to produce multi- and single-walled carbon nanotubes at large scale production are electric arc discharge, laser ablation, and chemical vapor deposition. Although these techniques are the most exploited, they present advantages and disadvantages.

Electric Arc Discharge: This method was first used for the production of fullerene. It is a high temperature process which involves the evaporation of graphite electrodes for the CNTs production. Two graphite electrodes are placed at 1 mm of distance in a furnace filled with a gaseous background, usually argon or helium, at low pressure. A high voltage is applied between the two electrodes with the formation of an arc discharge (Figure 5). The local heating of the electrodes causes the instant vaporization of a little amount of graphite which condenses in a spider-web like deposit formed from the product mixture.
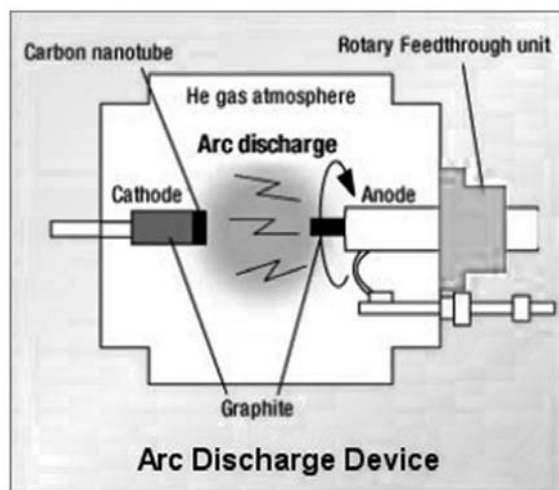

Figure 5: Schematic representation of an arc discharge reactor.

Without catalyst, this method produces a mixture of multi- and single-walled carbon nanotubes. The inclusion of metal catalysts [37] such as Co, Ni, Fe, etc.,

in the anode lead to the production of SWCNTs. The electric arc discharge method is one of the simplest methods used for the synthesis of nanotubes on large scale. However, this method produce a large amount of simultaneous multimorphology soot. This implies several steps of purification.

Laser Ablation: Also the Laser ablation technique was used in the past for the production of fullerene. However, it was noticed that the incorporation of a metal catalyst in the carbon target leaded to the formation of SWCNTs with a narrow diameter distribution and high yields [38]. This technique is therefore exploited for the production of high quality SWCNTs. Unlike electric arc discharge, this method is not suitable for large mass production; moreover the use of high power lasers makes it rather expensive. The reactor in laser ablation technique is similar to that of electric arc discharge, comprising a graphite target placed inside a furnace filled with an inert gas at low pressure. Unlike electric arc discharge, the graphite target (doped with a metal catalyst for SWCNTs production) is heated and vaporized in this case with a pulsed or continuous laser (Figure 6).
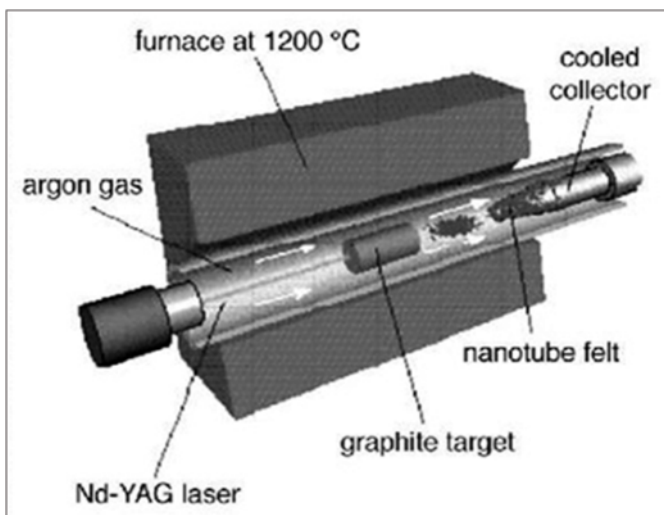

Figure 6: Schematic representation of a laser ablation reactor.

The formed carbon vapor moves out from the hot-point, before to cool down and condense on the surface of the gaseous catalyst. A gas flow transports the product in a porous filter where the carbon nanotubes and other by-products are grouped and then, collected at the end of the process. The SWCNTs yield and diameter distribution can be varied by controlling the process parameters in the reaction [39, 40].

Chemical Vapor Deposition: In this technique volatile precursors are used to provide a carbon feed source to a catalyst particle or pore at elevated temperatures (350-1000 °C) [41]. The gas source is usually composed by small gas molecules containing carbon atoms, such as acetylene, ethylene, methane, ethane or carbon monoxide, flowing in a furnace (Figure 7).
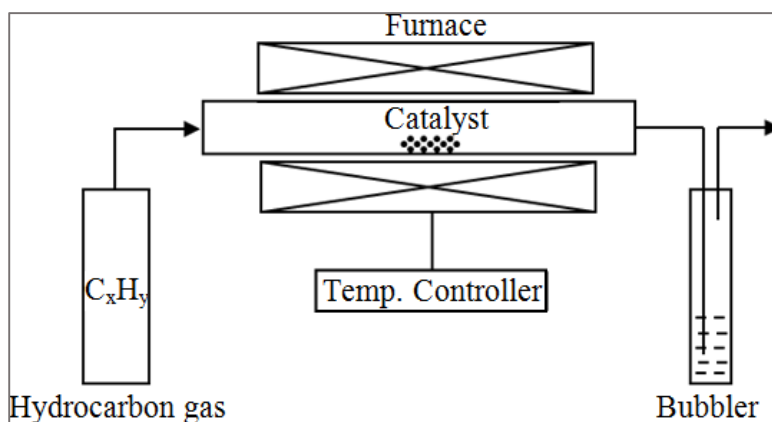
Figure 7: Schematic representation of a CVD setup.

The furnace heats the gas mixing and the reactive carbon atoms are obtained by applying thermal energy. In the furnace is inserted a target substrate, which is coated by sputtering with a transition metal (usually nickel, iron or cobalt) working as catalyst for the grow process. Carbon atoms diffuse to the target substrate and condense. The heating, cause the melting of the metal which forms small "islands" of nm-size, in which carbon nanotubes starts to grow. Formation of single- or multi-walled carbon nanotubes is governed by the size of the catalyst particle. Focusing on SWCNTs growth, modification of the process parameters

33

provides relatively pure SWCNTs with controlled diameter, diameter distribution and yield. CVD is a multivariable process which can be adjusted in several manners. This makes of the CVD the most common route by which CNTs are formed.

2.1.5. Carbon nanotubes: Purification

The three different production techniques described above and in general all the production processes known so far to produce CNTs, yield undesirable byproducts that interfere with the properties of CNTs themselves. Such impurities are constituted by amorphous carbon, metal catalysts, fullerenes, etc. Determining the purity of nanotube materials is challenging because no unified standard parameters have been established yet to assess the quality of CNTs. However, several methods have been developed to purify CNTs mostly from amorphous carbon and metal catalysts. These methods entail various oxidation steps, sonication, thermal treatments, chemical acid treatments, etc. In addition to the purification need, CNTs produced on large scale present different diameters, chirality and they are grouped in bundles composed of up to hundreds of single nanotubes [12]. Thus, the purification process should encompasses in addition to the removal of impurities also the possibility to divide CNTs in length, diameter and permit in the specific case of SWCNTs to distinguish between semiconducting and chiral tubes.

Lots of efforts have been dedicated in the recent years to the development of post-synthesis methods to effectively separate semiconducting nanotubes from the as-synthesized mix. The approaches reported in literature to solve this problem are countless, however the main principles are based on density gradient ultracentrifugation (DGU), use of electric fields, selective polymer wrapping, spontaneous phase separation, and gel-chromatography. These approaches allowed to obtain high purity and single-chirality semiconducting SWCNTs, however they suffer in low yield, elaborate multi-step procedures and/or rely on

expensive equipment that hinders the easy commercial affordability of SWCNTs [42].

The main methods employed for the purification of CNTs from amorphous carbon and metal catalysts involve the use of oxidative and non-oxidative approaches [43]. The oxidative approach exploits the attitude of CNTs to react slower than carbonaceous impurities (i.e. small graphitic particles, fullerenes and amorphous carbon) under oxidative treatment. This method is easy, affordable and permit to purify CNTs without the introduction of many defects on the CNTs surface. However, if performed without control of the oxidative parameters like time of reaction and acid concentration, the oxidative treatment can lead to serious damages of CNTs structure. The oxidative treatment is usually performed using nitric acid (HNO_3) or sulfuric acid (H_2SO_4), eventually combined in various ratios with hydrochloric acid (HCl), at high temperature (100-150 °C).

The non-oxidative method is non-destructive and it is commonly based on centrifugation and filtration of CNTs dispersed in water with the help of surfactants. The centrifugation allows the removal of materials that are not fully dispersed; the filtration retains carbon nanotubes on the filter and permits the recovery. Also more sophisticated purification techniques can be used in order to obtain length and size separation of CNTs. One example is represented by the size exclusion chromatography (SEC). However, this technique presents the disadvantage of treating only small amounts of CNTs dispersions at a time.

2.2. Carbon nanotubes: Functionalization

Carbon nanotubes are very attractive for their outstanding properties, however the main drawback showed by both single- and multi-walled carbon nanotubes is their poor wettability and poor dispersibility/solubility in most organic solvents and water. CNTs lattice is formed by carbon atoms sp^2 hybridized. These carbon atoms are covalently bonded to three near atoms via three sp^2 orbitals while the fourth valence electron occupies the p_z orbital, forming a delocalized π-bond by the partial overlapping of all p_z orbitals. The strong bonds and the formation of ropes

or bundles of CNTs due to the extended π-conjugation are the causes of the low reactivity showed by pristine CNTs (p-CNTs). Functionalization is usually performed to improve the chemical reactivity of CNTs toward the interaction with solvent of different nature (i.e. polar or non-polar) or toward other kind of matrices as for example the interaction with target molecules. The two main approaches for functionalizing CNTs are the covalent and non-covalent method. The first one implies a chemical modification of the CNTs sidewalls; the second one is commonly carried out with molecules capable of interact with the external surface of CNTs via π-stacking. Other technique exist to functionalize CNTs, these are the endohedral functionalization, where the functionalize molecules interact with the inner walls of CNTs and the defect-side functionalization. In this work two approaches of covalent functionalization and one approach of non-covalent functionalization were studied and they will be discussed in detail later in Chapter 4 and Chapter 5. In these section we are going to describe the general approaches to physical and chemical CNTs modification properties by covalent, non-covalent, endohedral and defect-side functionalization.

2.2.1. Carbon nanotubes: Covalent functionalization

Covalent functionalization, or sidewall functionalization, involves the disruption of the sp^2 lattice of CNTs by the formation of sp^3 hybridized carbon atoms on the CNTs sidewalls (Figure 8). So far, several strategies of covalent modification are known. However, to understand better the concept of covalent functionalization it is necessary to take into account the precursor of CNTs, namely graphite and fullerene. Graphite and graphene are chemically inert due to their planar, aromatic framework. Only very reactive compounds, such as fluorine, are able to interact with the planar sp^2-bonded carbon atoms of graphite or graphene. Conversely, CNTs appear to be more reactive toward functionalization. This different behavior can be addressed to two factors responsible of the different chemical reactivity: (a) curvature-induced pyramidalization at the single carbon atoms [44, 45] and (b) p-orbital misalignment between adjacent pairs of carbon atoms [46, 47].
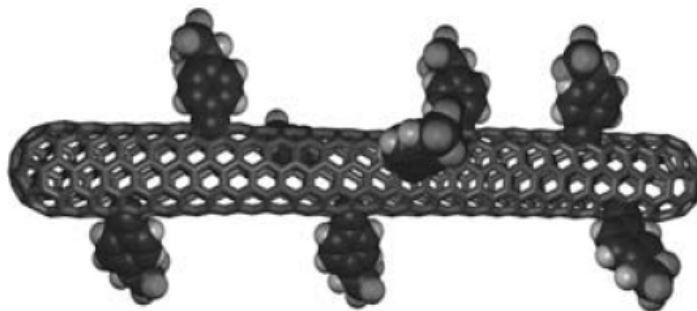
Figure 8: Sidewall functionalization.

This explains why CNTs are less reactive of fullerene (more release of pyramidalization strain energy if compared to CNTs) and why the fullerene-like end caps of CNTs are more susceptible toward addition reactions than their sidewalls. Direct consequence of this, is the correlation of the tube diameter with reactivity toward addition reactions [48] as both the pyramidalization angle and the p-orbital misalignment angle scale inversely with the diameter. Thus, smaller CNTs are expected to be more reactive than their larger counterparts [31, 49, 50]. MWCNTs with an outer tube diameter in the range of 5-50nm generally exhibit a much lower tendency toward sidewall addition reactions than SWCNTs with diameter distributions in the range of 0.7-2nm. Another factor affecting the reactivity of SWCNTs is their metallic/semiconducting character.

Joselevich [51] noted that pyramidalization and misalignment just dealt with the localized electronic structure of carbon nanotubes without including the delocalized electronic band structure in the same molecular orbital picture. By merging the solid-state physics description of band structure with the chemical molecular orbital theory, the different reactivities of metallic and semiconducting SWCNTs can be interpreted and predicted by a classical HOMO-LUMO description[37]. Therefore, semiconducting nanotubes can be described as analogous to aromatic [4n + 2] annulenes, whereas metallic nanotubes are analogous to antiaromatic [4n] annulenes. Regarding sidewall functionalization, one of the

37

most controversial problem is the assessment of the formation of a new covalent bond on the carbon nanotube sidewalls. In general a combination of techniques are being used to evaluate the real modification of the nanotube structure. A general overview of these techniques will be provided at the end of this chapter.

2.2.2. Carbon nanotubes: Non-covalent functionalization

Whereas covalent functionalization involves the disruption of the sp^2 lattice of CNTs causing an alteration of their intrinsic physical properties such as the lowering or the loss of their inherent conductivity, non-covalent approach affords the preservation of this and other characteristics.

The non-covalent interactions with CNTs involve hydrophobic, van der Waals, and electrostatic forces provoking the physical adsorption of suitable molecules [36] (usually polyaromatic molecules presenting a large π-system, such as anthracene or pyrene or heterocyclic polyaromatic molecules such as porphyrins [52] or phthalocyanines) onto the sidewalls of CNTs (Figure 9). Non-covalent functionalization is also achieved by polymer wrapping or physisorption of surfactants or biomolecules such as DNA and peptides.
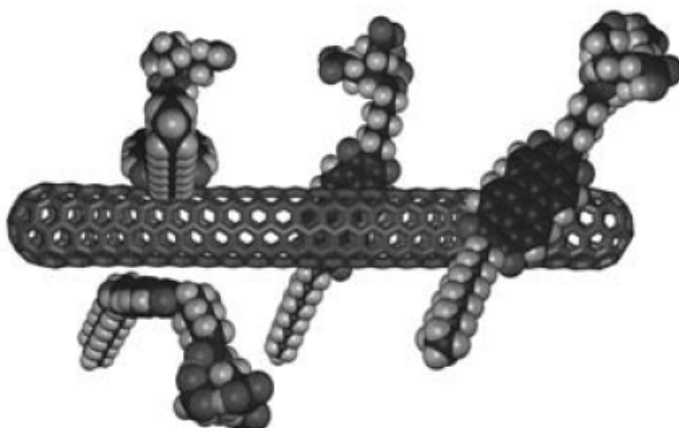

Figure 9: Non-covalent functionalization.

2.2.3. Carbon nanotubes: Endohedral functionalization

The endohedral functionalization is the direct variant of exohedral (non-covalent) decoration of CNTs. In this technique the cavity of CNTs are filled with small size molecules (Figure 10) such as fullerene [53] which was one of the first molecules to be used for this purpose. Other molecules exploited for the endhoedral functionalization are metal nanoparticles or metal halides [54, 55].
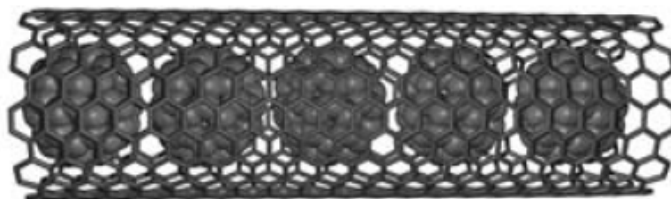

Figure 10: Endohedral functionalization.

The filler can be inserted in the cavities of CNTs during their growth or in a second time via solution phase process exploiting the capillary effect. This kind of functionalization takes place in the inner part of CNTs. This means that the disperdibility/solubility of CNTs is not improved by this type of functionalization.

2.2.4. Carbon nanotubes: Defect-site functionalization

Basically, the defect-site functionalization [12] concerns the chemical transformation of defect sites of CNTs, intrinsically present or intentionally introduced by oxidation (Figure 11). As-grown CNTs present some defects coming from the production process. These defects are mostly located at the extremities of CNTs where the growth process starts or where the catalyst is attached. Other defects can be found in the CNTs structure such as the replacement of the hexagon rings with pentagons or heptagons rings, the so-called pentagon-heptagon defect which cause the bending of the CNTs affecting their electrical and mechanical properties, holes and some functional groups. These defect can also be introduced intentionally onto the CNTs surface. The major method

employed is the oxidation process that, depending on the severity, causes more or less damages on the CNTs structure. Basically, the oxidation process can open the caps of CNTs, introduce hole in the sidewalls, and introduce a high density of various oxygen groups (mainly carboxyl groups) where successive reactions of esterification or amidation are fostered opening in this way the route to other chemical modifications. The oxidative attach is favored where defect-sites are present.

Figure 11: Defect-site functionalization.

CHAPTER 3

Graphene and reduced Graphene Oxide - General properties
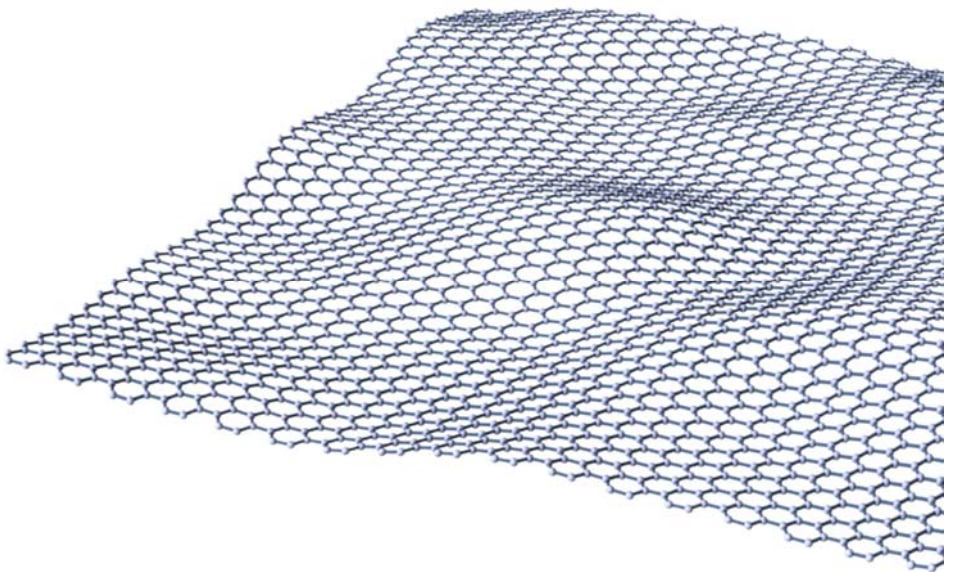
3.1. Graphene and reduced graphene oxide: Introduction

Although CNTs are formed wrapping up a graphene sheet, graphene was isolated only in 2004 by Geim's group. Geim's group successfully extracted monolayer graphene sheets by repeatedly cleaving a graphite crystal with an adhesive tape to its limit [56] (Figure 12). The first reason for the so late isolation of a one graphene sheet was that no one expected graphene to exist in the free state and secondly there were not experimental tools able to search for one-atom-thick flakes [57]. Although the scotch tape method was an outstanding discovery, its application for mass production is not feasible. Strong efforts are continuously made by researchers to develop efficient method for the synthesis of considerable amounts of graphene [58].
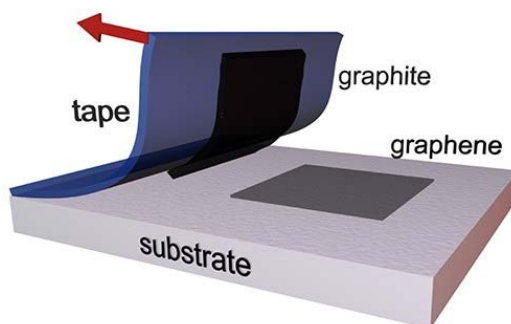
Figure 12: Scotch tape method.

Graphene is a two-dimensional flexible structure made out of sp^2 hybridized carbon atoms arranged in a honeycomb lattice. The sp^2 hybridization between one s orbital and two p orbitals leads to a trigonal planar structure with a formation of a σ bond between carbon atoms that are separated by 1.42 Å. The σ band is responsible for the robustness of the lattice structure in all carbon allotropes. Like CNTs, graphene presents unique properties.

3.1.1. Graphene: Electrical properties

At room temperature, graphene shows a high electron mobility which exceeds 2000 cm^2/V s.

The electron mobility is given by the electronic structure of graphene. While the s orbital and the two in-plane p orbitals contribute to the robustness of the carbon sheet, namely to the mechanical stability, the remaining p orbital, which is perpendicularly oriented to the molecular plane, hybridizes to form the p* (conduction) and p (valence) bands, which dominate the planar conduction phenomena [59]. Graphene mobility is temperature-independent between 10 and 100 K. This suggested that the dominant scattering mechanism was related to graphene defects [60]. Improved sample preparation, including post-fabrication desorption of adsorbates by current annealing, allowed to reach mobilities of more than 25000 cm^2/V s.

Also the reduce graphene oxide (rGO), which is the cheapest alternative for the production of graphene on large scale, shows high electrical performances. This suggests that rGO can be considered a promising competitor to the industrial standard ITO (Indium Tin Oxide) for the production of transparent conductive films. ITO is one of the most widely used transparent conducting oxides showing a typical sheet resistance of 40 Ω/sq for visible transparency above 80%. The casting of dispersions of rGO into sub-3 nm thick films yield >90% transparent coating with sheet resistance of the order of 10^9 Ω/sq which can be reduced to ca. 40 kΩ/sq upon thermal annealing [61]. Other strategies are known to increase the conductivity of industrially produced graphene. These strategies can be exploited for the production of low-cost, high-performance conductive transparent materials.

3.1.2. Graphene: Optical properties

In the visible range, the transparency of thin graphene films decreases linearly with the film thickness. A film 2-nm thick films shows a transmittance higher than

95%. For 10-nm thick films, the transmittance remains above 70% [62]. The macroscopic linear dependence of the transmittance as function of the thickness of the graphene film is intimately related to the two-dimensional gapless electronic structure of graphene [63].

3.1.3. Graphene: Mechanical properties

All carbon allotropes show a very high robustness. Graphene is not an exception. Its stress-strain response was investigated using the AFM technique. The reported stiffness was in the order of 300-400 N/m, with a breaking strength of ca. 42 N/m for a defect-free sheet [64]. The estimated Young's modulus is 0.5-1.0 TPa which is very similar to that of graphite [50].

A very interesting and surprising property is showed by graphene oxide sheets which, despite their defects have a Young's modulus of 0.25 TPa [65]. This characteristic, combined with its low cost, makes of graphene oxide a good candidate to be exploited in matrices mechanical reinforcement.

3.2. Graphene: Production

Since 1960 scientists tried to isolate graphene without success. The discovery in 2004 paved the way to new experimental physic efforts to produce graphene also on large scale. New techniques such as epitaxial growth and CVD were shown to produce high-quality graphene, however these techniques are suitable only for a limited production. In order to produce large quantities of graphene for industry applications more affordable methods, such as the total organic synthesis of polyaromatic hydrocarbons (PAH) and the chemical reduction of graphene oxide were developed. To date, the chemical reduction method seems to be the more viable route to produce graphene sheets in considerable amounts.

Mechanical exfoliation: Mechanical exfoliation is the method used by Geim's group to isolate a graphene sheet for the first time. It consists in peeling off a graphene sheet from graphite flakes by a Scotch tape. The presence of graphene

is then identified by transferring the sheet on a silicon substrate (usually SiO_2/Si) and checked with optical microscopy. The presence of a graphene sheet is eventually proved by performing AFM or Raman spectroscopy. Since the interlayer van der Waals forces in graphite are very weak, graphite can be easily exfoliated by using a Scotch tape. However this method is not suitable for mass-production. It requires manual searching for single graphene sheet between producing very low yields and time consume.

Epitaxial Growth: In the epitaxial growth [66] isolated monolayer of graphene are grown on a substrate, usually a single-crystal of silicon carbide (SiC). The silicon is heated at ca. 1300 °C under vacuum. This causes the sublimation of the silicon atoms, while the carbon atoms remains on the surface. The carbon atoms of the surface reorganize and graphitize in graphene islands over the entire surface of the surface. A careful and controlled sublimation allow to obtain graphene in single-layer, bi-layer or multi-layer. An advantage of this method is the possibility to pattern the graphene growth by using standard lithography techniques. Nevertheless, the epitaxial growth technique is not widespread for large mass production, mainly because of its discontinuity in the process of graphene growth.

Chemical Vapor Deposition (CVD): Chemical vapor deposition (CVD) represents an important method for low-defects graphene industrial production. CVD is able to produce graphene with few structural and electrical damages. The technique consists in a direct growth of graphene on a transition metal substrate (Ni or Cu films) via saturation of carbon upon exposure to a hydrocarbon gas (such as methane) at high temperature. At the cooling of the substrate, the solubility of carbon on the substrate decreases and the carbon precipitates to form mono- to multi-layer graphene sheets on the substrate. Disadvantages of this technique are the difficult control of films thickness and the need of expensive materials to form the substrate. The latter point limits the large-scale production.

3.2.1. Graphene oxide and reduced graphene oxide: Production

A chemical method to produce graphene, or better, reduced graphene oxide (rGO) is based on the weakening of the van der Waals cohesive force upon insertion of reactants in the inter-layer space of graphite, then the layer are distanced and treated to give the final graphene-like material. The all sequence comprises a multi-step process that starts from the oxidation of the graphite leading to the production of graphite oxide, then the graphite oxide is being exfoliated to give graphene oxide (GO) which is finally being reduced to rGO (Figure 13).

A fast route for producing GO was proposed by Hummer [67] in 1958. Since then, Hummer's method is one of the most exploited method to produce GO, and subsequently rGO, at low cost and on large scale. Beyond some slight changes carried out in the years, the basic Hummer processes is based on the dispersion of graphite in a mixture of concentrated sulfuric acid, sodium nitrate and potassium permanganate at 45 °C for 2 hours. X-ray and electron diffraction investigation of GO show the total disappearance of the typical graphite inter-layer diffraction peak (0.34 nm) and the appearance of a new one indicating a larger inter-layer spacing (0.65-0.75 nm) which strongly depends from the solution water content [68].
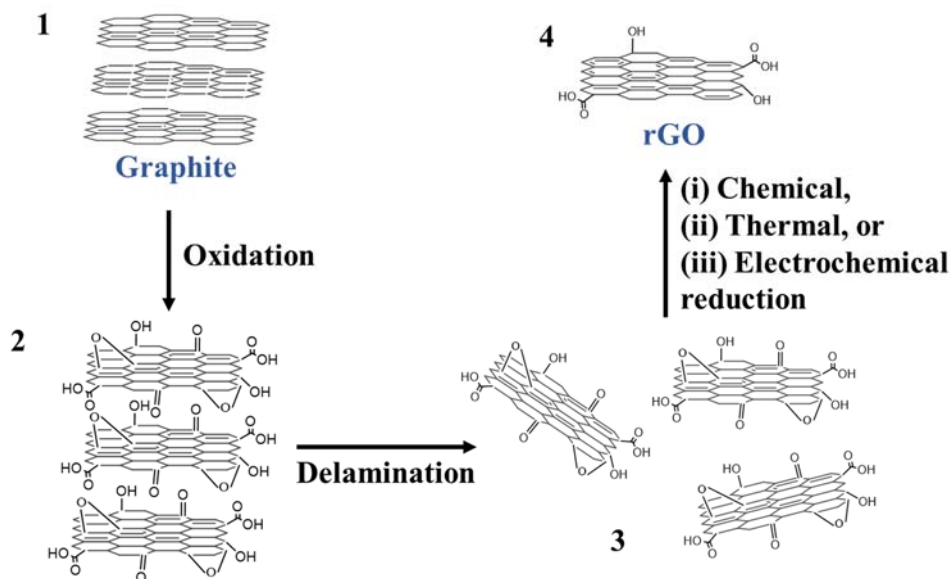
Figure 13: Multi-step process for the synthesis of rGO. The first step is the oxidation of (1) graphite to produce (2) graphite oxide; the second step is the exfoliation of graphite oxide in (3) graphene oxide. The last step is the reduction of graphene oxide by (i) chemical treatment, (ii) thermal treatment, or (iii) electrochemical treatment to (4) reduced graphene oxide.

The oxidation process causes the partial degradation of the sp^2 lattice of graphite into less aromatic carbons. The formation of a sp^2-sp^3 sheet leads to less π-π stacking stability. The oxidation introduces on the graphite sheet many oxygen atoms in the form of hydroxyl and carboxyl moieties. In particular, oxygen atoms in the form of hydroxyl (-OH) and epoxy (C-O-C) groups decorate the top of graphene sheet, instead a lower amount of carbonyl (C=O) and carboxyl (O=C-OH) groups decorate the edges of the sheet. Once graphite oxide is formed, it can be converted into graphene oxide by delamination. Ultra-sonication is the method commonly used to separate the graphite oxide into individual graphene oxide sheets. The oxygenated moieties introduced on the graphite flakes make graphene oxide dispersions stable in polar solvents such as water. GO chemical and electronic properties are completely different from graphene properties. Compared to graphene, GO has completely different chemical and electrical

properties. It is soluble in polar solvent and it is non-conductive. The latter issue can be partly solved by chemical reduction. The reduction step allows the recovery of most of the electrical properties of pristine graphene obtained by mechanical exfoliation or epitaxial growth. The reduced graphene oxide is an intermediate between graphene and graphene oxide. In fact, by reduction, rGO is not capable to recover completely the sp^2 character typical of a graphene sheet produced with other techniques. However, rGO presents some advantages as the possibility to produce large amount of a reasonable conductive and transparent material as well as the possibility to develop new materials by further chemical derivatization thanks to its more reactivity due to the presence of some oxygenated functionalities that do not disappear even after the reduction process.

3.2.2. Reduction of graphene oxide to produce reduced graphene oxide

GO can be reduced to rGO by several methods. Herein the electrical, thermal and chemical treatments are reported.

Electrochemical treatment: A promising method for the reduction of GO is the electrochemical treatment. In the electrochemical treatment a thin film of GO is deposited on a substrate as glass, plastic, etc., while an inert electrodes is placed opposite to the film in a electrochemical cell in an aqueous buffer solution. The reduction occurs during the charging of the cell. The process is relatively simple and do not produce byproducts. The reduction is mainly caused by the electron exchange between GO and electrodes. Moreover, Zhou et al. found that the potential needed to realize the reduction is controlled by the pH value of the buffer solution. A low pH value is favorable to the reduction of GO, so the authors proposed that H^+ ions participate in the reaction.

Thermal treatment: In this strategy it should be paid attention to temperature. The heating rate and the heating temperature can significantly affects the effect of the reduction on GO. Schniepp et al. found that if the temperature was less than 500

°C, the C/O ratio was no more than 7, if the temperature reached 750 °C, the C/O ratio instead could be higher than 13. Usually it is recommended use temperature close to 1000 °C. The annealing atmosphere is important to guarantee an effective reduction. As the etching of oxygen gas dramatically increases at high temperature, oxygen gas should be excluded during the annealing. Thus, annealing is often performed in vacuum or in inert or reducing atmosphere. The drawbacks of annealing are the large energy and time consuming. In fact, if assembled GO structure are treated, it is required a slow heating to prevent the explosion of the structure due to the expansion of CO and CO_2 gases.

Chemical treatment: Reduction via chemical reactions is a cheap and easy way for the mass production of rGO. Hydrazine was one of the first reactants used for reduction of graphite oxide. Its first use for the reduction of GO was reported by Stankovich in 2007 [69]. The reduction with hydrazine or its derivatives such as hydrazine hydrate and dimethylhydrazine is performed by adding the liquid reagent into a GO aqueous dispersion heating at a moderate temperature. When dried an electrically conductive black powder with C/O ratio around 10 can be obtained.

Also metal hydrides, which are largely known for their reducing properties were tried. However, a drawback of these reagents is their strong reactivity with water, which is the main solvent exploited for exfoliation and dispersion of GO. A recent new reagent reported in literature, which seems a good candidate for substituting hydrazine is the ascorbic acid (Vitamin C). Ascorbic acid, in addition to produce C/O ratio comparable to that of hydrazine, is non-toxic and has a higher chemical stability with water than metal hydrides such as $NaBH_4$.

3.3. Graphene and reduced graphene oxide: Functionalization

Despite to great application potential, graphene itself possess zero band gap and it is rather chemical inert. This led researchers to search for effective methods to functionalize graphene with the aim to alter its chemical properties. Several

strategy have been developed in the recent years. Herein, we briefly describe only the covalent and non-covalent approaches. As for CNTs, these methods aim to produce more soluble and more reactive carbon nanomaterials. Common examples of non-covalent functionalization include polymer wrapping, $\pi-\pi$ interactions, electron donor−acceptor complexes, hydrogen bonding, and van der Waals forces. In all instances, non-covalent functionalization leads to enhanced dispersibility, biocompatibility, reactivity, binding capacity, or sensing properties. Non-covalent interactions are expected to have lower energies than those of covalent bond. This is true, expect when a very large surface is considered such as for graphene or reduced graphene oxide. In this case the non-covalent interaction energies can rival with those of covalent bonds.

Reduced graphene oxide presents defect as epoxides or hydroxides bound to the carbon atoms. Besides π-interactions, as occurs in graphene, rGO can thus experiences hydrogen bonds due to the oxygenated moieties.

The covalent functionalization can follows two general route: (a) the formation of covalent bonds between free radicals or dienophiles and C=C bonds of pristine graphene and (b) the formation of covalent bonds between organic functional groups and the residual oxygen groups of rGO. The most attractive organic species for the reaction with sp^2 carbons of graphene are organic free radicals and dienophiles. The covalent attachment of organic groups to graphene sheets can be exploited to introduce a band gap, which, in controlled conditions, makes the functionalized graphene potentially useful as semiconducting nanomaterial.

CHAPTER 4

Carbon nanotubes, graphene and reduced graphene oxide: Covalent approach for the synthesis of sensitive materials
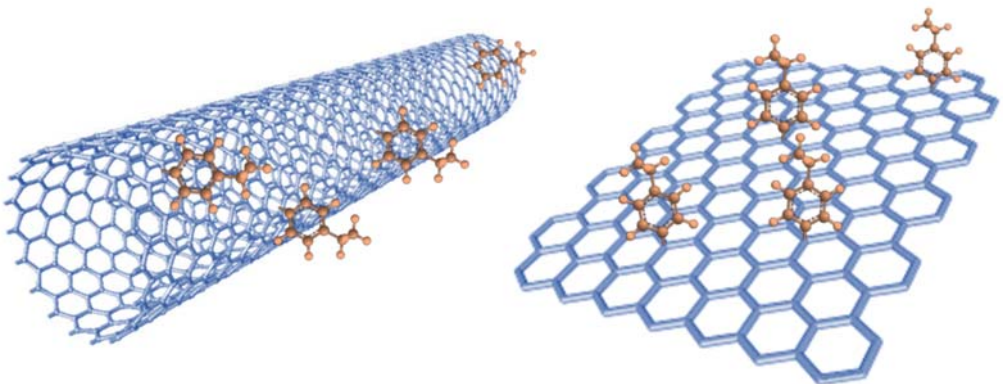
4.1. Introduction

Covalent functionalization allows the insertion of different functional groups on the surface of carbon nanomaterials. So far, many methods have been investigated for CNTs and graphene functionalization. In this work, we aimed to compare the potentialities of SWCNTs, MWCNTs and rGO toward two different approaches of covalent functionalization: nitrene addition and diazonium addition. Phenyl and alkyl azide react with the C-C bonds of CNTs, graphene or rGO with the formation of nitrene as reactive intermediate. The reaction leads to the formation of a three-membered aziridine ring [70, 71] (Figure 14). The generation of the reactive intermediate nitrene can be performed either thermally or photochemically.

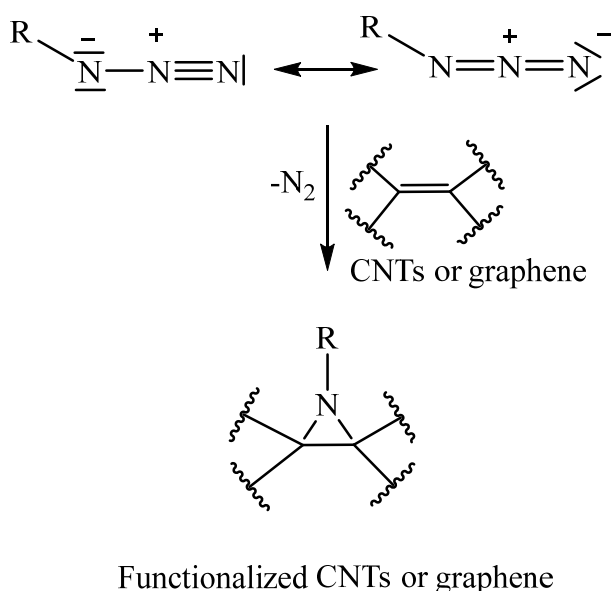Functionalized CNTs or graphene

Figure 14: Covalent functionalization of CNTs or graphene by [2+1] cycloaddition of nitrene.

Diazonium can be generated in situ by treating an aniline with isoamyl nitrite. The reductive dissociation of diazonium salt leads to the loss of N_2 and to the formation of an aryl radical. The aryl radical reacts with the surface of carbon allotropes

enabling the grafting of molecules or chains by the formation of a C-C bond (Figure 15).

CNTs or graphene

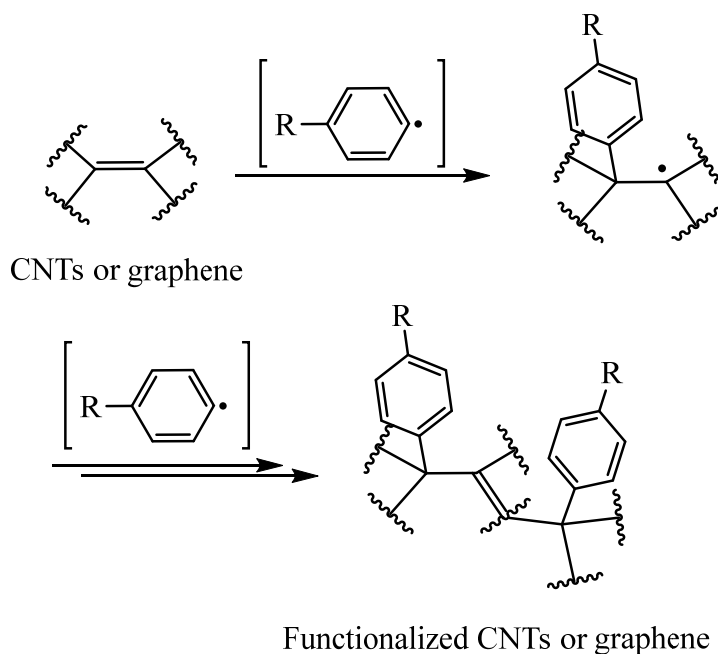Functionalized CNTs or graphene

Figure 15: First step in the mechanism of functionalization of CNTs or graphene by the addition of a diazonium salt.

Both reactions require an excess of functionalizing reagent. However, it has been shown that a large excess of diazonium salt precursor often leads to the formation of biaryl coupling on the top of the first monolayer attached [72]. For this reason, we decided to work with a limited excess of functionalizing molecule, namely 1:10 w/w, to avoid undesired side reactions.

In this chapter, results obtained with the covalent functionalization of different types of CNTs and graphene are discussed. Section 4.2 focuses on the covalent functionalization of SWCNTs, MWCNTs and rGO using as intermediate of reaction two different reactive species: nitrene and diazonium. The different reactivity of the different substrates toward the two different mechanisms of reaction was investigated. Section 4.3 is dedicated to the investigation of the

reactivity of MWCNTs, SWCNTs, Graphene and rGO toward the nitrene addition using as functionalizing molecules a fluorinated and a non-fluorinated compound.

4.2. Nitrene and diazonium chemistry: synthesis and characterization of the functionalized carbon nanomaterials

The synthesis and characterization of SWCNT-N-$C_6F_4CO_2H$, SWCNT-N-$C_6F_4CO_2CH_3$, SWCNT-$C_6F_4CO_2H$, MWCNT-N-$C_6F_4CO_2H$, MWCNT-N-$C_6F_4CO_2CH_3$, rGO-N-$C_6F_4CO_2H$, and rGO-$C_6F_4CO_2H$ is described in this paragraph.

4.2.1. Instruments

^{1}H and ^{19}F NMR spectra were recorded on a Bruker AVANCE III HD 400 instrument at 400 MHz and 376 MHz, respectively. Chemical shifts are reported as δ values (ppm) and referred to the residual protons of deuterated chloroform.

High resolution mass spectra were measured with a Bruker Daltonics APEXIV 4.7 Tesla FT– ICR–MS using ESI ionization.

Thermogravimetric analyses (TGA) under nitrogen were performed with a TA Discovery TGA by heating samples at 10 °C/min from 50 to 1000 °C.

Raman spectra were measured by a Horiba Jobin-Yvon LabRam (HR 800) Raman Confocal Microscope, with a laser excitation at 532 nm and a laser spot size of 1.2 μm.

UV-Vis-NIR absorption spectra of dispersions of CNTs in 1,2-dichlorobenzene (o-DCB) were measured in quartz cuvettes using an Agilent Cary 5000 UV-Vis-NIR spectrophotometer.

X-ray Photoelectron Spectroscopy (XPS) was performed on a Physical Electronics Versaprobe II X-ray Photoelectron Spectrometer with a hemispherical energy analyzer and a monochromated X-ray source (Aluminum Kα, 1486.6 eV). Survey scans were collected with a 200 μm - 50 W - 15 kV X-ray setting and a pass energy of 187.85 eV at a base pressure of 10^{-9} Torr.

Scanning electron microscopy (SEM) was carried out using a JEOL JSM-6700F field emission SEM (FESEM). Typical accelerating voltages were 3.0 kV.

4.2.2. Materials

SWCNTs were obtained from Nano-C Corp. (ultra-purified SWCNT, UPT200) and MWCNTs were purchased from Sigma-Aldrich (>98% carbon, outer diameter = 6–9 nm, average length = 5 μm, number of walls = 3–6); both were used without further purification. Solid GO was prepared in our laboratory according to an established procedure [73].

Methyl pentafluorobenzoate (99% purity), hydrazine hydrate (50-60%), isopentyl nitrite (96% purity) and 4-amino-2,3,5,6-tetrafluorobenzoic acid (99% purity) as well as solvents were purchased from Sigma-Aldrich and used as received.

4.2.2.1. Synthesis of methyl 4-azido-2,3,5,6-tetrafluorobenzoate (**1**)

The functionalizing molecules methyl 4-azido-2,3,5,6-tetrafluorobenzoate (**1**) and 4-azido-2,3,5,6-tetrafluorobenzoic acid (**2**) were synthesized according to the methods described by Keana *et al.* [74]. Amounts of methyl pentafluorobenzoate (10 g, i.e. 44.2 mmol) and NaN$_3$ (3.0 g, i.e. 46.1 mmol) were dissolved in a mixture of acetone and water (3:1 v/v) and refluxed for 8 h at 85 °C. Caution: sodium azide can explode when heated as a solid and is highly toxic, so this procedure has to be performed in a fume hood provided with a blast shield.

The mixture was then cooled to room temperature, diluted with 250 mL of water and extracted with diethyl ether (3x300 mL). The extract phases were collected and dried with MgSO$_4$, evaporated and dried under vacuum overnight to give **1** as a white solid (yield: 80.0%). ^{1}H NMR: δ 3.99 (s, 3 H). ^{13}C NMR: δ 53.24 (–OCH$_3$). ^{19}F NMR: δ –138.6 (m, 2 F), –150.9 (m, 2 F). HRMS m/z: [M+H$^+$] calcd for C$_8$H$_3$F$_4$N$_3$O$_2$: 250.0234, found: 250.0237.

4.2.2.2. Synthesis of 4-azido-2,3,5,6-tetrafluorobenzoic acid (2)

4-Azido-2,3,5,6-tetrafluorobenzoic acid (**2**) was prepared treating 4.00 g of **1** with 20% aqueous NaOH (5.3 mL) in MeOH (66.7 mL) and water (7.0 mL). The mixture was stirred at room temperaturefor 24 h. The solution was acidified by 2N HCl in an ice bath to pH<1 and extracted by CHCl$_3$ (3x100mL). The extract was dried (MgSO$_4$) and evaporated to yield 3.416 g (yield 90.6%) of colorless solid (**2**). ^{19}F NMR: δ –137.1 (m, 2 F), –150.7 (m, 2 F). HRMS m/z: [M–H$^-$] calcd for C$_7$H$_2$F$_4$N$_3$O$_2$: 233.9932, found: 233.9919.

4.2.2.3. Preparation of functionalized SWCNTs, MWCNTs and rGO via nitrene addition

An aliquot (20 mg) of SWCNTs was placed in a 100 mL Schlenk flask together with 20 mL of N-methyl-2-pyrrolidone (NMP), then the mixture was sonicated for 2 h. Afterwards, the Schlenk flask was connected to a condenser and the suspension was bubbled with argon for 30 min. An amount of 200 mg of **1** was added to the mixture, which was then heated to 160 °C and left under argon atmosphere and constant stirring for 18 h. The mixture was then cooled at room temperature and the product was isolated by precipitation in acetone. The solid was recovered by centrifugation at 14000 rpm for 20 min, re-dispersed in CHCl$_3$ with the aid of ultrasonication and then recovered again by centrifugation at 13000 rpm for 10 minutes. This procedure was repeated four times. The final black solid (SWCNT-N-C$_6$F$_4$CO$_2$CH$_3$) was dried under vacuum at 70 °C overnight.

The same protocol was used to prepare MWCNTs functionalized with **1** (MWCNT-N-C$_6$F$_4$CO$_2$CH$_3$) and SWCNTs and MWCNTs functionalized with **2** (SWCNT-N-C$_6$F$_4$CO$_2$H and MWCNT-N-C$_6$F$_4$CO$_2$H, respectively).

Functionalized rGO was preparared by dispersing 60 mg of GO in 60 mL of distilled water with the aid of stirring and ultrasonication. After the addition of 300 µL of 50% hydrazine hydrate the mixture was heated to 100 °C for 4 hours, then solid rGO was recovered by centrifugation, dried under vacuum and an

aliquot of 20 mg was functionalized with **2** to obtain rGO-N-C$_6$F$_4$CO$_2$H. The functionalization was accomplished with the procedure described for SWCNTs and MWCNTs.

4.2.2.4. Preparation of functionalized SWCNTs and rGO via diazonium addition

Aliquots of 20 mg of SWCNTs and 20 mg of rGO were sonicated for 30 minutes in 20 mL of o-DCB and NMP, respectively. The resulting suspensions were bubbled with argon for 30 minutes, then 200 mg of 4-amino-2,3,5,6-tetrafluorobenzoic acid (**3**) were added to dispersions and left to dissolve for some seconds. After the subsequent addition of 100 µL of isopentyl nitrite, the mixtures were stirred overnight at 80 °C. The black solid materials were recovered by centrifugation as described in the previous paragraph.

4.2.3. Results and discussion

4.2.3.1. SWCNTs, MWCNTs and rGO functionalized via nitrene addition

Azido group served as precursor for the highly reactive nitrene intermediate. Herein, the aryl nitrene was formed by thermal treatment at 160 °C of methyl 4-azido-2,3,5,6-tetrafluorobenzoate (**1**) and 4-azido-2,3,5,6-tetrafluorobenzoic acid (**2**) in N-methyl-2-pyrrolidone (NMP). This treatment allowed carboxylic acid and methyl ester moieties to be inserted on both SWCNTs and MWCNTs sidewalls (Figure 16a). 4-azido-2,3,5,6-tetrafluorobenzoic acid was instead grafted onto rGO sheets (Figure 16b). Pentafluorophenyl compounds were used since their presence was supposed to foster the interaction of the sensitive material with the target analytes.
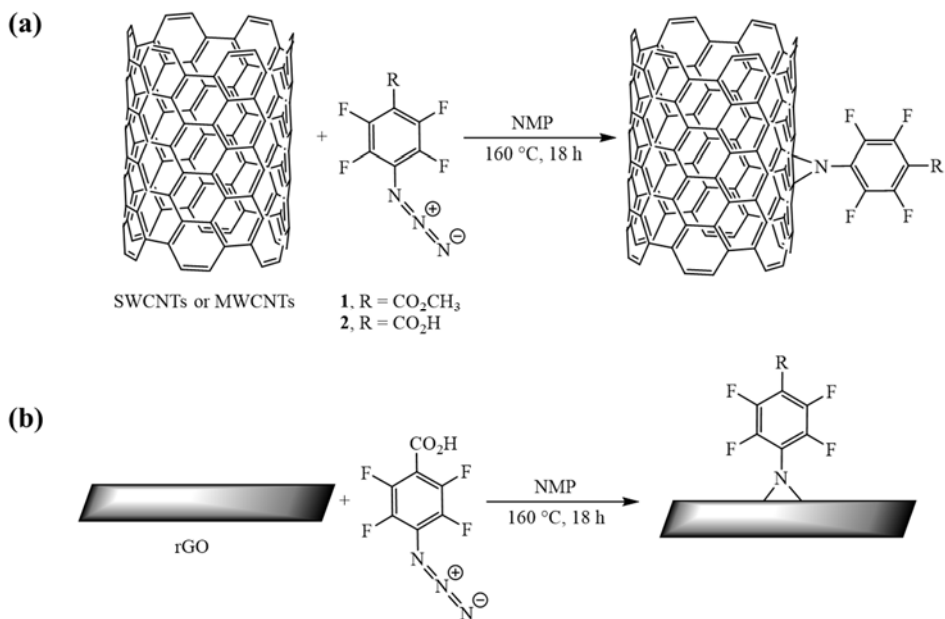
Figure 16: (a) Schematic reaction of SWCNTs and MWCNTs with methyl 4-Azido-2,3,5,6-tetrafluorobenzoate (**1**) and 4-Azido-2,3,5,6-tetrafluorobenzoic acid (**2**) via nitrene addition and (b) schematic reaction of graphene or rGO with **2**.

Table 1 lists the sensitive materials synthetized exploiting the reactivity of nitrene intermediate.

Table 1

Chemical structure and name of the functionalized molecules synthetized by nitrene chemistry.
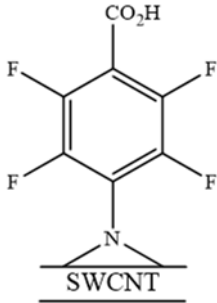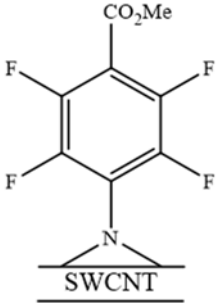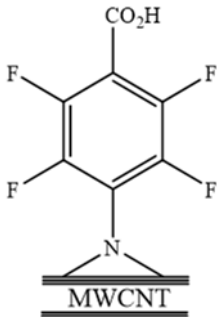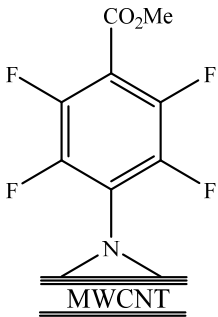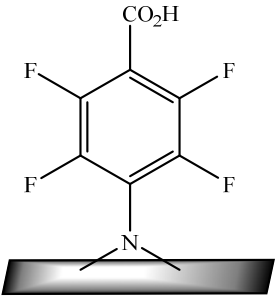
Sensitive compound		
Name	SWCNT-N-C$_6$F$_4$CO$_2$H	SWCNT-N-C$_6$F$_4$CO$_2$CH$_3$
Sensitive compound		
Name	MWCNT-N-C$_6$F$_4$CO$_2$H	MWCNT-N-C$_6$F$_4$CO$_2$CH$_3$
Sensitive compound		
Name	rGO-N-C$_6$F$_4$CO$_2$H	

Figure 17 shows illustrative XPS spectra of pristine and functionalized SWCNTs. The XPS is a surface analysis technique which, among other characteristics, allows to determine the elemental composition of a sample. In this thesis, this technique was exploited to evaluate the degree of functionalization (DF), namely the number of functionalized molecules inserted every 100 atoms of carbon on the surface of the modified CNMs.

DF was calculated basing the results on the quantification of fluorine. As fluorine is not naturally present on the surface of unfunctionalized carbon nanomaterials, a presence of this element in a XPS spectrum means that a functionalization occurred. The percentage of fluorine in comparison with other elements give an idea about the amount of functionalizing molecules attached to the carbon nanomaterials. This amount is therefore expressed in the text as DF which for XPS analysis was calculated making a calibration curve between the number of functionalizing molecules and the theoretical percentage ratio of F:C, where F is the number of fluorine atoms present in the functionalizing molecule and C is 100 carbon atoms plus the carbon atoms present in the functionalizing molecule. The final DF was extrapolated from the calibration curve using the %F:C ratio obtained by the experimental XPS data.

DF was also estimated considering the results of the thermogravimetric analyses. In this case, DF was calculated making a calibration curve between the number of functionalizing molecules and the theoretical percentage weight difference loss of the functionalizing molecules with respect to the weight of 100 carbon atoms. The final DF was extrapolated from the calibration curve using the experimental percentage weight loss obtained by the TGA spectra normalized to the weight loss values of p-CNTs and rGO at 600 °C. The comparison of the DF estimated from XPS and TGA, observable in Table 2, will be commented later in the text.

Table 2

Percentage abundance of C, O, N and F in pristine and functionalized CNMs determined from XPS analysis, and degree of functionalization (DF) relevant to f-CNMs samples calculated from XPS and TGA results. DF is the number of functionalizing groups per every 100 carbons.

Sample	Atom C1s Abundance (%)	O1s Abundance (%)	N1s Abundance (%)	F1s Abundance (%)	DF (XPS) (%)	DF (TGA) (%)
p-SWCNTs	96.90	3.10	–	–	–	–
SWCNT-N-$C_6F_4CO_2CH_3$	84.95	8.35	5.45	0.75	<1	<1
SWCNT-N-$C_6F_4CO_2H$	83.60	8.00	6.35	1.80	1.2	1.2
p-MWCNTs	98.05	1.95	–	–	–	–
MWCNT-N-$C_6F_4CO_2CH_3$	88.70	6.60	4.35	0.40	<1	<1
MWCNT-N-$C_6F_4CO_2H$	87.50	5.55	3.75	2.65	1.3	1.3
rGO	87.30	8.85	2.25	–	–	–
rGO-N-$C_6F_4CO_2H$	79.90	11.25	7.05	1.85	<1	<1

About XPS analysis, as expected, the starting p-SWCNTs, p-MWCNTs and rGO did not show any fluorine signal, whereas the percentages in CNM-N-$C_6F_4CO_2H$ and CNM-N-$C_6F_4CO_2CH_3$ suggested an effective functionalization.
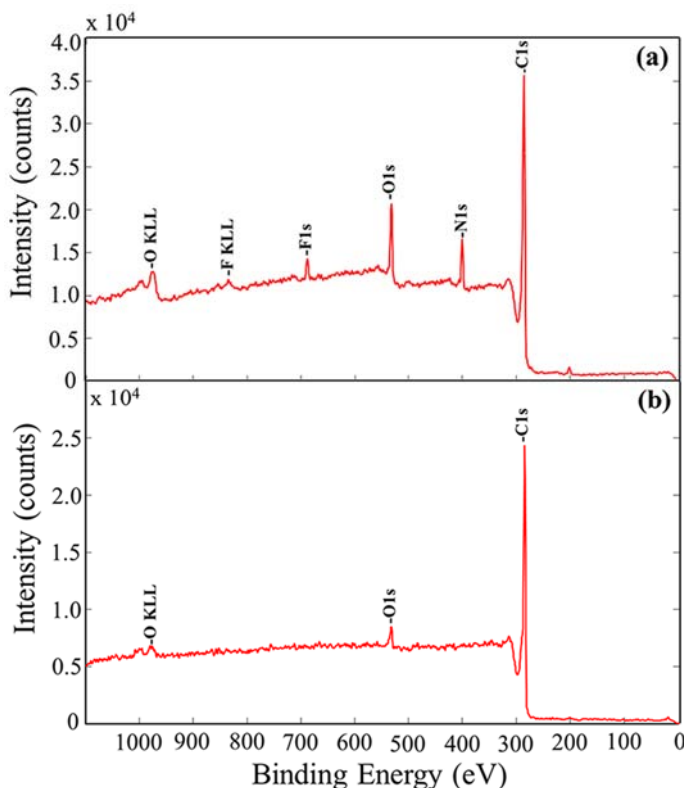
Figure 17: Illustrative XPS spectra for a) SWCNT-N-$C_6F_4CO_2H$ and b) p-SWCNTs. The primary XPS regions of carbon (C1s), oxygen (O1s), nitrogen (N1s) and fluorine (F1s) are visible.

Functionalization was also confirmed observing the TGA profiles of p-CNMs and f-CNMs (Figure 18). Herein, both SWCNT-N-$C_6F_4CO_2H$ and MWCNT-N-$C_6F_4CO_2H$ lost about 16 wt.% of their initial weight at about 450 °C and 525 °C, respectively. This phenomenon was associated with a functionalization degree slightly higher than 1.2 grafted units per 100 carbon atoms. Conversely, SWCNT-N-$C_6F_4CO_2CH_3$ and MWCNT-N-$C_6F_4CO_2CH_3$ showed a smaller weight loss at ~ 450 °C, suggesting a lower functionalization degree (<1%). rGO-N-$C_6F_4CO_2H$ lost about 8% wt.% at around 520 °C yielding a DF<1%. Furthermore, a small weight loss was observed in most samples between 100 and 200 °C, which was probably the result of the desorption of aromatic molecules physisorbed to the CNMs surface [75].
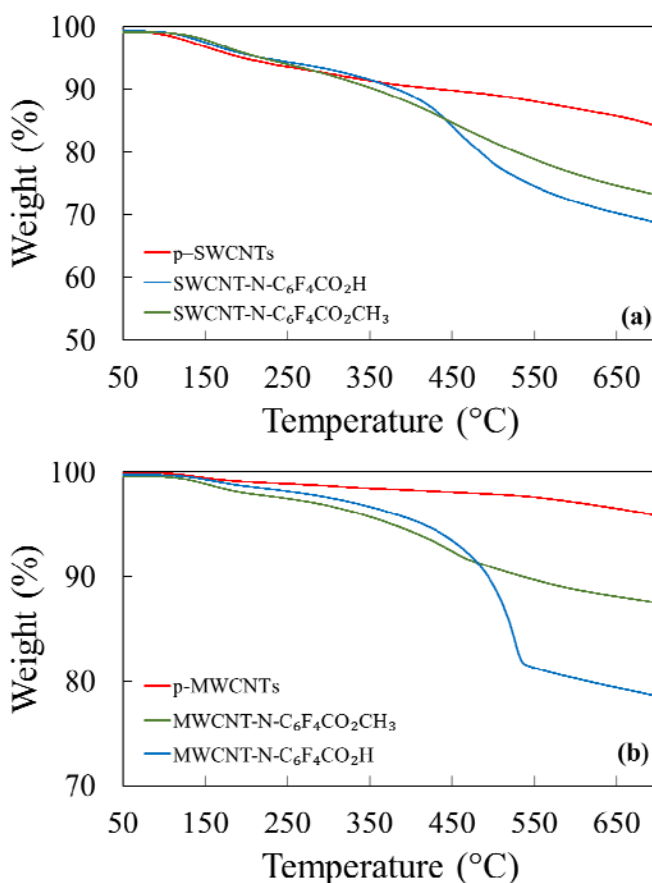
Figure 18: Illustrative TGA profiles of a) p-SWCNTs and f-SWCNTs and b) p-MWCNTs and f-MWCNTs, recorded under nitrogen atmosphere.

Table 2 reveals that the DF of f-CNMs estimated from XPS and TGA data are in good agreement. The reactions of CNTs with **2** gave a level of functionalization of approximately 1.2-1.3 functional groups every 100 nanotube carbon atoms. Conversely, DFs < 1% were obtained by the functionalization of CNTs with **1**. Interestingly, the nitrene chemistry gave similar results for both SWCNTs and MWCNTs, and this suggests that the intrinsic reactivity, i.e. the one controlled by the pyramidalization angle and diameters [76], was not a critical factor. Critical was instead the functionalization of rGO. DFs obtained from XPS and TGA

results, showed for rGO-N-$C_6F_4CO_2H$ a DF<1%. Another experiment not described here, but carried out in our laboratory, was the functionalization of GO with -N-$C_6F_4CO_2H$. The reaction was performed in the same conditions of the rGO/4-azido-2,3,5,6-tetrafluorobenzoic acid system and gave a DF of 1.4% and 1.3% by XPS and TGA analysis, respectively. This result, in evident disagreement with the DF<1% obtained for the sample rGO-N-$C_6F_4CO_2H$, suggested how the presence of defects on the CNM surface enhanced the reactivity of the substrate. However, the sample GO-N-$C_6F_4CO_2H$, was not considered in this work because the final material was not conductive and so not suitable for the development of a resistive sensor.

UV-Vis-NIR spectroscopy is largely exploited in literature to investigate the properties of SWCNTs. In this thesis, it was applied to confirm the covalent nature of the bonds originated via nitrene chemistry on the SWCNTs surface.

Figure 19 shows the absorption spectra of f-SWCNTs and p-SWCNTs dispersed in o-DCB. The absorption bands in the visible and near-IR regions of p-SWCNTs are attributed to the van Hove singularities, that clearly drop after the functionalization. These different spectra are indicative of significant electronic perturbations of the nanotube structure as a consequence of the disruption of the extended π-conjugation. As expected, these features are no longer visible for SWCNT-N-$C_6F_4CO_2H$ and partly retained for SWCNT-N-$C_6F_4CO_2CH_3$ according to their functionalization degree (i.e., 1.2% and <1%, respectively).
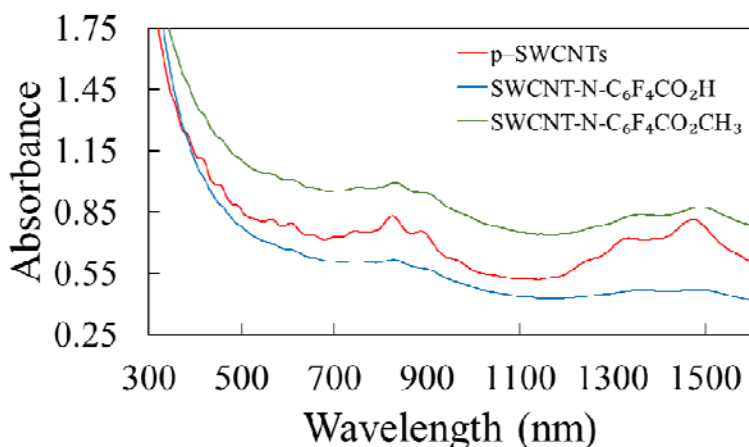
Figure 19: Absorption spectra of p-SWCNTs and f-SWCNTs in o-DCB showing the loss of structure on functionalization.

Raman spectroscopy did not give significant information about the nature of the functionalization. The peaks at about1590 cm^{-1} and 1330 cm^{-1} for SWCNTs (Figure 20a) and at 1580 cm^{-1} and 1346 cm^{-1} for MWCNTs (Figure 20b) are the D- and G-bands, respectively. The G-band is associated with the ordered sp^2 hybridized carbon structure typical of graphite and specifically, it refers to in-plane vibrations from E2g modes. The D-band instead, is due to the amorphous carbon and local defects that originate from structural imperfections [77] and it originates from the out-of-plane vibrations from A1g modes [78]. The intensity ratio of the D- and G-bands (I_D/I_G) is largely described in literature to prove the efficiency of functionalization [79–81]. Usually, an increased I_D/I_G ratio suggests an increased degree of disorder on the carbon nanotube surface, and this information can be used to claim that a covalent modification took place. However, frequently happens that any increase or even a decrease in the I_D/I_G intensity ratio of functionalized material respect to pristine material occurs [82–84] and this was what we observed in our experiments (Table 3). This effect can be explained considering the combination of several factors like for example the use of mild conditions of reaction and low degrees of functionalization which allow to preserve the characteristic structural properties of the raw material

avoiding the damage the outer structure of carbon nanotubes. Moreover, the intensity ratio of the D- and G-bands (I_D/I_G) in our work did not remarkably change after the functionalization, probably because of the opposite effects of the removal of impurities and the creation of defects because of the functionalization [77].
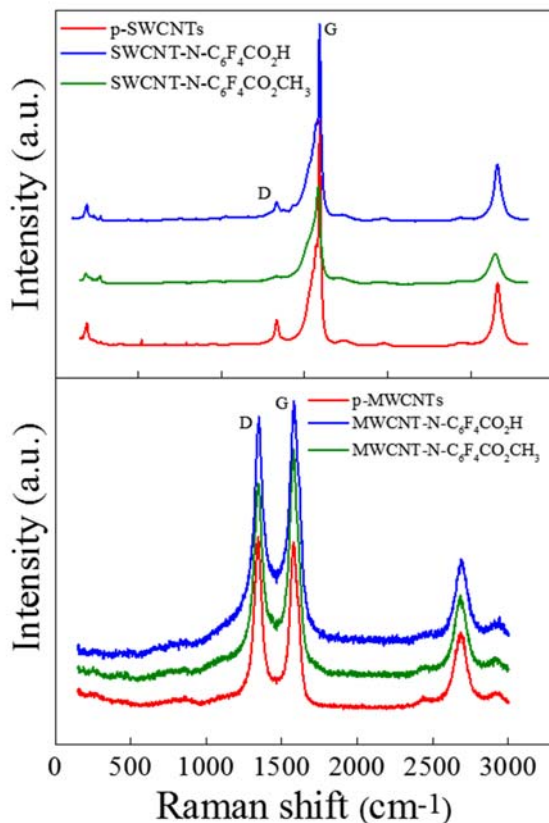

Figure 20: Raman (532-nm excitation) of (a) SWCNTs and (b) MWCNTs.

rGO-N-$C_6F_4CO_2H$ showed the same behavior of SWCNTs and MWCNTs and therefore the same conclusions can be drawn.

Table 3

Intensity ratio of the D and G bands (I_D/I_G) in SWCNTs, MWCNTs and rGO samples.

Sample	I_D/I_G	Sample	I_D/I_G
p-SWCNTs	0.12	p-MWCNTs	1.03
SWCNT-N-$C_6F_4CO_2CH_3$	0.10	MWCNT-N-$C_6F_4CO_2CH_3$	0.89
SWCNT-N-$C_6F_4CO_2H$	0.12	MWCNT-N-$C_6F_4CO_2H$	0.95
rGO	1.27		
rGO-N-$C_6F_4CO_2H$	1.02		

Representative SEM images (Figure 21) reveal the high density of well exfoliated f-SWCNTs, which do not seem to be damaged, shortened or broken by the functionalization procedure.
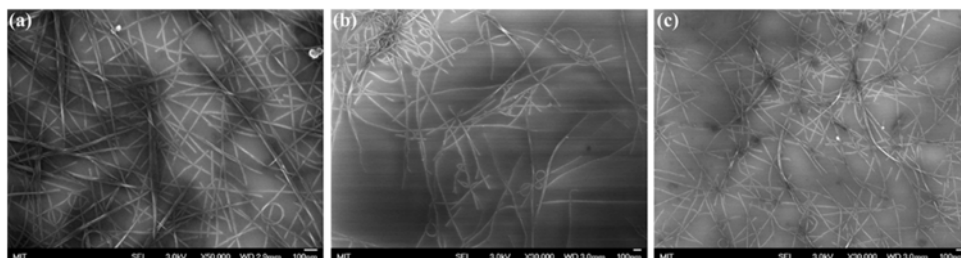

Figure 21: Representative SEM images of (a) p-SWCNTs, (b) SWCNT-N-$C_6F_4CO_2CH_3$ and (c) SWCNT-N-$C_6F_4CO_2H$ samples.

4.2.3.2. SWCNTs and rGO functionalized via diazonium addition

SWCNTs and rGO samples functionalized with 4-amino-2,3,5,6-tetrafluorobenzoic acid *via* diazonium addition are listed in Table 4. A schematic representation of the reaction is given in Figure 22.

(a)

SWCNTs or MWCNTs

3, X = F
4, X = H

80 °C, overnight

(b)

graphene or rGO

3, X = F
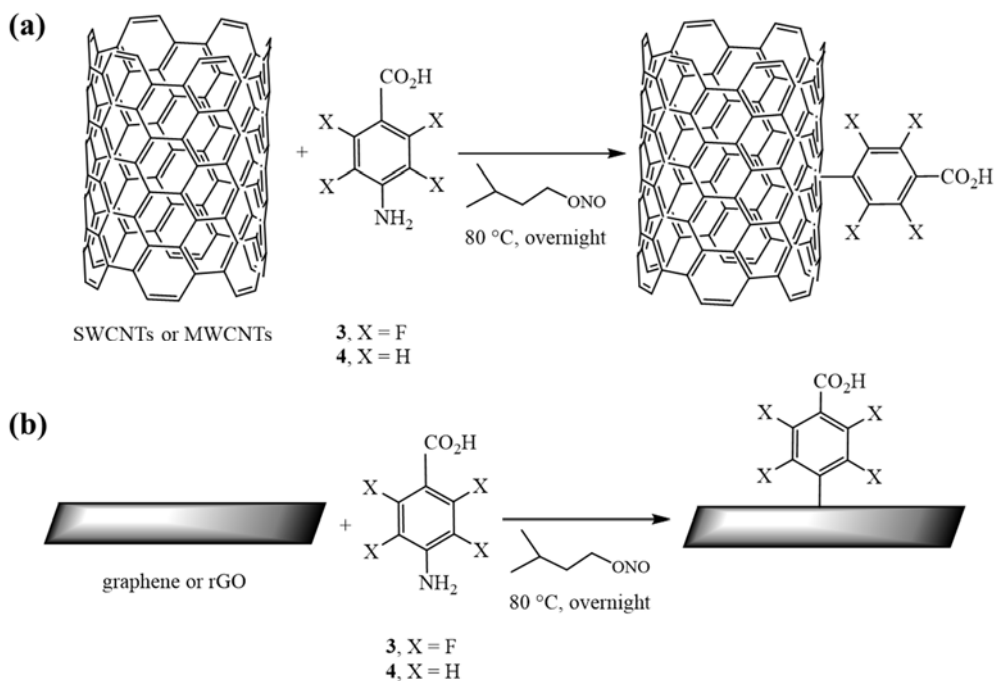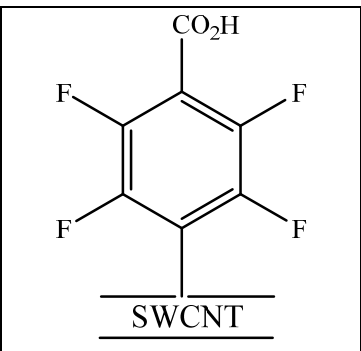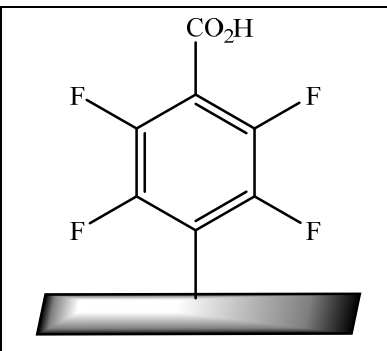**4**, X = H

80 °C, overnight

Figure 22: (a) Schematic reaction of SWCNTs and MWCNTs with 4-amino-2,3,5,6-tetrafluorobenzoic acid (**3**) or 4-aminobenzoic acid (**4**) via diazonium addition. (b) Schematic reaction of graphene or rGO with **3** or **4**.

Table 4

Chemical structure and name of the selector groups synthetized by diazonium addition.

Sensitive compound		
Name	SWCNT-$C_6F_4CO_2H$	rGO-$C_6F_4CO_2H$

The TGA profiles of pristine and functionalized SWCNTs and rGO are shown in Figure 23. The main weight loss, occurred at about 200 °C for both SWCNT-$C_6F_4CO_2H$ and rGO-$C_6F_4CO_2H$, is probably associated to the detachment of functionalizing molecules physisorbed on the surface of the aromatic substrates.
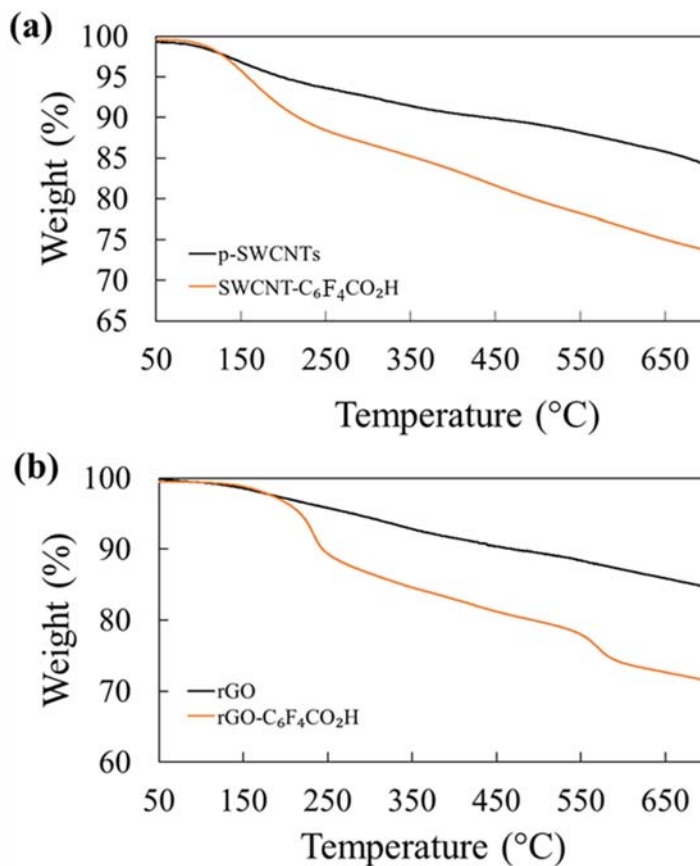

Figure 23: TGA profiles of (a) p-SWCNTs and SWCNT-$C_6F_4CO_2H$ and (b) rGO and rGO-$C_6F_4CO_2H$ collected under nitrogen atmosphere.

Unlike SWCNT-$C_6F_4CO_2H$, rGO-$C_6F_4CO_2H$'s TGA plot showed also a slight inflection at around 550 °C, suggesting that a small fraction of the functionalizing molecule was attached the rGO sheets covalently.

The XPS analysis confirmed the presence of fluorinated molecules in the samples SWCNT-$C_6F_4CO_2H$ and rGO-$C_6F_4CO_2H$ with a DF of 1 and 1.2 for SWCNT-

72

$C_6F_4CO_2H$ and $rGO-C_6F_4CO_2H$, respectively. The DF calculated by TGA was of 1 for both the samples. The TGA results were fairly consistent with the results obtained by XPS spectroscopy.

UV-Vis-NIR carried out for the sample $SWCNT-C_6F_4CO_2H$ confirmed the non-covalent attachment of the molecule **3** on the CNTs sidewall. $SWCNT-C_6F_4CO_2H$ spectrum, in fact, showed several characteristic bands of p-SWCNTs.

As predictable, Raman spectroscopy did not give useful information about the kind of functionalization. The I_D/I_G of $SWCNT-C_6F_4CO_2H$ and $rGO-C_6F_4CO_2H$ were 0.11 and 1.28, respectively, indicating that no alteration on the CNMs structure occurred.

4.3. Diazonium addition: fluorinated and non-fluorinated anilines

Diazonium chemistry is very easy to apply for the covalent functionalization of CNMs. Herein, we decided to further investigate the potentialities of this kind of functionalization using as carbon nanosubstrates: SWCNTs, MWCNTs, graphene (G) and rGO and as functionalizing molecules: 4-amino-2,3,5,6-tetrafluorobenzoic acid and 4-aminobenzoic acid. We were curious to verify how the presence of fluorine on the aromatic ring could influence the reactivity of the diazonium intermediate. Moreover, the presence or the absence of fluorine on the functionalized molecules affected the sensing response of the chemoresponsive materials toward the detection of volatile amine as shown in Chapter 6.

4.3.1. Instruments

Thermogravimetric analyses (TGA) under nitrogen were performed with a Mettler Toledo TGA/SDTA 851 analyzer by heating samples at 10 °C/min from 60 to 900 °C.

Raman spectra were carried out using a Renishaw Raman Invia instrument with a laser excitation at 532 nm. The instrument was equipped with a 1800 grooves/mm diffraction grating, a CCD detector, and a 50X magnifying lens.

UV-Vis-NIR absorption spectra of dispersions of CNTs in o-DCB were measured in quartz cuvettes using an Agilent Cary 5000 UV-Vis-NIR spectrophotometer. X-ray Photoelectron Spectroscopy (XPS) was performed using a PHI Versa Probe II.

4.3.2. Materials

SWCNTs were purchased from Nano-C Corp. (nano-c Purified PT25). MWCNTs were purchased from Strem Chemicals (>90% nanotubes, diameter ~140 nm, average length ~7 μm);

Graphene (G) was purchased from ACS material (Industrial-Quality Graphene, thickness ≤ 3.0 nm, BET surface area ~600 m^2/g). Graphene Oxide was obtained from Graphenea (4 mg/mL water dispersion, carbon content 49-56%, oxygen content 41-50%). SWCNTs, MWCNTs, graphene and GO were used without further purification.

4-amino-2,3,5,6-tetrafluorobenzoic acid (99% purity), 4-aminobenzoic acid (99% purity), hydrazine hydrate (50-60%) and isopentyl nitrite (96% purity) were purchased from Sigma-Aldrich and used as received. All other reagents and solvents were purchased from Sigma-Aldrich and used without any purification.

4.3.2.1. Preparation of functionalized SWCNTs, MWCNTs, G and rGO via diazonium addition
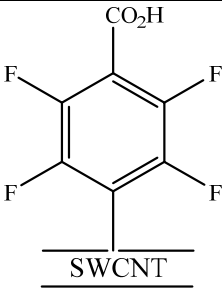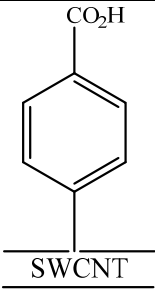
Aliquots of 30 mg of SWCNTs, MWCNTs and graphene (G) were sonicated for 30 minutes in 20 mL each of NMP, then the resulting suspensions were bubbled with nitrogen for 30 minutes. Afterward, 300 mg of 4-amino-2,3,5,6-tetrafluorobenzoic acid (**3**) or 4-aminobenzoic acid (**4**) were added to dispersions and left to dissolve for a few seconds before adding 400 μL of isopentyl nitrite; the resulting mixtures were stirred at 70 °C, overnight. After cooling, the black solid materials were filtered on Teflon filters (0.2 μm) and the filter cakes were

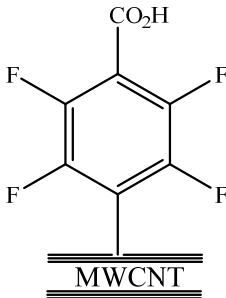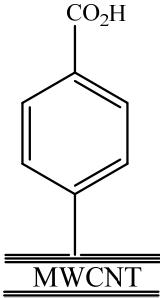washed with water, acetone and chloroform. The remaining cleaned solids were dried at 70 °C under vacuum.

Unlike the reaction described in section 4.2.3.1, where rGO was functionalized with **3** in NMP, herein rGO was functionalized using water as solvent of reaction. rGO was therefore left to react with **3** or **4** in one-pot synthesis starting from a GO water dispersion. A volume of 7.5 mL of GO dispersion in water (dispersion concentration 4 mg/mL) was diluted with 2.5 mL of distilled water, then added with 200 µL of 50% hydrazine hydrate and finally heated to 100 °C for 4 hours to obtain rGO. Then, after the addition of 400 µL of isopentyl nitrite and 300 mg of either **3** or **4** in the same reaction pot, the mixture was heated to 70 °C under stirring for one night. After cooling, the black solid materials 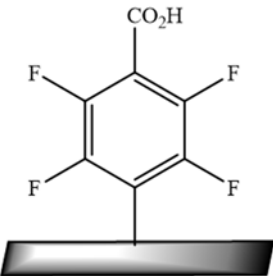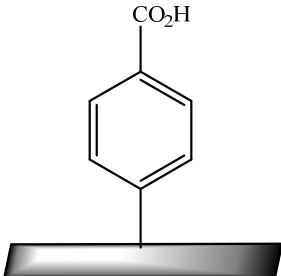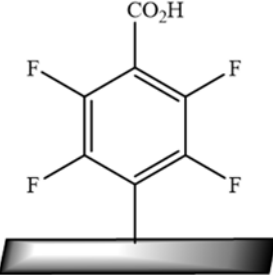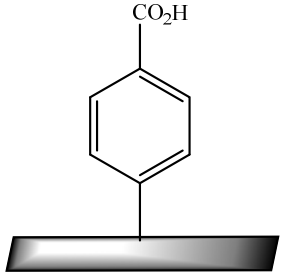were filtered on Teflon filters (0.2 µm) and the filter cakes were washed with water, acetone and chloroform. The remaining cleaned solids were dried at 70 °C under vacuum Table 5 lists the sensitive materials synthetized by the reactions mentioned above.

Table 5

Chemical structure and name of the selector groups synthetized by diazonium chemistry.

Sensitive compound		
Name	SWCNT-$C_6F_4CO_2H$	SWCNT-$C_6H_4CO_2H$

Sensitive compound		
Name	MWCNT-C$_6$F$_4$CO$_2$H	MWCNT-C$_6$H$_4$CO$_2$H
Sensitive compound		
Name	rGO-C$_6$F$_4$CO$_2$H	rGO-C$_6$H$_4$CO$_2$H
Sensitive compound		
Name	G-C$_6$F$_4$CO$_2$H	G-C$_6$H$_4$CO$_2$H

4.3.3. Results and discussion

Pristine and functionalized samples were characterized by TGA, Raman, XPS and UV-Vis-NIR. Two examples of TGA profiles are shown in Figure 24. Table 6, instead, summarizes the weight loss percentage of all synthetized samples. From Table 6 it is possible to note that a large wt.% loss occurred for the SWCNT-

$C_6H_4CO_2H$ sample in comparison with the SWCNT-$C_6F_4CO_2H$ sample (i.e. 9.70% and 1.43%, respectively). The same trend was showed also for MWCNTs, rGO and G: All -$C_6H_4CO_2H$ functionalized samples showed larger wt.% loss than the respective materials functionalized with the pendant -$C_6F_4CO_2H$. Moreover, it is worth mentioning that all wt.% profiles showed the largest weight loss in the range 400-500 °C. This suggested that a covalent functionalization occurred.
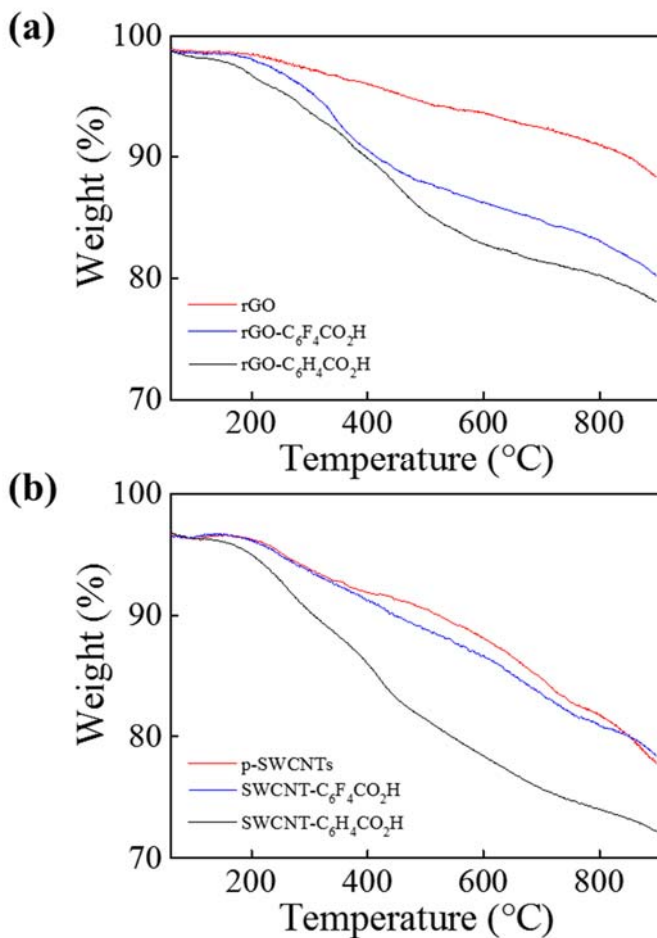

Figure 24: Examples of TGA profiles (experiments carried out under nitrogen) for (a) rGO and f-rGO and (b) p- and f-SWCNTs. Other samples showed similar trends.

Table 6

Percentage weight loss relative to synthetized samples. Δwt.% were calculated at 600 °C and referred to the pristine materials.

	Δwt.% (600°C)
p-SWCNTs	–
SWCNT-$C_6F_4CO_2H$	1.43
SWCNT-$C_6H_4CO_2H$	9.70
p-MWCNTs	–
MWCNT-$C_6F_4CO_2H$	1.05
MWCNT-$C_6H_4CO_2H$	1.71
rGO	–
rGO-$C_6F_4CO_2H$	7.43
rGO-$C_6H_4CO_2H$	10.84
G	–
G-$C_6F_4CO_2H$	5.30
G-$C_6H_4CO_2H$	7.57

Raman spectroscopy considerably contributed to assess the covalent nature of the bond SWCNT/-$C_6H_4CO_2H$. Looking at Table 7, it is evident the increase in the I_D/I_G ratio for the sample SWCNT-$C_6H_4CO_2H$ toward p-SWCNTs. This means that a change in the SWCNT structure occurred causing damages on the extended sp^2 network of SWCNTs surface.

Table 7

Intensity ratio of the D and G bands (I_D/I_G) in SWCNTs, MWCNTs and rGO samples.

Sample	I_D/I_G	Sample	I_D/I_G
p-SWCNTs	0.19	rGO	1.19
SWCNT-$C_6F_4CO_2H$	0.20	rGO-$C_6F_4CO_2H$	1.13
SWCNT-$C_6H_4CO_2H$	0.65	rGO-$C_6H_4CO_2H$	1.16
p-MWCNTs	0.11	G	0.88
MWCNT-$C_6F_4CO_2H$	0.10	G-$C_6F_4CO_2H$	0.90
MWCNT-$C_6H_4CO_2H$	0.11	G-$C_6H_4CO_2H$	0.89

The intensity variation of the D band is well visible in the spectrum of Figure 25: Examples of Raman spectra of (a) p- and f-SWCNTs and (b) rGO and f-rGO. Despite expectations, other Raman spectra did not give significant information regarding the kind of functionalization. The I_D/I_G ratios remained almost constants, indicating that any relevant electronic modification of the CNMs structure took place.
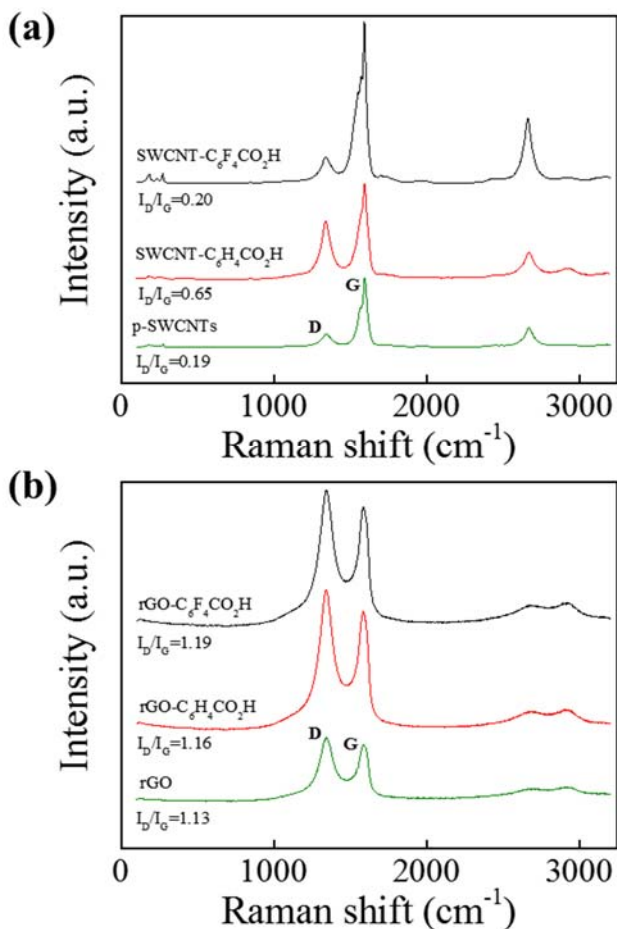
Figure 25: Examples of Raman spectra of (a) p- and f-SWCNTs and (b) rGO and f-rGO.

XPS analysis confirmed the introduction of the $-C_6F_4CO_2H$ and $-C_6H_4CO_2H$ pendants on the surface of SWCNTs, MWCNTs, rGO and G. Figure 26 reports an example of XPS signals relative to the regions of carbon and oxygen for the samples p-SWCNTs, SWCNT-$C_6F_4CO_2H$ and SWCNT-$C_6H_4CO_2H$.
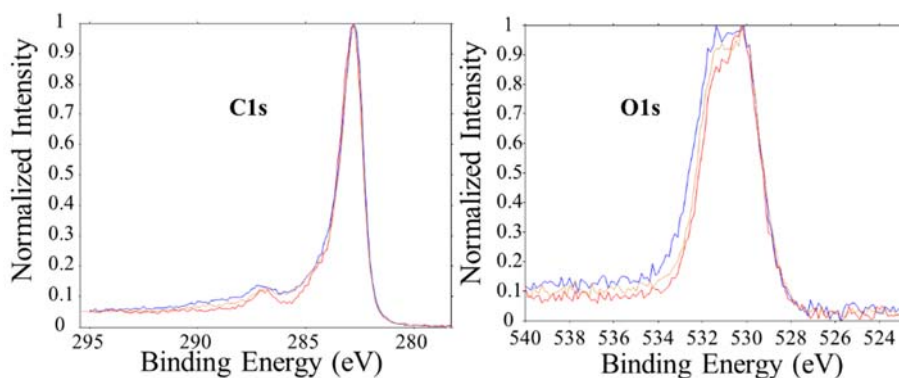
Figure 26: Example of XPS signals. The red line is referred to p-SWCNTs, the yellow line to SWCNT-$C_6F_4CO_2H$ and the blue line to SWCNT-$C_6H_4CO_2H$.

Analyzing the sample SWCNT-$C_6H_4CO_2H$, we observed a raise of the oxidized/oxygenated components, namely an increment of the signal blue respect to the signal red observable in Figure 26. SWCNT-$C_6F_4CO_2H$ spectrum showed the presence, or rather the insertion, of the heteroatom F.

Table 8 reports the percentage abundances of C, O, N and F for SWCNTs, MWCNTs, rGO and G and the comparison of the DFs obtained by TGA and XPS analysis. The DF by XPS analysis was calculated only for the samples functionalized with the fluorinated molecules and it was calculated on the basis of fluorine percentage. DFs for the material functionalized with **4** could have been calculated in relation to the oxygen percentage, however, being oxygen presents also in the pristine material, its quantification could have led to a misleading datum, so we preferred to omit the value.

Table 8

Percentage abundance of C, O, N and F in pristine and functionalized CNMs determined from XPS analysis, and DF relevant to f-CNs samples calculated by XPS and TGA. DF is expressed as the number of functionalizing groups per every 100 carbon atoms.

Sample	Atom C1s Abundance (%)	O1s Abundance (%)	N1s Abundance (%)	F1s Abundance (%)	DF (XPS) (%)	DF (TGA) (%)
p-SWCNTs	85.74	13.47	–	–	–	–
SWCNT-$C_6F_4CO_2H$	85.89	11.08	1.80	1.23	~1	~1
SWCNT-$C_6H_4CO_2H$	86.14	12.20	1.66	–	N.A.	1.5
p-MWCNTs	97.72	2.27	–	–	–	–
MWCNT-$C_6F_4CO_2H$	95.31	2.81	0.90	0.47	<<1	~1
MWCNT-$C_6H_4CO_2H$	92.90	5.22	1.66	–	N.A.	1.5
rGO	88.04	8.78	2.93	–	–	–
rGO-$C_6F_4CO_2H$	85.54	8.50	3.99	1.26	~1	~1
rGO-$C_6H_4CO_2H$	85.58	9.95	3.90	–	N.A.	1.5
G	87.06	12.51	–	–	–	–
G-$C_6F_4CO_2H$	84.43	12.40	1.71	1.45	~1	~1
G-$C_6H_4CO_2H$	84.45	14.16	1.40	–	N.A.	1.5

Another test very simple to carry out but which gave interesting results, was the assessment of the solubility of the functionalized materials in water. An aliquot of 2 mg of pristine and functionalized nanomaterials was dispersed in 2 mL of distilled water. The suspensions were sonicated for 30 minutes and then left to stand for 2 days. Figure 27 shows the behavior of p-SWCNTs, SWCNT-$C_6H_4CO_2H$ and SWCNT-$C_6F_4CO_2H$. After two days, the sample SWCNT-

$C_6H_4CO_2H$ (b) was still a suspension, whereas p-SWCNTs (a) and SWCNT-$C_6F_4CO_2H$ (c) precipitated. All other samples showed the same behavior, even though the most durable suspension obtained (visual judgment) was for the sample SWCNT-$C_6H_4CO_2H$. Other samples precipitated after 3/4 days.
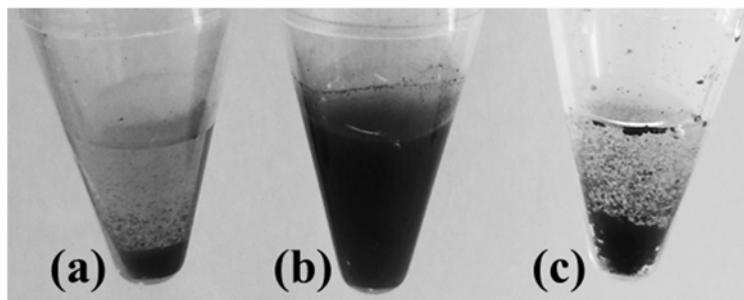

Figure 27: 2 mg of (a) p-SWCNTs, (b) SWCNT-$C_6H_4CO_2H$ and (c) SWCNT-$C_6F_4CO_2H$ dispersed in 2 mL of water.

UV-Vis-NIR for the sample SWCNT-$C_6H_4CO_2H$ confirmed the positive covalent functionalization of the substrate, since a flat line was obtained (without the absorption bands of the Van Hove singularities).

4.4. Conclusions

In this chapter we proved that the diazonium chemistry is an efficient way to covalently functionalize different kind of carbon nanosubstrates. SWCNTs, MWCNTs, rGO and graphene functionalized with 4-aminobenzoic acid gave good results in terms of degree of functionalization and solubility in aqueous solvent. SWCNT-$C_6H_4CO_2H$ resulted to be the best reactive material and its functionalization produced a very soluble compound in water. As expected, the functionalization with 4-amino-2,3,5,6-tetrafluorobenzoic acid was unsatisfactory. Probably, the presence of the four fluorine on the aromatic ring hindered the availability of the electrons to form the reactive radical diazonium intermediate. This result was in conflict with the result obtained for nitrene addition, where the presence of fluorine on the functionalizing molecule fostered

the formation of the azide and the subsequent nitrene intermediate. Another point which is worth stressing is the versatility of rGO. rGO reactions occurred in NMP and rGO reactions occurred in water in one-pot synthesis gave comparable results. The possibility to work in water in one-pot synthesis means little production of organic waste and easy work-up of reaction. On the other hand, SWCNTs remain the best conductive material tried. A tiny amount of functionalized SWCNTs is sufficient to get a very performing material. The choice between the different carbon substrates depends mostly on the final purpose.

CHAPTER 5

Non-covalent approach for the synthesis of single-walled carbon nanotubes-based sensitive materials
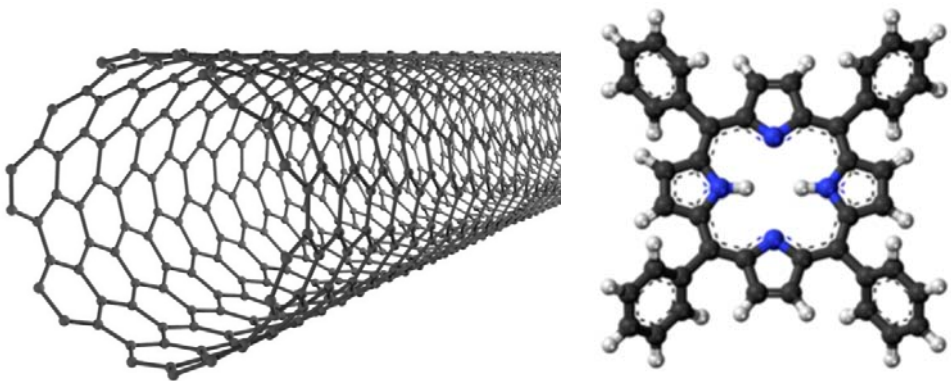
5.1. Introduction

In this chapter we describe the non-covalent functionalization of single-walled carbon nanotube with 5,10,15,20-Tetraphenyl-21H,23H-porphine (H_2TPP) and its metallo-derivatives 5,10,15,20-Tetraphenyl-21H,23H-porphine copper (II) (CuTPP) and 5,10,15,20-Tetraphenyl-21H,23H-porphine vanadium(IV) oxide (VOTPP) (Figure 28).
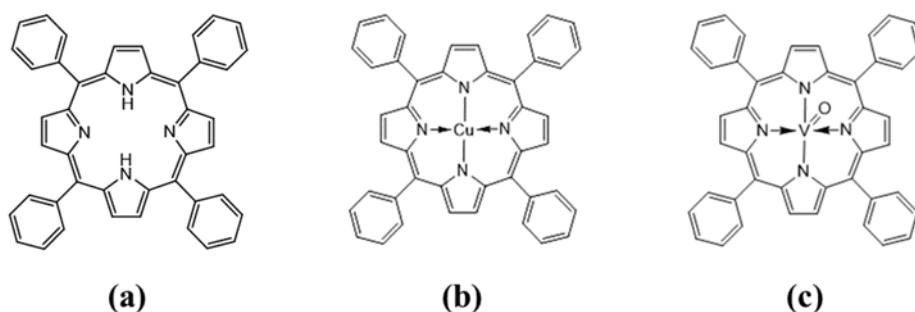

Figure 28: Chemical structures of porphyrins used: (a) H_2TPP, (b) CuTPP and (c) VOTPP.

Porphyrins are functional dyes with a variety of unique chemical, photophysical and biological properties. The basic porphyrin skeleton comprises four pyrrole rings linked via four methine (*meso*) carbons (Figure 29).
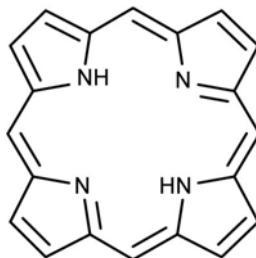

Figure 29: Basic porphyrin skeleton.

The nucleus of the macrocyclic system is a tetradentate ligand in which the maximum space available for a coordinated metal has a diameter of approximately 3.7 Å [85]. The free base porphyrin showed in Figure 29 can be modified by substituting the outer H atoms with molecules such as benzene. Another type of substitution replaces the central H atoms by any one of a variety of metals, thus changing the porphyrin from free base to metal salt [85]. Other kind of free base porphyrin modifications are known, but they are herein omitted for simplicity. In this thesis VOTPP was purchased by Sigma-Aldrich, whereas H_2TPP and CuTPP where synthesized in our laboratory. Almost all metals form complexes 1:1 with free base porphyrin. When coordination occurs, two protons are removed from the pyrrole nitrogen atoms, leaving two negative charges. In the case of Cu (II), when the divalent metal atom is chelated the resulting tetracoordinate chelate has no residual charge. Thanks to the aromatic character, porphyrins were exploited by Nakashima and co-workers to form by non-covalent interaction the first porphyrin-nanotube nanocomposite [86]. The macrocyclic organic molecule which have an extensive system of delocalized π electrons were capable of interacting with the π-system of SWCNTs.

Non-covalent functionalization of CNTs typically only requires mixing and sonication of CNTs with the functionalizing molecule. This has the advantage of being easy to execute, especially in the case of commercially available reagents.

5.2. Instruments

Porphyrins and SWCNT-porphyrin nanocomposites were characterized by the following techniques:

^{1}H-NMR spectroscopy

The ^{1}HNMR spectra were recorded at 25 °C with a spectrometer Bruker Avance DRX400. The samples were dissolved in $CDCl_3$ and analyzed in tubes of 5 mm. Chemical shifts are reported as δ values (ppm) and referred to the residual protons of deuterated chloroform.

FT-IR spectroscopy

The IR spectra were recorded at room temperature with a Perkin-Elmer Spectrum One spectrometer in Fourier transform interfaced with a personal computer. The spectra were recorded on films obtained by slow evaporation of the solvent on a KBr lamina.

UV-Vis spectroscopy

The UV-Vis absorption spectra were recorded at room temperature by a Perkin-Elmer Lambda 650 spectrophotometer interfaced with a personal computer. Sample solutions were examined in quartz cuvettes with 1 cm optical paths. N,N-dimethylformamide (DMF) was used as solvent with a samples concentration of $3 \cdot 10^{-6}$ M.

Fluorescence spectroscopy

Fluorescence spectra were collected at room temperature using a Fluorolog Horiba Jobin Yvon spectrophotometer into quartz cuvettes of one centimeter. The solvent was DMF. Samples concentration was $3 \cdot 10^{-6}$ M.

Micro-Raman spectroscopy

The micro-Raman analysis were carried out using a Renishaw Raman Invia instrument. The instrument was equipped with a 1800 grooves/mm diffraction grating, a CCD detector, and a 50X magnifying lens. The Raman spectra were acquired with a laser excitation at 532 nm.

Thermogravimetry (TGA)

Thermograms were collected using a Mettler Toledo TGA/SDTA 851 analyzer by heating samples at 10 °C/min from 50 to 900 °C under nitrogen atmosphere.

5.3. Materials

SWCNTs were purchased from Nano-C (Purified PT25 with an average <1 micron in length) and used without further purification.

Benzaldehyde, pyrrole and propionic acid were purchased from Sigma-Aldrich. They were used from a freshly opened bottle. Copper(II) acetate 98% and 5,10,15,20-Tetraphenyl-21H,23H-porphine vanadium(IV) oxide were purchased from Sigma-Aldrich and used as received. All solvents were purchased from Sigma-Aldrich and used without any purification.

5.3.1. Synthesis of 5,10,15,20-Tetraphenyl-21H,23H-porphine (H₂TPP)

250 mL of propionic acid were brought to reflux (ca. 141 °C) in a 500 mL round-bottom flask fitted with a condenser. Then 7.3 mL (72 mmol) of benzaldehyde and 5 mL (72 mmol) of freshly distilled pyrrole were added (Scheme 1).
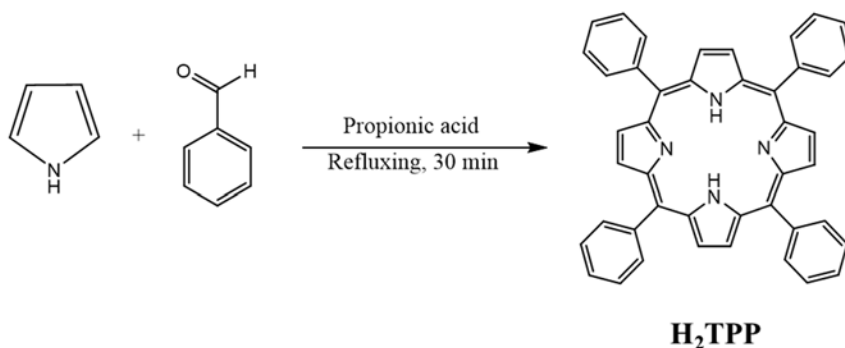
Scheme 1: Schematic reaction of the synthesis of 5,10,15,20-Tetraphenyl-21H,23H-porphine (H₂TPP). Stoichiometric factors are omitted for simplicity.

The reaction mixture was left refluxing for 30 minutes. After cooling to room temperature, the mixture was poured in a flask containing 250 mL of methanol under stirring. Then the mixture was cooled in an ice bath for two hours. The deep-purple crystals obtained were filtered using a Büchner funnel (Figure 30). The solid was washed with five 10 mL portions of methanol and five 10 mL portions

of boiling-hot distilled water. The crystals were air-dried. The yield was 22% which was in perfect accord with literature values [88]. The compound was pure enough for the subsequent metalation.

Figure 30: H_2TPP crystals.

5.3.2. Synthesis of 5,10,15,20-Tetraphenyl-21H,23H-porphine copper (II) (CuTPP)

The most general and convenient method for the metalation of porphyrins is the procedure employing DMF. An amount of 0.9 g (1.46 mmol) of H_2TPP was added to 150 mL of DMF previously brought to reflux (ca. 150 °C). H_2TPP was allowed to dissolve for few minutes, then 0.6 mg (3.30 mmol) of copper(II) acetate were added (Scheme 2). The proceeding of the reaction was checked by TLC. The reaction mixture was allowed to react for 3 hours. The mixture was then cooled at room temperature, after that, 150 mL of distilled water were added to foster the precipitation of CuTPP. The precipitate was filtered with a Büchner funnel (Figure 31) and washed thoroughly with water. The reddish-brown material was air-dried and the yield was 100%. The crude material could be further purified, however we judged it pure enough for our purpose.
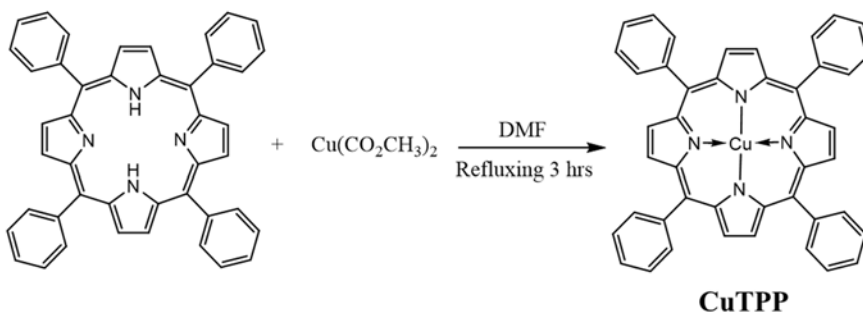
Scheme 2: Schematic reaction for the synthesis of 5,10,15,20-Tetraphenyl-21H,23H-porphine copper (II) (CuTPP).

Figure 31: CuTPP crystals.

Figure 32 reports the ^{1}H NMR spectra of H_2TPP and CuTPP. The peaks at 1.56 and 7.29 ppm are due to H_2O and CHCl$_3$, respectively. The peak at -2.74 ppm is due to the protons of the center of the molecule. When the complexation occurs, the NMR peaks are not observable as a result of the extreme broadening and shifting of their signals from the paramagnetic metal center. Other signals are due to the other protons present on the porphyrin ring. The ^{1}H NMR spectra were comparable with those of literature [89].
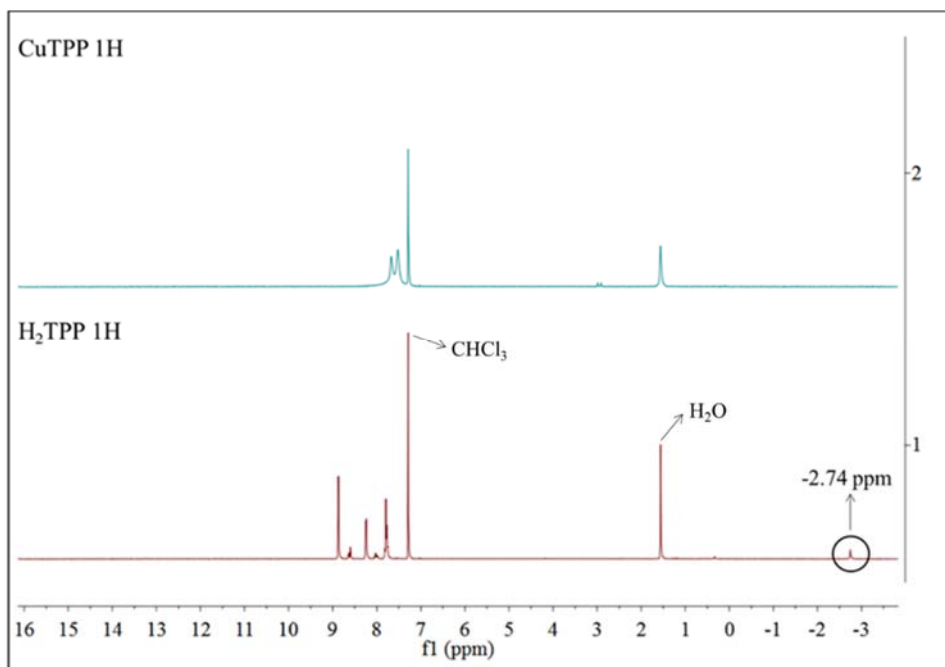
Figure 32: ^{1}H NMR spectra of CuTPP (top) and H$_2$TPP (bottom).

Also the FT-IR spectra confirmed the synthesis of H$_2$TPP and CuTPP. In (Figure 33) are reported the spectra of H$_2$TPP (in blue) and CuTPP (in pink). Examining only the characteristic bands at 3315 cm^{-1} and around 1000 cm^{-1}, it is possible to state that the two reactions occurred correctly. The band at 3315 cm^{-1}, reported on the bottom left side of Figure 33 (graph (a)) can be attributed to the stretching of N-H. The band disappears when the porphyrin is metaled. The band at 1001 cm^{-1} for H$_2$TPP is shifted to 1005 cm^{-1} for CuTPP with a considerable increase of the intensity (bottom right side of Figure 33 (graph (b)). This indicates the formation of the complex.
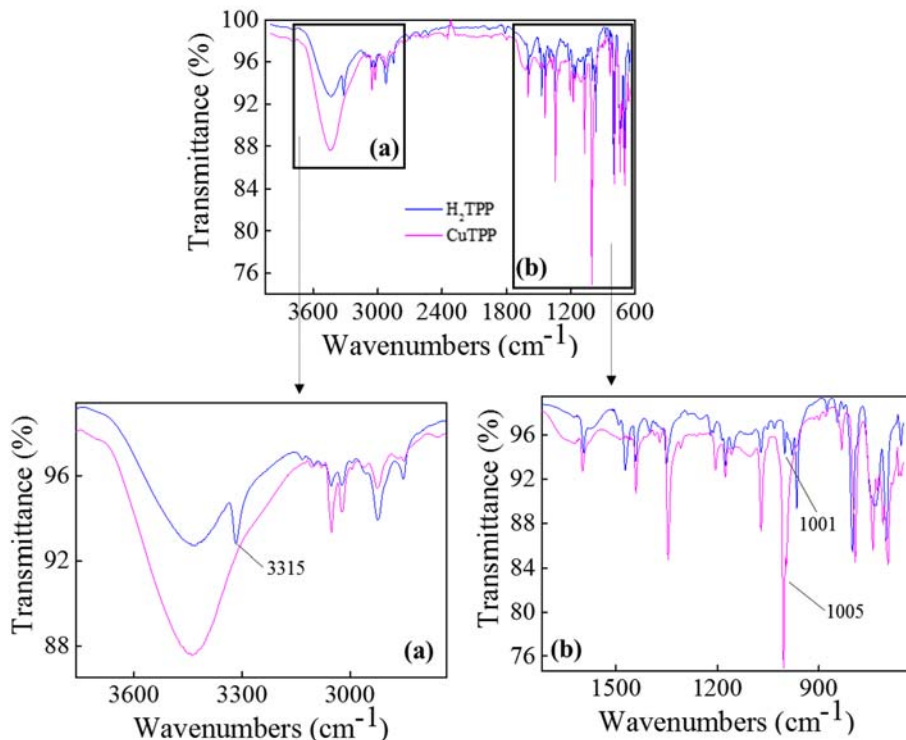
Figure 33: FT-IR spectra of H_2TPP (blue line) and CuTPP (pink line). The regions (a) and (b) highlighted with a black frame in the figure of the top are magnified in the two figures of the bottom.

Also UV-Vis and fluorescence spectroscopy confirmed the success of the reactions. Figure 34 shows the absorption spectrum of H_2TPP (a) and CuTPP (b).
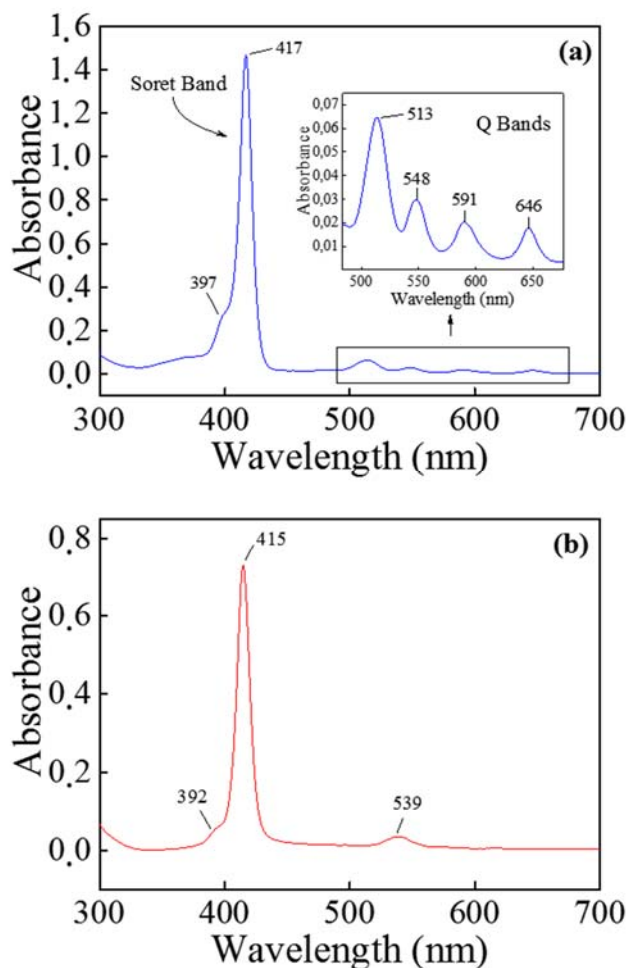
Figure 34: UV-Vis absorption spectrum of (a) H_2TPP and (b) CuTPP.

The electronic absorption spectrum of a typical porphyrin consists of a strong transition to the second excited state (S0 → S2) at about 400 nm (the Soret or B band) and a weak transition to the first excited state (S0 → S1) at about 550 nm (the Q band). The Soret and the Q bands both arise from π-π* transitions and can be explained by considering the four frontier orbitals (HOMO and LUMO orbitals, the Gouterman four orbital model). According to this theory, the absorption bands in porphyrin systems arise from transitions between two HOMOs and two LUMOs, and it is the identities of the metal center and the substituents on the ring that affect the relative energies of these transitions. The Soret band of CuTPP is

blu shifted of 2 nm (415 nm) if compared to the Soret band of H_2TPP (417 nm). This occurs because the d^9 Cu(II) ion in CuTPP has filled d_π orbitals which significantly interact with the porphyrin π^* orbitals via metal to ligand π-backbonding. H_2TPP also showed four Q bands, unlike CuTPP which only showed one Q band. This was due to the lower-order symmetry of H_2TPP than CuTPP.

CuTPP is not fluorescent, however, the emission spectra was recorded the same to have the confirmation. Figure 35 reports the fluorescent spectrum of H_2TPP compared to that of CuTPP obtained exciting the samples to 415 nm. H_2TPP was fluorescent, whereas CuTPP did not show any fluorescence, expect for a only very weak band at 648 nm as shown in the inset of Figure 35. This band was probably due to some impurity of H_2TPP.
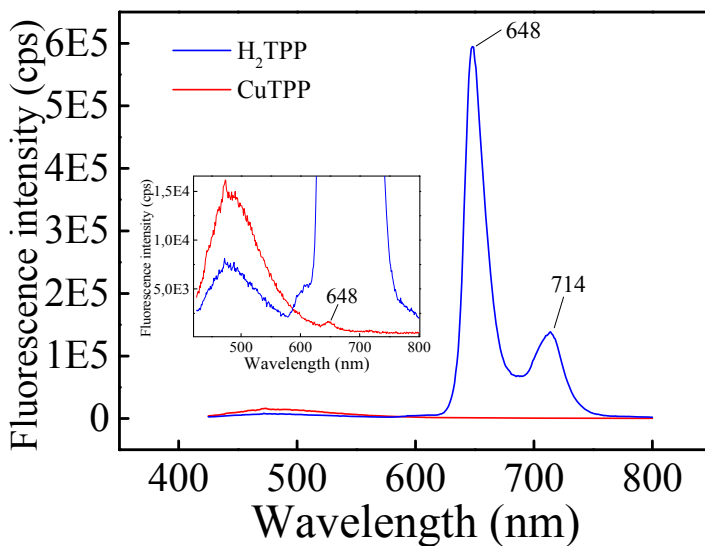

Figure 35: Fluorescence spectra of H_2TPP (blue line) and CuTPP (red line).

5.3.3. Functionalization of SWCNTs with 5,10,15,20-Tetraphenyl-21H,23H-porphine, 5,10,15,20-Tetraphenyl-21H,23H-porphine copper (II) and 5,10,15,20-Tetraphenyl-21H,23H-porphine vanadium(IV) oxide

SWCNTs/porphyrin dispersions were prepared by mixing 0.5 mg (42 μmol C) of SWCNTs with 200 mg (ca. 0.3 mmol) of porphyrin in 1 mL of DMF.

Procedure: 0.5 mg of SWCNTs were sonicated for 30 minutes in 1 mL of DMF, then 200 mg of H_2TPP, CuTPP or VOTPP were added. The mixtures were sonicated for 1 hour and used without further treatments.

The final samples were called: SWCNT-H_2TPP, SWCNT-CuTPP and SWCNT-VOTPP.

Unlike SWCNT-H_2TPP and SWCNT-CuTPP, SWCNT-VOTPP was characterized by only FT-IR and Raman spectroscopy. SWCNT-H_2TPP and SWCNT-CuTPP were characterized by Raman, FT-IR, UV-Vis, Fluorescence and TGA.

5.4. Results and discussion

Figure 36 and Figure 37 show the Raman spectra of SWCNT-CuTPP and SWCNT-VOTPP. Unfortunately, we were not able to collect a satisfying spectrum of SWCNT-H_2TPP because of the high fluorescence of H_2TPP. Nevertheless, the compound SWCNT-H_2TPP was characterized by FT-IR, Fluorescence, UV-Vis and TGA. Figure 36 reports the comparison of Raman spectra of p-SWCNTs, CuTPP and SWCNT-CuTPP. As the ratio porphyrin/SWCNTs was 400 by weight, the Raman signals of SWCNT-CuTPP were dominated by the signals of crystalline CuTPP. However, if we look closely at insets (a) and (b) we can observe the slight effect of the presence of SWCNTs. In particular, the inset (a) shows the amplification of the zone comprising the D and G bands. We can see how the peaks of the G band of p-SWCNTs (1592 cm^{-1}, 1570 cm^{-1}) are retained by the SWCNT-CuTPP sample (short dot arrows of inset (a)). Also the D band, visible in the inset (b), is retained by SWCNT-CuTPP.
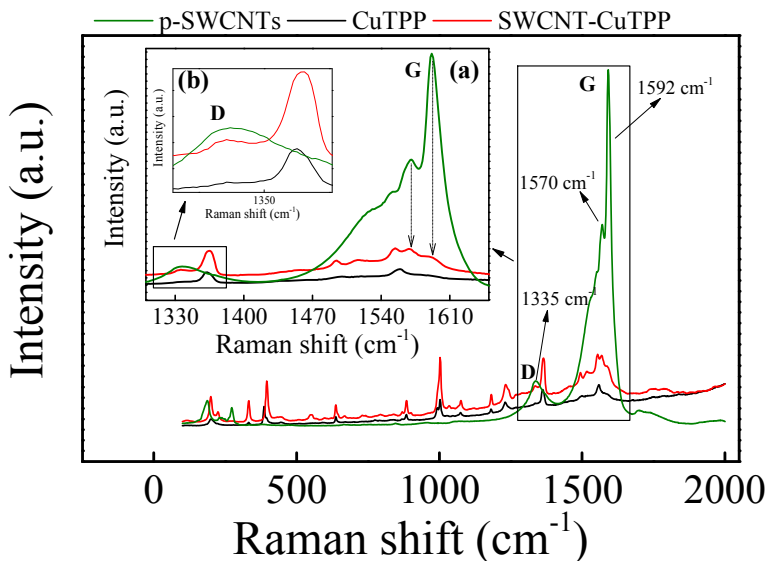
Figure 36: Raman spectra of p-SWCNTs (green line), CuTPP (black line) and SWCNT-CuTPP (red line).

Although these positive results, the analysis of Raman spectra did not give information about the effective interaction (π-π stacking) of CNTs with porphyrin. Moreover, no significant Raman shifts were observed. One of the most challenging issue about the functionalization of carbon nanotubes is the assessment of the effectiveness of functionalization. This matter is controversial also for covalent functionalization where several techniques have to be used to unequivocally state that a structural modification occurred. A TEM or HRTEM analysis could confirm the interaction of CNTs with porphyrin. However, at this stage of the thesis the TEM analysis was not available. Looking at literature results, several studies have been conducted regarding the non-covalent functionalization of CNTs with free base or metaled porphyrins. An interesting results that turns out is the better interaction of H_2TPP with CNTs respect to the metaled porphyrin [90].

Figure 37 shows the Raman spectra of p-SWCNTs, VOTPP and SWCNT-VOTPP. No changes in the SWCNT-VOTPP spectrum are noted respect to the VOTPP spectrum.
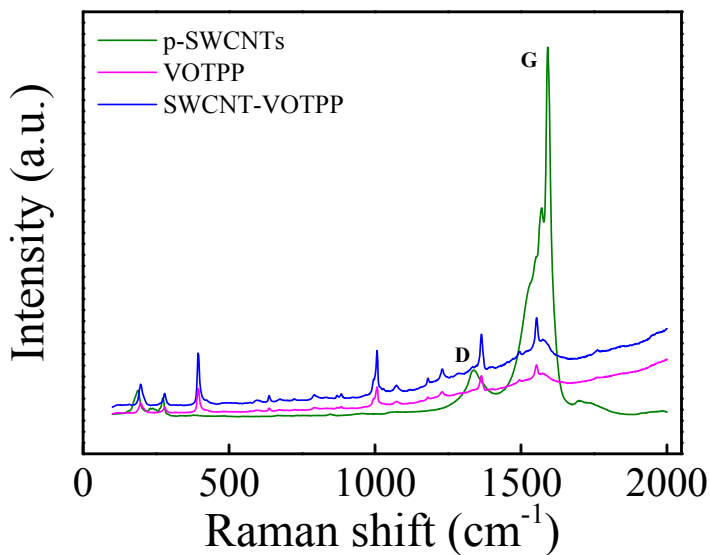

Figure 37: Raman spectra of p-SWCNTs (green line), VOTPP (pink line) and SWCNT-VOTPP (blue line).

The FT-IR spectra of SWCNT-CuTPP, SWCNT-VOTPP and SWCNT-H_2TPP are shown below in Figure 38.
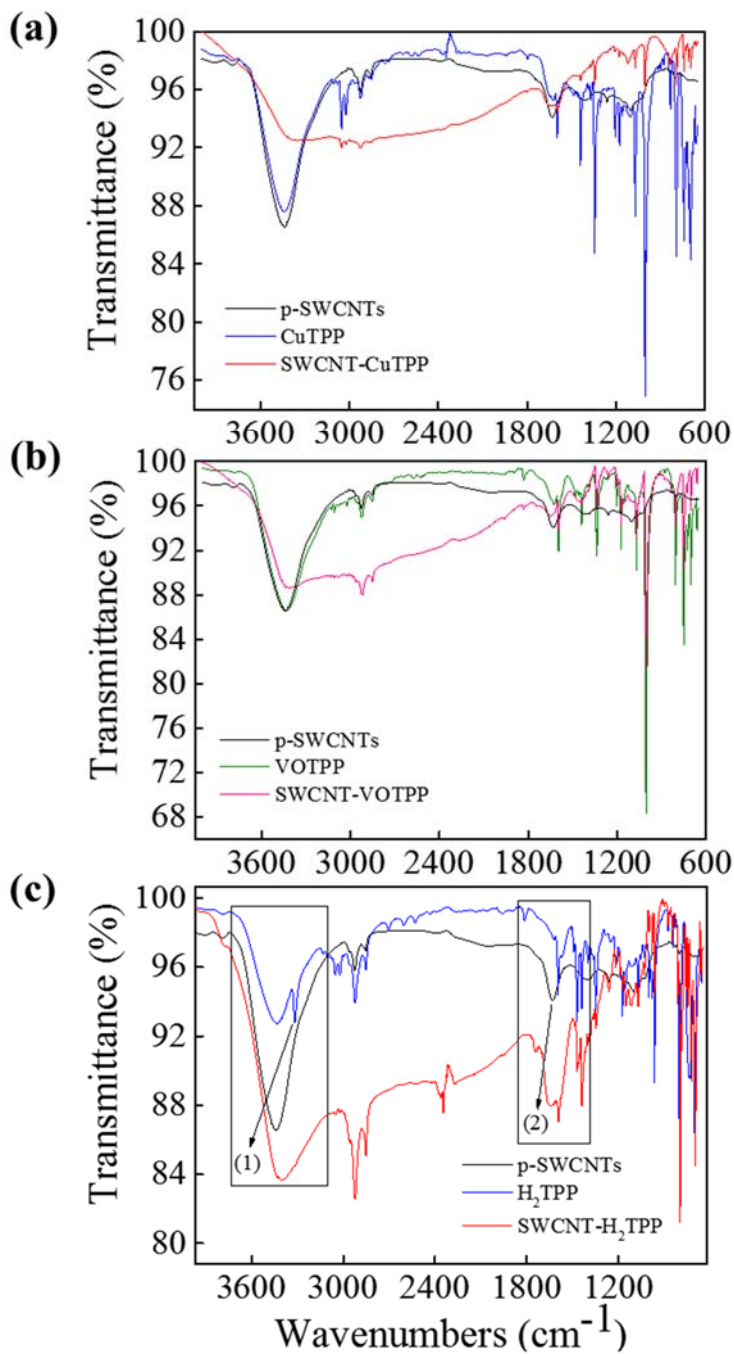
Figure 38: FT-IR spectra of (a) SWCNT-CuTPP, (b) SWCNT-VOTPP and (c) SWCNT-H$_2$TPP.

The FT-IR spectrum of p-SWCNTs were poorly resolved bands, however their contribution was well visible in the case of SWCNT-H$_2$TPP. SWCNT-CuTPP and SWCNT-VOTPP instead, did not show significant contributions of p-SWCNTs. Figure 38c shows the FT-IR profiles of p-SWCNTs, H$_2$TPP and SWCNT-H$_2$TPP. In the black frame on the left of Figure 38c, with the number 1, is highlighted the disappearance of the band at 3315 cm^{-1} characteristic of the N-H stretching. Moreover, the p-SWCNTs bands depicted as 2, is clearly visible also in the SWCNT-H$_2$TPP sample (red line) whereas is absent in the crystalline H$_2$TPP (blue line). The disappearance of the band at 3315 cm^{-1}, can be possibly attributed to the broadness of the SWCNT-H$_2$TPP band which hides the N-H stretch band of H$_2$TPP.

The UV-Vis analysis (Figure 39) did not show any particular evidence of CNTs/porphyrin interaction except for the reduction of the intensity of the Soret band both for SWCNT-CuTPP and SWCNT-H$_2$TPP respect to CuTPP and H$_2$TPP, respectively.
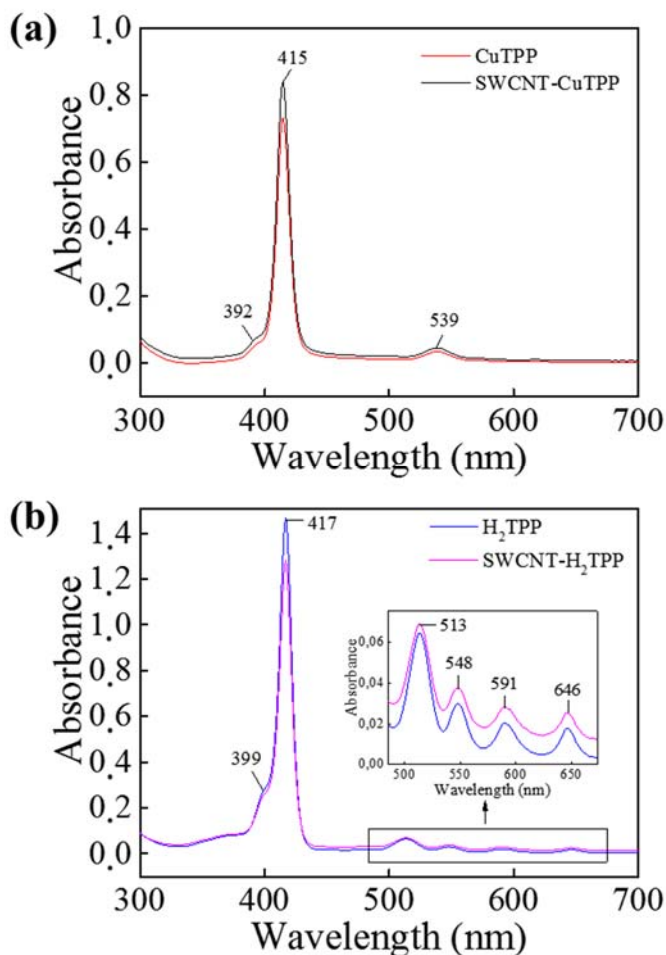
Figure 39: UV-Vis spectra of (a) CuTPP and SWCNT-CuTPP and (b) H_2TPP and SWCNT-H_2TPP.

CuTPP is not fluorescent, however the emission spectrum was recorded the same. It is interesting to note that the weak band at 648 nm, and attributed to H_2TPP impurity, disappears for the sample SWCNT-CuTPP. The quenching of fluorescence by SWCNTs is largely reported in literature [87] and gives direct evidence of the interaction of metaled porphyrin with CNTs. Unfortunately, this evidence cannot be exploited for SWCNT-H_2TPP. The small amount of SWCNTs respect to H_2TPP is not sufficient to completely overwhelm the strong signals of

the free base porphyrin (Figure 40). However, a slight decrease in the intensity of the bands at 648 nm and 714 nm can be observed.
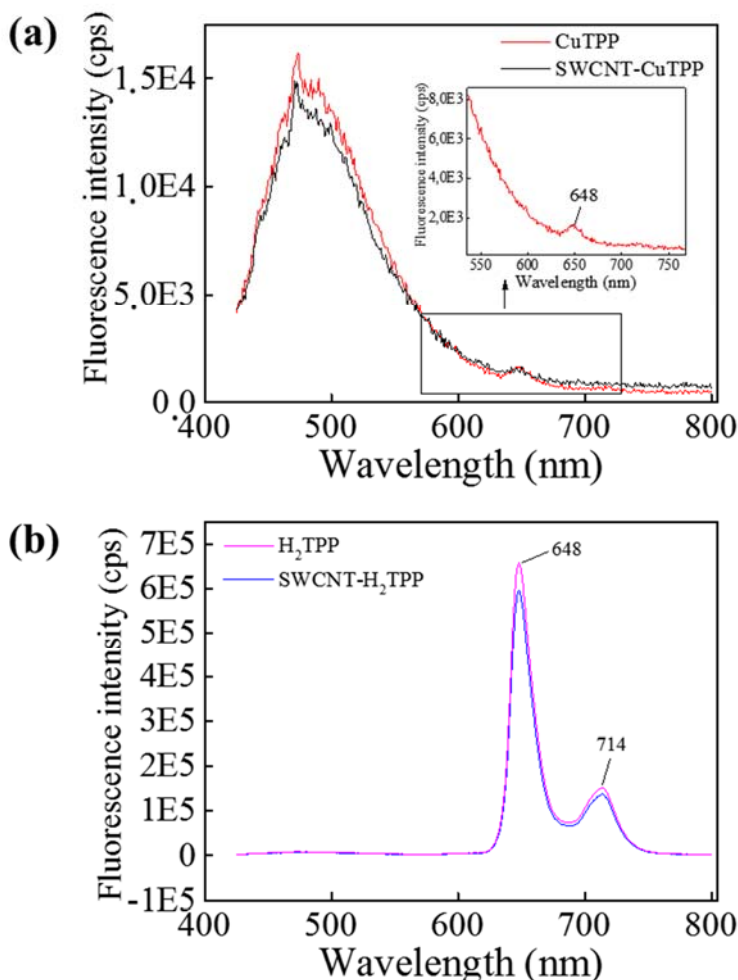
Figure 40: Fluorescence spectra of (a) CuTPP and SWCNT-CuTPP and (b) H$_2$TPP and SWCNT-H$_2$TPP.

Figure 41 shows the thermogravimetric profiles of CuTPP, SWCNT-CuTPP, H$_2$TPP and SWCNT-H$_2$TPP. From the analysis of the first derivative of weight loss (not shown here) we can deduce that the presence of CNTs stabilizes the compound SWCNT-H$_2$TPP of about 10 °C. In fact, H$_2$TPP (Figure 41b) has a weight loss at 485 °C, whereas SWCNT-H$_2$TPP shows the weight loss related to

the decomposition of porphyrin at 496 °C. SWCNT-CuTPP, instead, does not seem to be altered by the presence of SWCNTs. In fact, for both CuTPP and SWCNT-H$_2$TPP the weight loss related to the decomposition of porphyrin is around 530 °C. This could be due to the fact that the free base porphyrin interact better with CNTs if compared to metaled porphyrin as mentioned previously. The weight loss around 100 °C both for SWCNT-CuTPP and SWCNT-H$_2$TPP was due to the presence of the solvent in the samples, unlike CuTPP and H$_2$TPP which were analyzed as powder.
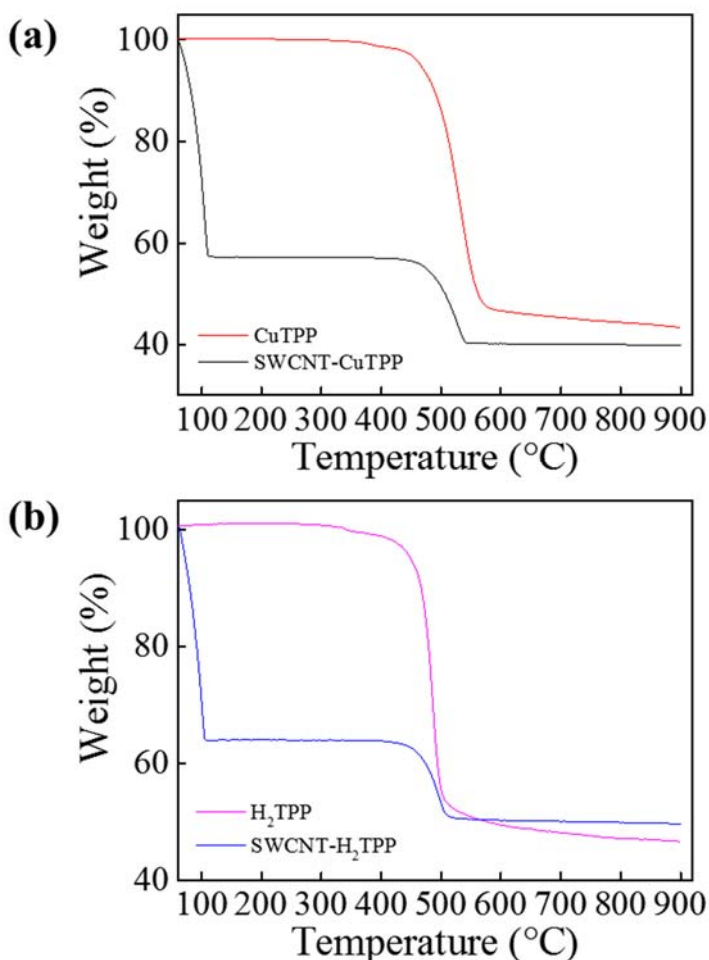
Figure 41: TGA profiles (under nitrogen) of (a) CuTPP and SWCNT-CuTPP and (b) H$_2$TPP and SWCNT-H$_2$TPP.

5.5. Conclusions

The non-covalent functionalization of SWCNTs with different kind of porphyrins aimed to increase the sensor sensitivity and selectivity.   .

The chemical characterization of SWCNT/porphyrin compounds gave information concerning the interaction of SWCNTs with porphyrins. Unfortunately, working with a high ratio of porphyrins respect to SWCNTs, the influence of CNTs on the porphyrins properties and vice versa was not immediately visible. However, with these analysis we proved that some electronic interactions between porphyrins and SWCNTs occurred. In the next chapter interesting results regarding the performances of non-covalently functionalized SWCNTs will be presented.

CHAPTER 6

Ammonia and trimethylamine:

Gas sensing tests
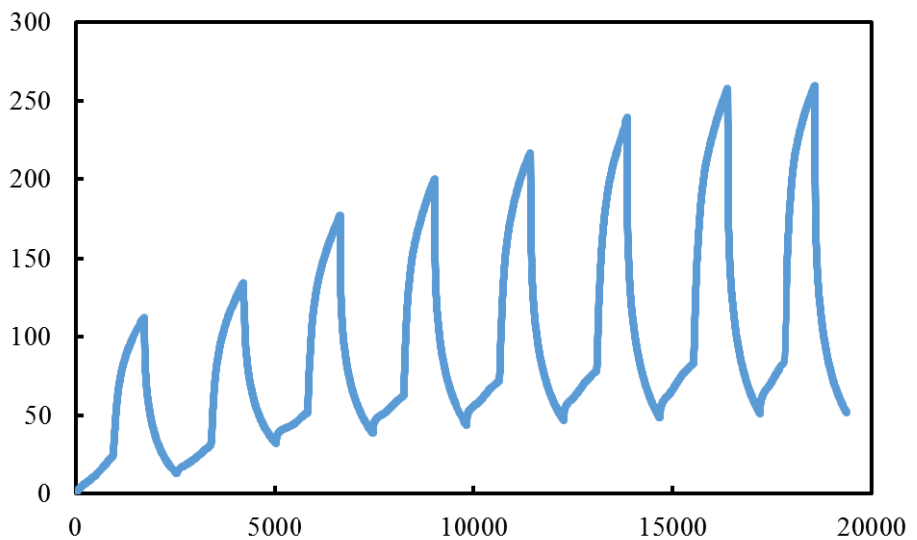
6.1. Introduction

The materials synthesized as described in Chapters 4 and 5 were used to fabricate sensors and tested for sensitivity to ammonia and trimethylamine using a dynamic and a semi-static method. The dynamic method was based on the continuous delivery of nitrogen as carrier gas and the addition of different aliquots of NH_3 or TMA gas every 400 seconds. On the contrary, the semi-static method entailed the exposure of sensors to a homogeneous atmosphere of the target analytes (NH_3 or TMA) at different concentrations. All measurements were carried out at room temperature. In both cases, the response of the sensors was given as $\Delta R/R_0$ (%).

6.2. Gas sensing tests: Dynamic method

6.2.1. Fabrication of the electrodes array and sensitive films

An aluminum mask was used when thermally evaporating (Angstrom Engineering) 14 gold electrodes (1 mm gap) on a microscope glass slide (VWR) previously washed in acetone and dried. A 10 nm layer of chromium (99.99%, R.D. Mathis) was deposited first to allow the subsequent adhesion of 100 nm of gold (99.99%, R.D. Mathis). A quantity of 2 mg of p-CNTs or functionalized carbon nanotubes (f-CNTs) was dispersed in 4 mL of o-DCB by sonication in an ultrasonic bath for 1-2 min at room temperature. The resulting dispersion was then drop-cast onto the electrodes and dried under vacuum to remove the solvent. Typically, the deposition of three to five 1 μL drops was necessary to obtain the target resistance in the range 100-150 KΩ (Fluke 287 True RMS Multimeter). The 14 electrode array was used to test different sensing materials under identical conditions and to identify the best performing material.

6.2.2. Gas delivery system

The sensor array was placed in a PTFE flow chamber connected to a gas mixing and delivery system. This system consisted of two digital mass flow controllers (MFC) (Sierra Instruments), one used to control the flow (0.5-4 mL/min) of NH_3 or TMA in nitrogen (1% NH_3 in N_2 and 1% TMA in N_2 custom-ordered from Airgas) and the other to dilute the target gas with N_2 (0.5-1 L/min). The analytes were delivered to the device at various concentrations (5-80 ppm) for 100 s at a time. The sensor recovery was carried out using nitrogen at room temperature for 400 s after each exposure.

6.2.3. Measurements of device response

An EmStat-MUX handheld potentiostat (PalmSens Instruments) was used to determine resistance values from the sensor array. For this purpose, the current was measured with the PSTrace software (PalmSens) while applying a constant potential (0.1 V) between the electrodes and resistance was calculated as the voltage to current ratio. The response of each array element was reported as percentage change in resistance, and the response was normalized for the initial resistance (R_0) to better compare results from different sensors. If R is the maximum resistance achieved during exposure to NH_3 or TMA for 100 sec., $\Delta R/R_0$ was therefore taken as the sensor response. All reported responses are the average of three replicate sensors for each sensing material. Data were used as obtained, without any fitting or baseline correction.

6.2.4. Results and discussion

Preliminary measurements at room temperature were carried out with sensor arrays to compare sensitivities of SWCNTs and MWCNTs toward NH_3 (Figure 42a) and MWCNTs toward TMA (Figure 42b. Detailed responses of SWCNTs toward TMA will be shown later). Even though MWCNTs were far less sensitive

than SWCNTs for both analytes, it was interesting to note how the functionalization improved the sensing signal of f-MWCNTs with respect to p-MWCNTs, which were insensitive to any concentration of analyte delivered on the system. In real conditions, sensors are prone to many possible interferents (both chemical and physical), and our result suggests that p-MWCNTs might be used as a reference blank to remove at least part of the interferences. Conversely, p-SWCNTs showed a response in the range of interest.
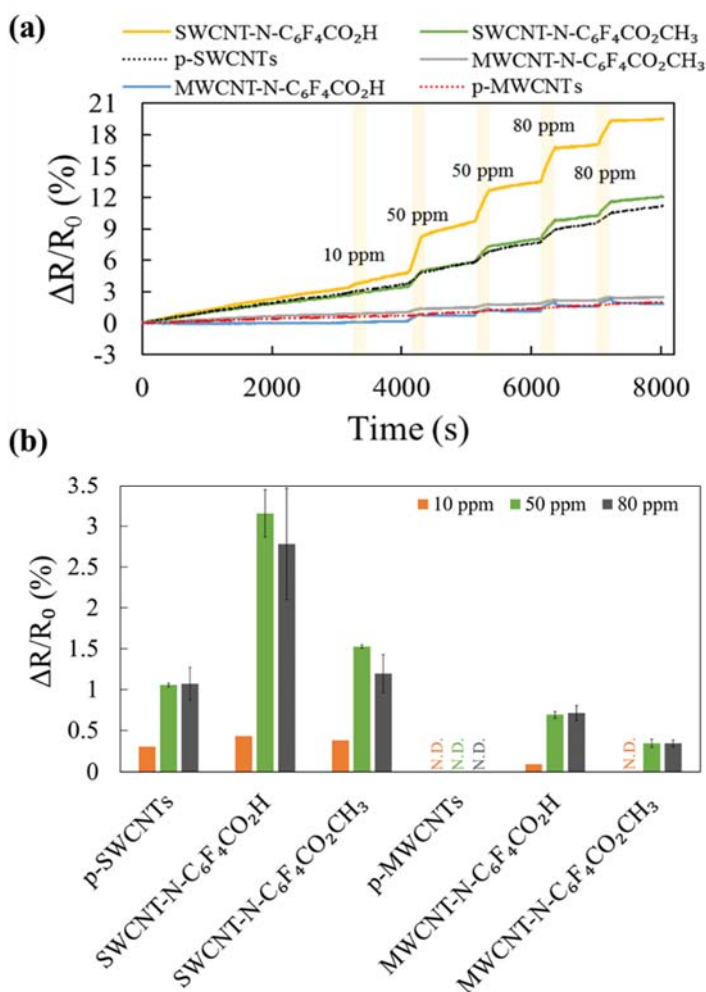

Figure 42: (a) Resistance change profiles of p-SWCNTs, p-MWCNTs, f-SWCNTs and f-MWCNTs in response to increasing concentrations of NH_3. The

electrical response to TMA (not reported here) showed similar profiles.. Both NH_3 and TMA were diluted with N_2. Analyte exposure time: 100 s. Recovery time under nitrogen at room temperature: 400 s. b) Bar graphs of the sensors responses. The error bars are the standard deviation. (N.D. Not Detectable)

As we will see better later in the text, all sensor responses saturated at a concentration of 40 ppm. $SWCNT-N-C_6F_4CO_2H$ and $SWCNT-N-C_6F_4CO_2CH_3$ responses were 2.5 and 5 times greater than those of f-MWCNTs to 40 ppm of TMA. The superior performance of f-SWCNTs was not surprising as the CNTs' band gap decreases with increasing diameter. For this reason, MWCNTs have a predominantly metallic character and a conductivity that is hard to quench by exposure to a gas. Functionalization of both SWCNTs and MWCNTs with 4-azido-2,3,5,6-tetrafluorobenzoic acid resulted in a superior sensitivity than functionalization with methyl 4-azido-2,3,5,6-tetrafluorobenzoate. This result was likely related to the strong Brønsted acid/base interaction of the carboxylic acid moiety with the lone-pair of the electron donor NH_3 and TMA. Another issue to be considered is that the estimated DF was lower in $SWCNT-N-C_6F_4CO_2CH_3$ and $MWCNT-N-C_6F_4CO_2CH_3$ than in $SWCNT-N-C_6F_4CO_2H$ and $MWCNT-N-C_6F_4CO_2H$ (i.e. both <1% compared to 1.2% in $SWCNT-N-C_6F_4CO_2H$ and 1.3% in $MWCNT-N-C_6F_4CO_2H$). This reduced the sensor response as only the less active (non-acidic) sites were available for the interaction with the amine molecules. Another fact which draws attention is the increase of the resistance upon analyte exposure. This increase in resistance can be explained considering the electronic nature of CNTs and their mechanisms of charge transfer. The p-SWCNTs have random chirality statistically yielding 1/3 of metallic SWCNTs and 2/3 of semiconducting tubes [91, 92] and under ambient conditions are p-type semiconductors. In this work, no effort was made to separate different types of SWCNTs. In metallic carbon nanotubes, the charge transfer from NH_3 or TMA to nanotubes is not expected to induce large changes in conductivity. Conversely, in the p-type semiconducting SWCNTs the interaction with the donor molecules NH_3 and TMA will have a larger effect on the electrical properties by decreasing

112

the conductance of the network, as the charge transfer from the amines effectively refiles the holes of the valence band. This mechanism explains why p-SWCNTs are sensitive to NH_3 and TMA. Our modification of the carbon nanotubes surface improved the interactions of the SWCNTs enhancing the electrical response. The interaction of NH_3 or TMA with the perfluorinated functionalizing molecule transforms the organic molecular component into an anion capable to deplete or trap the holes of carbon nanotubes and increase resistance.

f-SWCNTs were investigated in greater detail as they appeared the most promising candidate for the realization of NH_3/TMA gas sensors. In particular, SWCNT-N-$C_6F_4CO_2H$ resulted the best material. SWCNT-$C_6F_4CO_2H$ was tested in the range 5-70 ppm and surprisingly sensors produced with this material gave a response comparable to that of p-SWCNTs. This anomalous behavior could be due to the formation of a π-π interaction between the nanotube and functionalizing molecule following the reaction between SWCNTs and the diazonium salt, instead of the expected covalent bond.

Figure 43 shows the response of SWCNT-N-$C_6F_4CO_2H$, SWCNT-$C_6F_4CO_2H$ and p-SWCNTs to a 100 s exposure of NH_3 and TMA over the range 5-70 ppm. The higher sensitivity of the sensors toward TMA compared to NH_3 can be possibly ascribed to its more basic nature, indicating a more favored lone electron pair interaction with SWCNTs and/or the pendant N-$C_6F_4CO_2H$ groups [93].
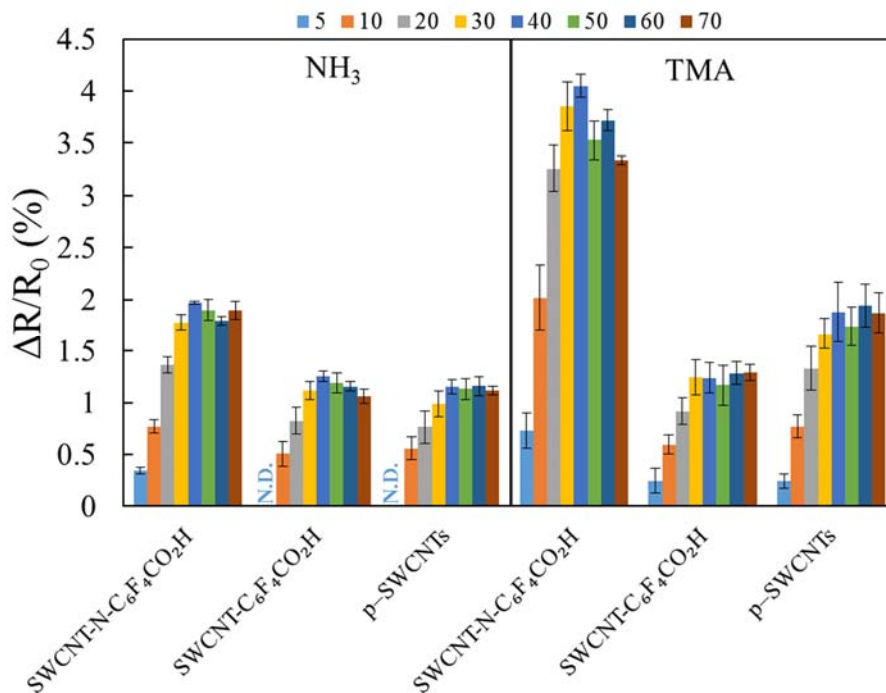
Figure 43: Resistance variations of pristine and functionalized SWCNTs upon 100 s exposures to different concentrations (expressed in the legend in ppm) of TMA in N_2. (N.D. Not Detectable)

Figure 43 shows that all sensors provide the highest response at a concentration of 40 ppm, then the response remain either stable or decrease. Figure 44 gives the calibration curves of SWCNT-N-$C_6F_4CO_2H$ responding to NH_3 and TMA in the range 5-40 ppm.
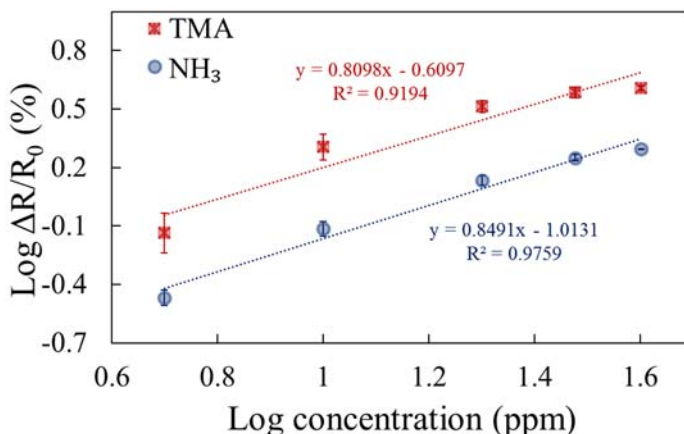
Figure 44: Calibration curve of SWCNT-N-$C_6F_4CO_2H$ at a single exposure of various concentrations of NH_3 and TMA in N_2. (Dotted line: linear fit).

Figure 45 shows the response of three replicate sensors with f-SWCNTs exposed to 5, 10, and 40 ppm of TMA for 100 s each in nitrogen (3 exposures for each concentration).
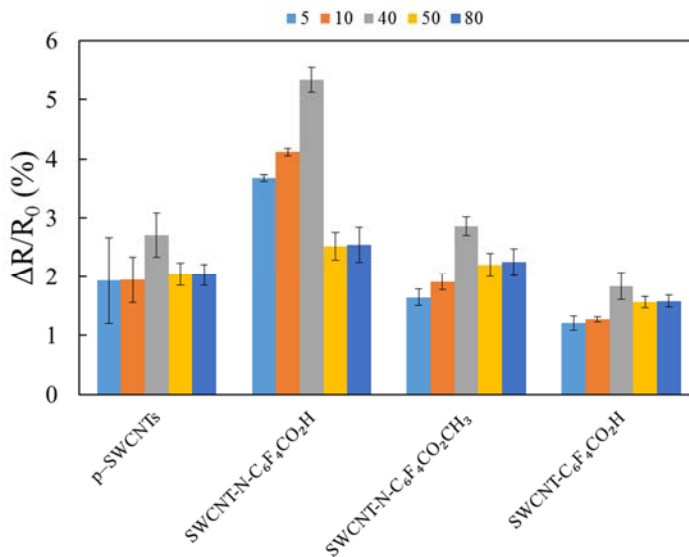
Figure 45: Illustrative responses of pristine and functionalized SWCNTs to three 100 s exposures of various concentrations (ppm expressed in legend) of TMA in

N_2. N_2 was delivered on the sensors between each vapor exposure for 400 s. Error bars are the pooled variance.

f-SWCNTs showed a better reproducibility than the corresponding p-SWCNTs. Figure 46 shows typical responses of rGO-based sensors (rGO, rGO-N-$C_6F_4CO_2H$ and rGO-$C_6F_4CO_2H$) exposed to different concentrations of NH_3 or TMA.
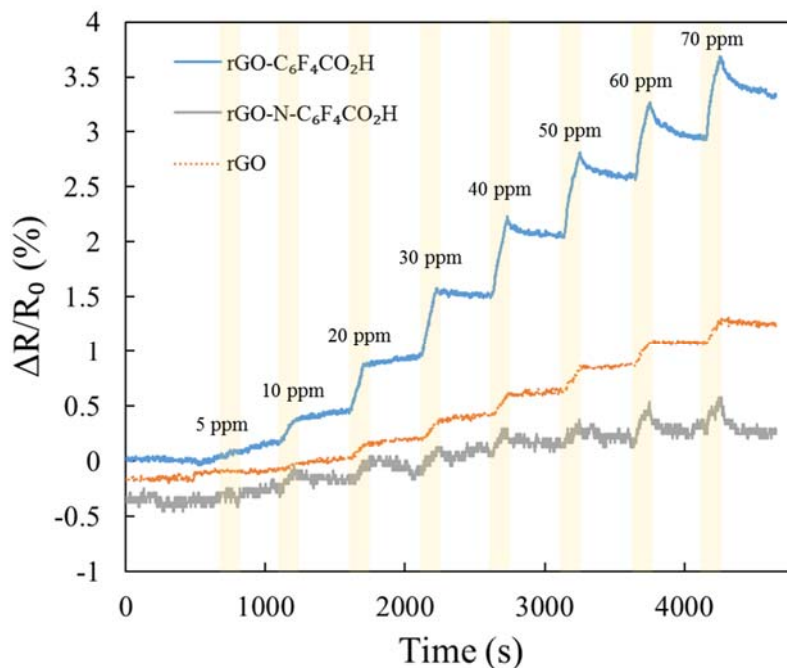
Figure 46: Example of electrical response of rGO-based samples exposed to different concentrations of NH_3 in N_2. Responses to TMA showed the same profile.

The pendant -N-$C_6F_4CO_2H$ produced a poor response and a very noisy signal when used to functionalize rGO and the highest sensitivity both for NH_3 and TMA when combined with SWCNTs. The reaction *via* nitrene addition resulted in an effective functionalization but the electrical response was unsatisfactory. This can be ascribed to the different functionalization mechanism of nitrene respect to diazonium. As briefly described in Chapter 4, the [2+1] cycloaddition of nitrene

entails the disruption of the extended π-conjugation of the graphene sheet, causing a reduction in the conductivity of the system. It is probable that the covalent functionalization of rGO reduced its conductivity leading to a material less sensitive to volatile analytes. SWCNTs, inherently more conductive than rGO, were probably less affected by the surface modification and, on the contrary, the functionalization improved the doping of nanotubes making them more sensitive to volatiles. Figure 47 shows the response of rGO and rGO-N-$C_6F_4CO_2H$ exposed for 100 s to different concentrations of NH_3 and TMA.
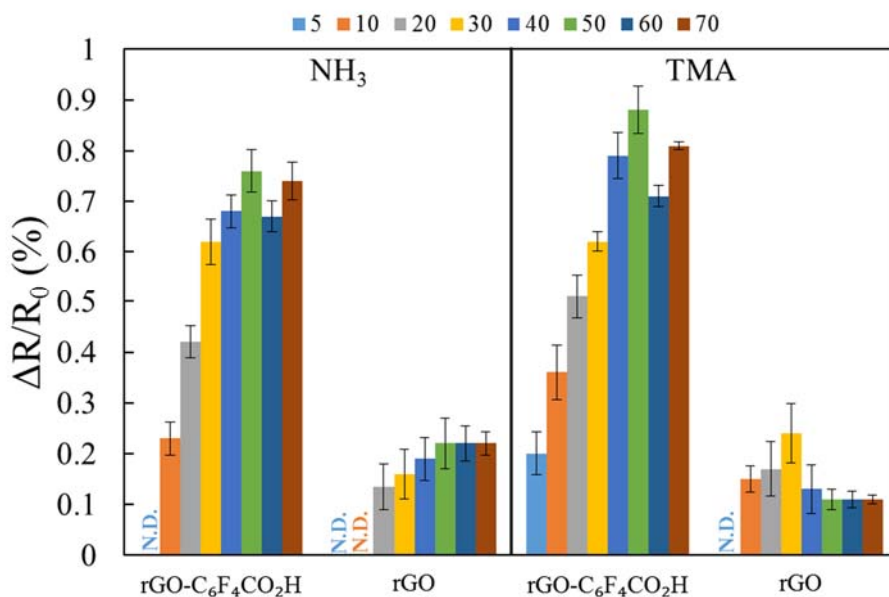
Figure 47: Responses of pristine and functionalized rGO to 100 s exposures of various concentrations (expressed in the legend in ppm) of TMA in N_2. N_2 was delivered on the sensors between each vapor exposure for 400 s. (N.D. Not Detectable)

rGO-N-$C_6F_4CO_2H$ turned out to be insensitive to 5 ppm of NH_3. However, as SWCNTs, the maximum saturation response of f-rGO was 50 ppm. Figure 48 shows the calibration curves of rGO-N-$C_6F_4CO_2H$ toward NH_3 and TMA, both linearly fitted.
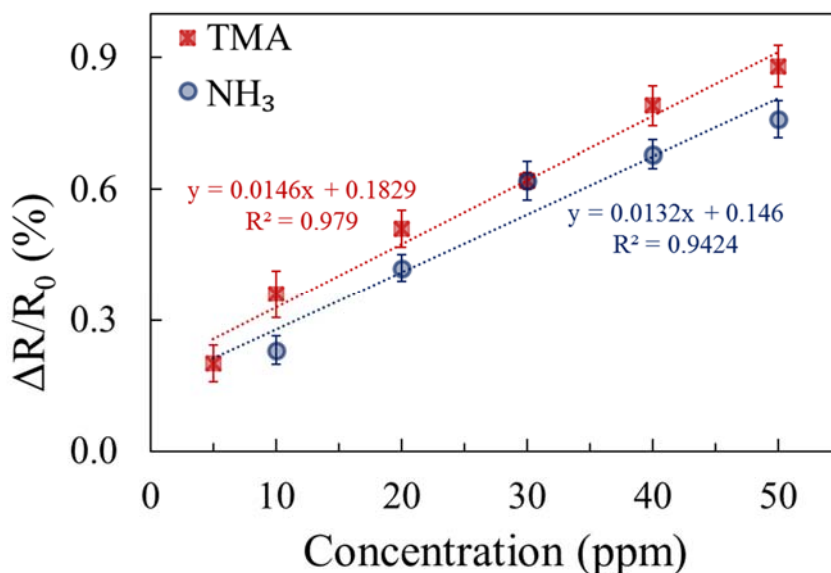
Figure 48: Response of rGO-N-$C_6F_4CO_2H$ at a single exposure of various concentrations of NH_3 and TMA in N_2. (Dotted line: linear fit).

Both f-CNTs and f-rGO based devices showed strong but irreversible responses, a behavior more similar to that of a dosimeter more than a sensor, namely devices able to assess the presence or the absence of hazardous vapors above a concentration threshold. Such responses can be useful for example in single-use wireless tags.

6.2.5. Wireless ammonia/trimethylamine gas detection

The electrical nature of the responses obtained allow for facile integration of sensitive materials into other platforms. For example, the detection of gaseous analytes can be performed by exploiting the Radio-Frequency IDentification (RFID) [94, 95] technology. In this case, pristine CNMs or modified CNMs can be inserted into the resonant circuit of a commercial RFID tag [96] and a network analyzer or a mobile phone [97] can be used as the reader.

Among all the synthesized materials, SWCNT-N-C$_6$F$_4$CO$_2$H showed the highest resistance variation upon exposure of gaseous analytes and was therefore tested with an RFID device.

6.2.6. RFID tag preparation and gas sensing measurements

The integration of the chemoresponsive material on commercial RFID tags (HF-I Tag-IT 13.56-MHz rf identification transponder square analysis (RI-I11-114A-01), Texas Instruments) was performed by disrupting the electronic circuits of the tags between the integrated circuit (IC) and the capacitor (C) with a hole punch. The electrical connection was then restored by drop-casting a sufficient amount of the suspension in order to obtain a film with an initial resistance of about 200 KΩ (Figure 49).

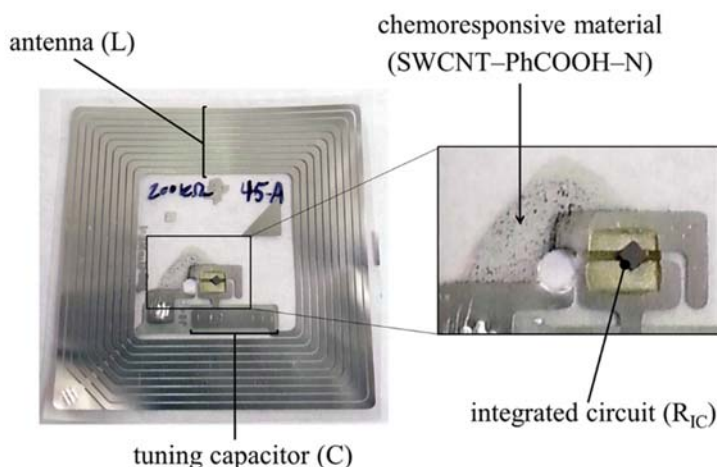Figure 49: A modified commercial RFID tag with the amine-sensitive SWCNT-N-C6F4CO$_2$H connecting the integrated circuit and the tuning capacitor after the interruption of the aluminum track.

The modified tag was enclosed in a homemade gas flow chamber and the gas exposures were carried out as described in section 6.2.2. The response of the device was investigated during four sequential exposures to 40 ppm of NH$_3$ or

TMA. The sensor material integrated into the RFID tag affects the power transferred between the reader and the tag and thereby indicates absence or presence of chemical stimuli. The RFID tag can be modeled as a RLC (resistance-inductance-capacitance) circuit with a half power bandwidth (BW) equal to 1/RC. BW and C were found using the same setup reported in [97] and the device response was defined as $\Delta R/R_0$. Data were used as obtained, without any fitting or baseline correction.

6.2.7. Results and discussion

The SWCNT-N-$C_6F_4CO_2H$ performance was tested with an RFID device for the detection of 40 ppm of NH_3 and TMA. This target concentration is ideal to detection when a fish has started the process of decomposition [3, 4]. Figure 50 shows the response profiles of two different tags exposed four times to 40 ppm of NH_3 and TMA. The exposures to 40 ppm of NH_3 and TMA rapidly increased the resistance of the device causing variations between 1.1% and 1.3% for NH_3 and TMA, respectively. According to literature [97] and to our experience, after a careful tuning of the initial resistance, such responses are appropriate to trigger changes in a wireless readout of the sensor performed, for example, with a smartphone.
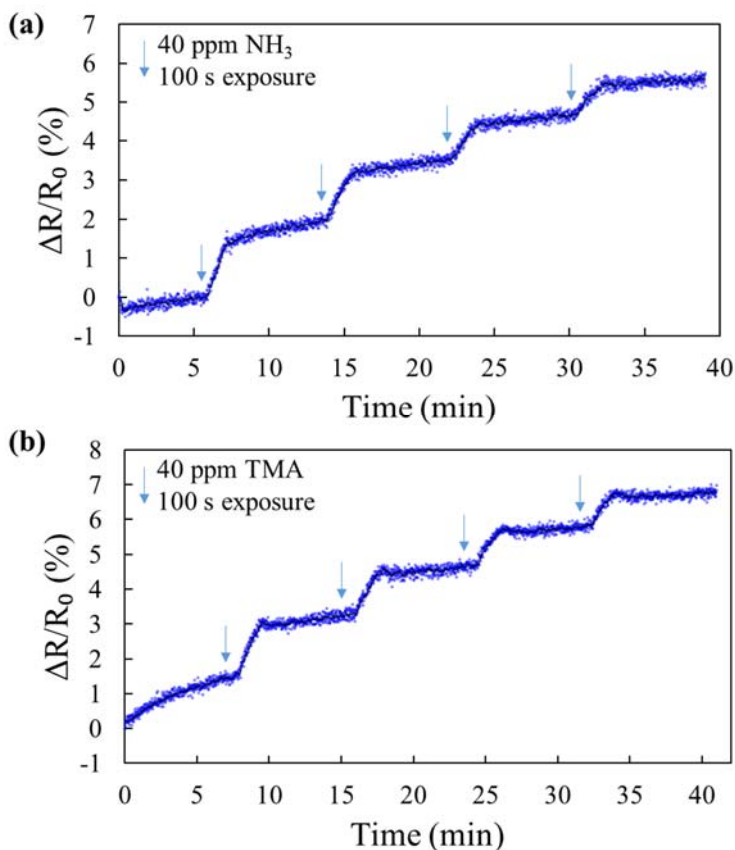
Figure 50: Resistance changes of (a) SWCNT-N-$C_6F_4CO_2H$ modified-tag exposed for 4 times to 40 ppm of NH_3 (100 s exposure, 400 s recovery with nitrogen at r.t.), (b) SWCNT-N-$C_6F_4CO_2H$ modified-tag exposed for 4 times to 40 ppm of TMA (100 s exposure, 400 s recovery with nitrogen at r.t.).

6.3. Gas sensing tests: Semi-static approach

Some materials were selected to be tested in a semi-static way using humid gases instead of anhydrous gases to simulate the real conditions of measurement. In fact, a possible use case scenario is represented by the insertion of the sensor into a package containing fish where a static atmosphere with high water content is expected. Sensors were fabricated by drop-casting the dispersions containing the sensitive materials onto custom made sensor platforms bearing two pairs of gold

electrodes (Figure 51), and the sensor resistance was measured by a multimeter (Keithley mod. 2700).

6.3.1. Fabrication of the sensitive films

SWCNTs-based samples: An amount of 2 mg of p- and f-SWCNTs was dispersed in 2 mL of distilled water. After sonication (~1-2 minutes), aliquots of 1-3 µL of the resulting dispersions were drop-cast onto the electrodes and dried under vacuum.

Porphyrins-based samples: SWCNT-H$_2$TPP, SWCNT-VOTPP and SWCNT-CuTPP were briefly sonicated (~30 seconds), then aliquots of 3 µL were-drop cast onto the electrodes to form films and dried under vacuum.
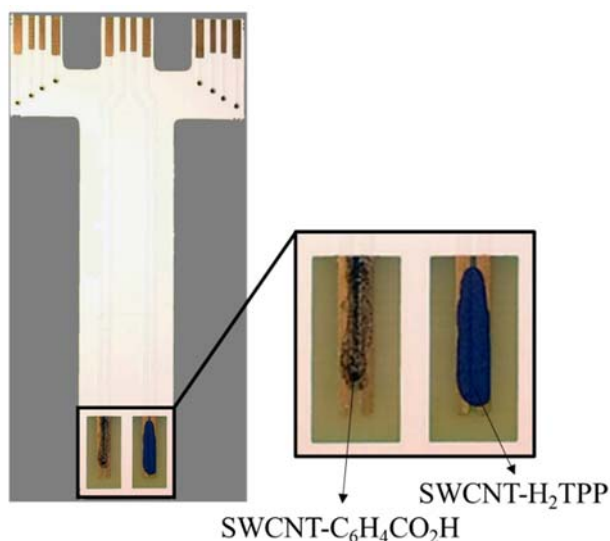

Figure 51: Illustrative SWCNTs- and porphyrins-based sensors.

Each device comprised two gold electrodes fabricated by standard photolithography on an FR4 substrate. The electrodes (1 mm width, 500 µm band gap) were connected to the reader by a USB connector. The device allowed the simultaneous measurement of two sensors.

6.3.2. Gas delivery system

Specific aliquots of aqueous ammonia, methylamine, dimethylamine or trimethylamine solutions (ammonium hydroxide solution, 28-30% NH_3 in H_2O, Sigma-Aldrich; methylamine solution 40 wt. % in H_2O, Sigma-Aldrich; dimethylamine solution 40 wt. % in H_2O, Sigma-Aldrich; trimethylamine solution ~45 wt. % in H_2O, Sigma-Aldrich) were introduced in a home-made test chamber (net volume 100 cm^3) at atmospheric pressure and controlled temperature (25 °C). The limited volume allowed the complete evaporation of the solution and the generation of different concentrations of analyte. After the exposure to the target analyte, the sensor recovery of the baseline was measured while cleaning the test chamber with vacuum (Figure 52). Vacuum cleaning of the sensor chamber allowed to perform multiple measurements in a reasonable period of time, and it shortened the recovery of the sensor baseline conditions with respect to leaving the sensor in air at room temperature.
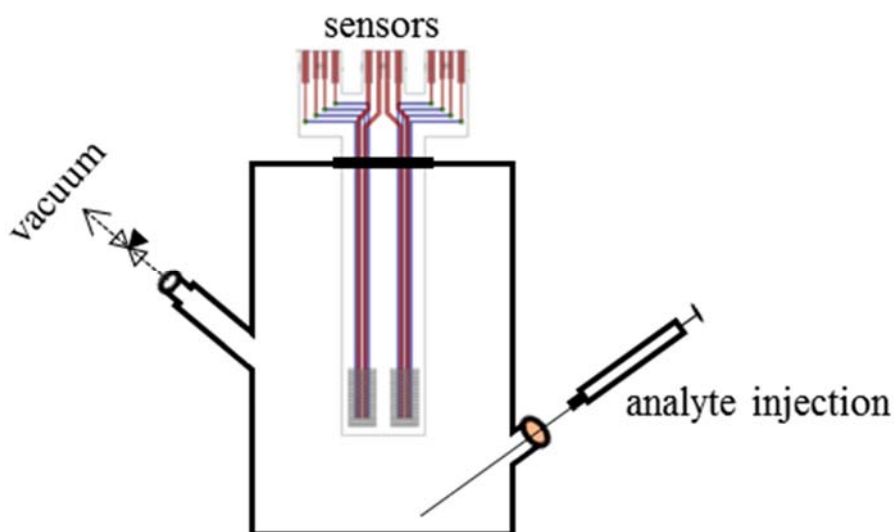

Figure 52: Schematic representation of the home-made test chamber. The system was kept at constant temperature with a thermostatic bath (Haake GH, Fisons) not depicted in figure for simplicity.

After cleaning the chamber, the atmospheric pressure was retrieved by refilling the chamber with purified air for 90 seconds.

In addition to volatile amines, other volatile analytes were tested such as acetone ($\geq$99.9%, Sigma-Aldrich), diethyl ether ($\geq$ 99.0%, Sigma-Aldrich), ethanol ($\geq$99.8%, Sigma-Aldrich), 2-propanol (99.5%, Sigma-Aldrich), methanol (99.8%, Sigma-Aldrich), water (LC-MS CHROMASOLV, Sigma-Aldrich), hexane (95%, Sigma-Aldrich), acetonitrile (99.8%, Sigma-Aldrich), toluene (99.8%, Sigma-Aldrich), chloroform ($\geq$99% with amylenes as stabilizer, Sigma-Aldrich) and ethyl acetate (99.8%, Sigma-Aldrich).

6.3.3. Sensor response

The electrical resistance of the sensors was measured by using a Keithley 2700 Multimeter/ Data Acquisition System. The sensor response was given as $\Delta R/R_0$, where R_0 is the resistance before exposure to the volatile analyte and R is the maximum resistance achieved during exposure. For each sensing material, the average responses of two replicate sensors is reported. Data were used as obtained, without any fitting or baseline correction. Error bars represent the standard deviation.

6.3.4. Results and discussion

SWCNTs-based samples: p-SWCNTs, SWCNT-$C_6F_4CO_2H$, SWCNT-$C_6H_4CO_2H$, SWCNT-H_2TPP, SWCNT-VOTPP and SWCNT-CuTPP were tested with the method described above.

Although the low DF, SWCNT-$C_6F_4CO_2H$ was tested to confirm the irreversible behavior of the perfluorinated compound as already proved in the paragraph 6.2.4. Figure 53 gives an idea about the irreversible response of the compound.
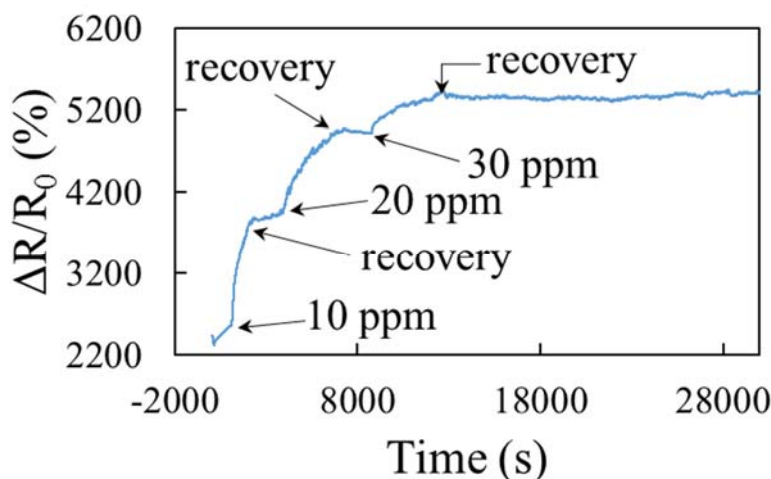
Figure 53: Example of irreversible response of SWCNT-$C_6F_4CO_2H$ sample exposed to different concentrations of TMA. Recovery was performed by empting the test chamber with a vacuum pump (10^{-1} Torr).

The presence of four fluorine atoms in the aromatic ring of the functionalizing molecule, in addition to the carboxylic group, made the interaction between sensor and amines too strong, hindering the reversibility of the response. Baseline conditions of sensors can be recovered by ultraviolet (UV) light [23] or intense heating [100], but these treatments would alter the chemical characteristic of the compound and affect the sensor performance and lifetime. For this reason we decided not to use these approaches to recover the baseline resistance.

Unlike SWCNT-$C_6F_4CO_2H$, SWCNT-$C_6H_4CO_2H$ gave a reversible response. Figure 54 shows the response of p-SWCNTs and SWCNT-$C_6H_4CO_2H$ at different concentrations of TMA.
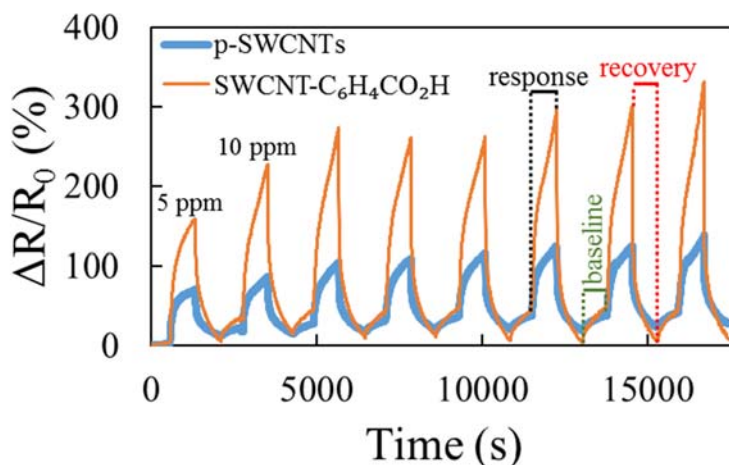
Figure 54: Response profile of p-SWCNTs and SWCNT-$C_6H_4CO_2H$ exposed to different concentrations (5, 10, 20, 30, 40, 50, 60, 70 ppm) of TMA. (15 minutes exposure to gas analyte (response), 15 minutes vacuum for the recovery of the sensor (recovery), 13 minutes baseline collection, including 90 seconds to restore the pressure (baseline).

All sensors described in this paragraph showed the same response profile, so Figure 54 can be taken as representative example of sensing trace with graphically visualized key terms (response, baseline, recivery) referring to the response profile of SWCNT-$C_6H_4CO_2H$.

As can be noted from the graph, SWCNT-$C_6H_4CO_2H$ sensor was not able to distinguish TMA concentrations ranging between 30 and 40 ppm due to a saturation of the response. The test with NH_3 showed a similar response, but response saturation was achieved at a concentration of 50 ppm. The improvement of the response in sensors fabricated with functionalized CNTs respect to the pristine material was noticeable; p-SWCNTs showed a reversible behavior in the test performed in semi-static conditions, however their sensitivity was low.

The response of the sensor fabricated with non-functionalized rGO to both ammonia and trimethylamine was unstable and very noisy, whereas rGO-$C_6H_4CO_2H$ produced net signals even if quantitation of NH_3 and TMA was

unsatisfactory as the sensor saturated just at 10 ppm for TMA and 20 ppm for NH$_3$.

Porphyrins-based samples: p-SWCNTs functionalized with porphyrins turned out to be promising materials. Figure 55 shows typical responses for SWCNT-H$_2$TPP (Figure 55a) and SWCNT-CuTPP (Figure 55b) at different concentrations of TMA.
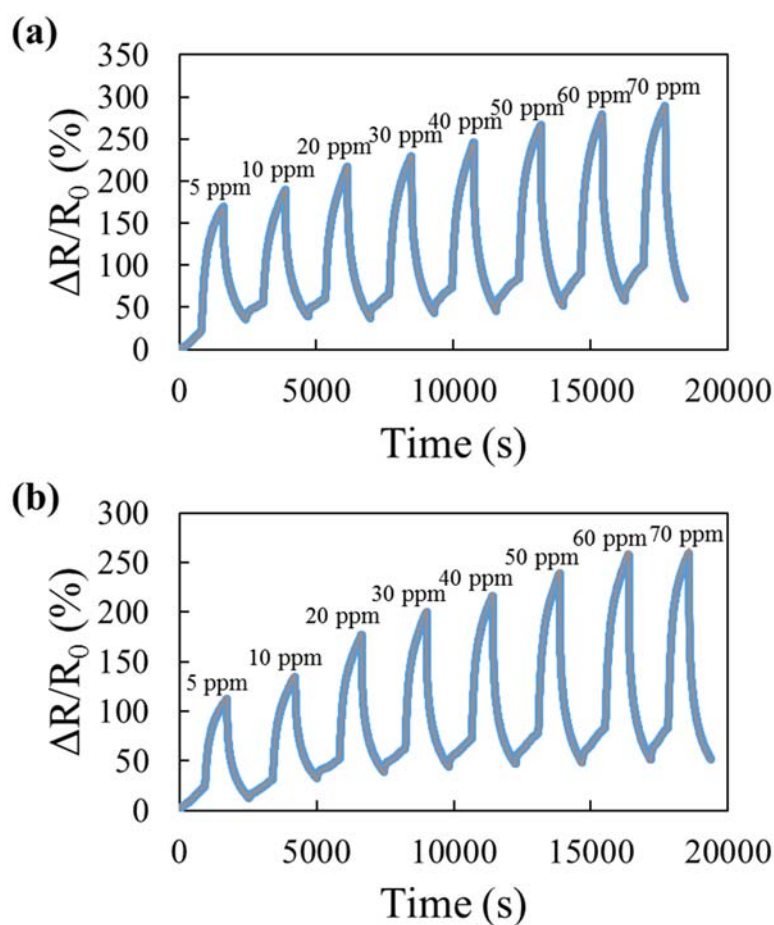
Figure 55: Response profiles of two replicate sensors of (a) SWCNT-H$_2$TPP and (b) SWCNT-CuTPP to increasing concentrations of TMA. (blue line: sensor 1, orange line: sensor 2). Experimental conditions: 15 minutes exposure to gas analyte (response), 15 minutes vacuum for the recovery of the sensor (recovery),

13 minutes baseline collection, including 90 seconds to restore the pressure (baseline).

Unfortunately, SWCNT-VOTPP did not show the same response profile of SWCNT-H_2TPP or SWCNT-CuTPP. Figure 56 shows the electrical response of SWCNT-VOTPP in two different tests carried out to evaluate the performance of sensors fabricated with this material.

Figure 56: Electrical response of SWCNT-VOTPP upon the delivery of different concentrations of TMA. Experimental conditions for (a): 30 minutes exposure to gas analyte, for 20 and 70 ppm sensor exposed overnight, 20 minutes vacuum, 20 minutes baseline collection, including 90 seconds to restore the pressure; (b) 15

minutes exposure to gas analyte, 15 minutes vacuum for the recovery of the sensor, 13 minutes baseline collection, including 90 seconds for restoring the pressure).

Clearly SWCNT-VOTPP did not work well, as it changed its resistance upon the exposure to the analyte but the response did not have a monotone relationship with the concentration. The vanadyl complex was chosen because literature is rich of examples of sensors based on vanadium (IV) or (V) for the detection of low concentrations of gas molecules like ethanol or ammonia [101]. Even though the vanadyl-based sensor failed for the analyte concentrations examined in this work, it is not excluded that this sensor may be suitable for the determination of very low concentrations of ammonia or trimethylamine.

Conversely, SWCNT-CuTPP showed a completely different behavior. Figure 57 shows the result of a test performed in almost the same conditions of the test showed in Figure 56a. The sensor was left to respond until saturation for each concentration examined. Moreover, at 20 and 70 ppm, the sensor was left to respond over one night. The stability of the sensor response even for very long times is noticeable.
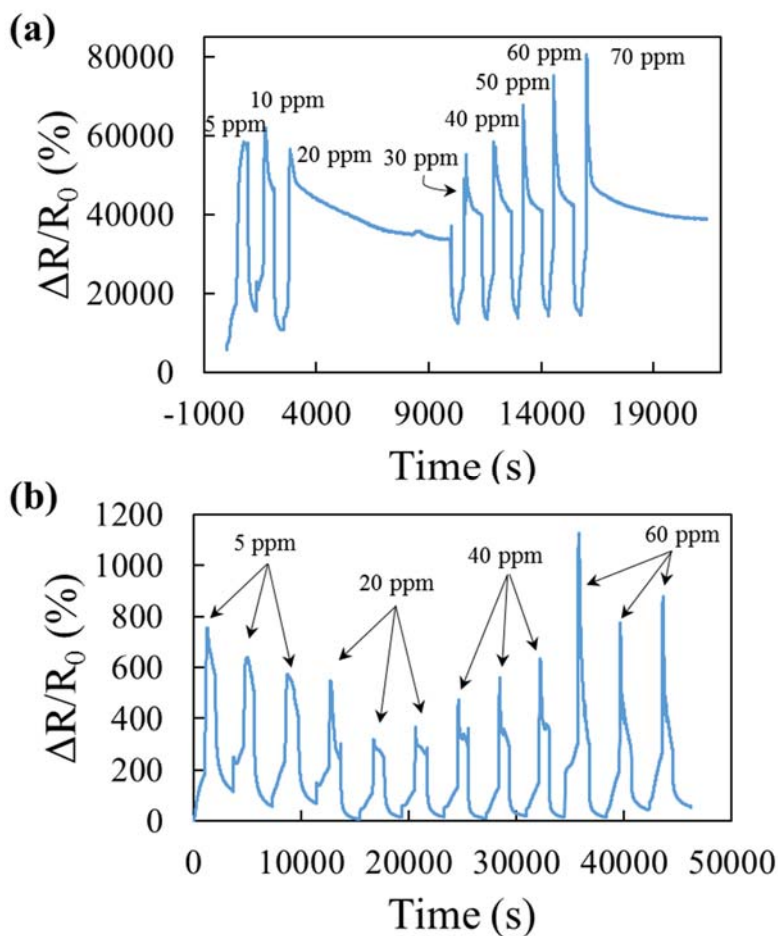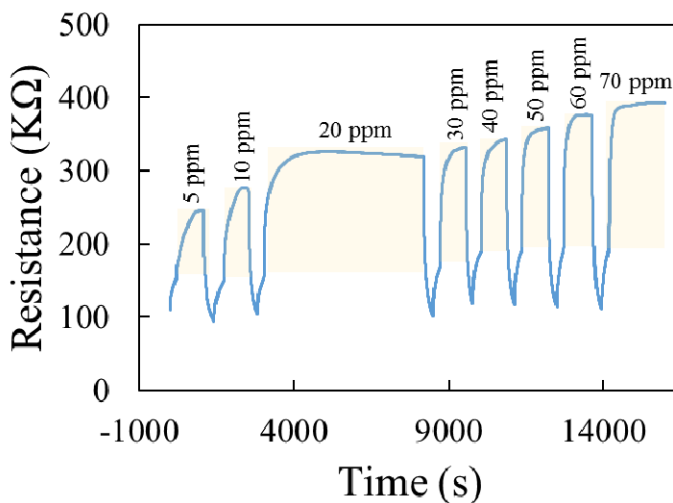
Figure 57: Electrical response of SWCNT-CuTPP upon the delivery of different concentrations of TMA. Experimental conditions: exposure to gas analyte until saturation, at 20 and 70 ppm sensor exposed overnight, 20 minutes vacuum after each exposure, 20 minutes baseline collection, including 90 seconds to restore the pressure before each exposure.

Hereafter, all sensor responses showed in the text were obtained using the test procedure described in the caption of Figure 54 and repeated here for simplicity for the reader: 15 minutes exposure to gas analyte (response), 15 minutes vacuum for the recovery of the sensor (recovery), 13 minutes baseline collection, including 90 seconds to restore the pressure (baseline). This allows an easy comparison of sensor performances. Figure 58a and Figure 58b show the calibration curves of p-SWCNTs, SWCNT-H$_2$TPP and SWCNT-CuTPP for TMA and NH$_3$, respectively.
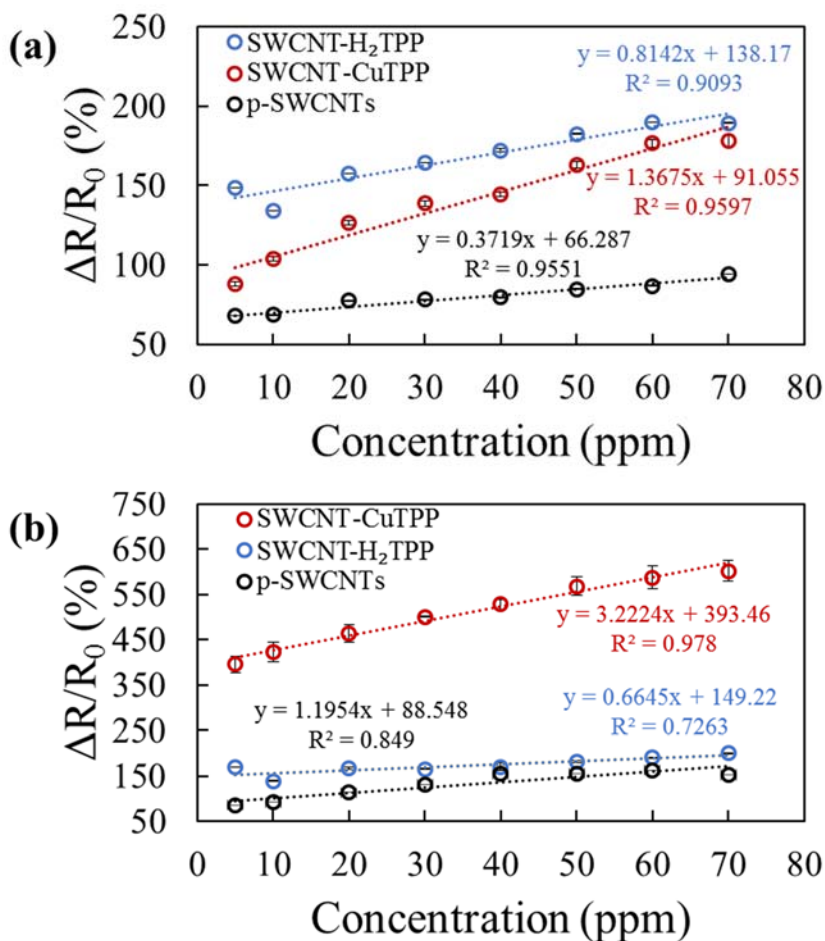
Figure 58: Calibration curves of p-SWCNTs, SWCNT-H$_2$TPP and SWCNT-CuTPP exposed to different concentrations of (a) TMA and (b) NH$_3$. Experimental conditions: 15 minutes exposure to gas analyte (response), 15 minutes vacuum for the recovery of the sensor (recovery), 13 minutes baseline collection, including 90 seconds to restore the pressure (baseline). (Dotted line: linear fit)

The plot shows the remarkable effect of the functionalization of SWCNTs with CuTPP or H$_2$TPP on the sensor response, a marked increase in sensitivity toward ammonia and trimethylamine respect to pristine SWCNTs (p-SWCNTs) occurs. However, so far, the functionalization improved the sensitivity but not the selectivity, as NH$_3$ and TMA produced rather comparable resistance changes both for SWCNT-CuTPP and SWCNT-H$_2$TPP. Looking closely at the graph of Figure

58, it can be noted that SWCNT-H_2TPP experienced an anomalous behavior when exposed to 5 ppm of NH_3 or TMA. The SWCNT-H_2TPP sensor response at 5 ppm was higher than the successive larger tested concentrations for both NH_3 and TMA. However, if subjected to more cycles, SWCNT-H_2TPP response at 5 ppm stabilized (Figure 59). SWCNT-H_2TPP response toward the basic volatile compounds can be caused by the interaction of the basic analytes with the two relatively acid protons of the core of the free base porphyrin ring.

Contrary to SWCNT-H_2TPP, SWCNT-CuTPP showed a linear increasing trend. The high affinity of copper with NH_3 it is well known. SWCNT-CuTPP was therefore tested further with NH_3, and Figure 60 is an example of the stability and reproducibility of the metallated porphyrin-based sensor.
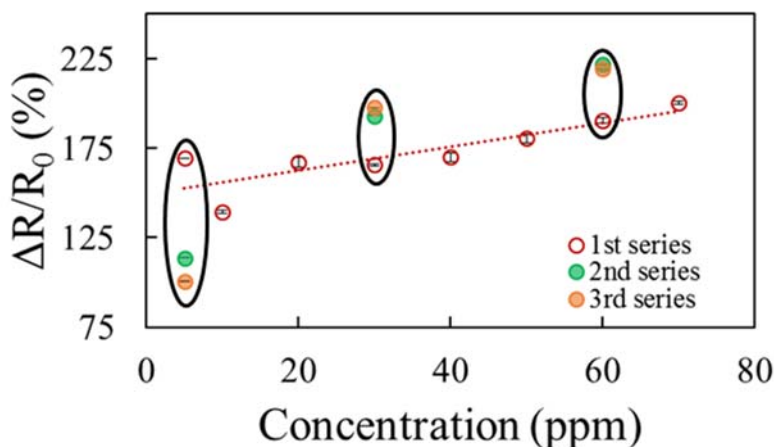
Figure 59: After a first series of measurement (red), the sensor SWCNT-H_2TPP was tested a second time (green) and a third time (orange) at 5, 30 and 60 ppm and showed a marked change in sensitivity. Black ellipses are only intended to help the reader to visualize replicate measurements performed at the same concentration level. Target analyte: NH_3.
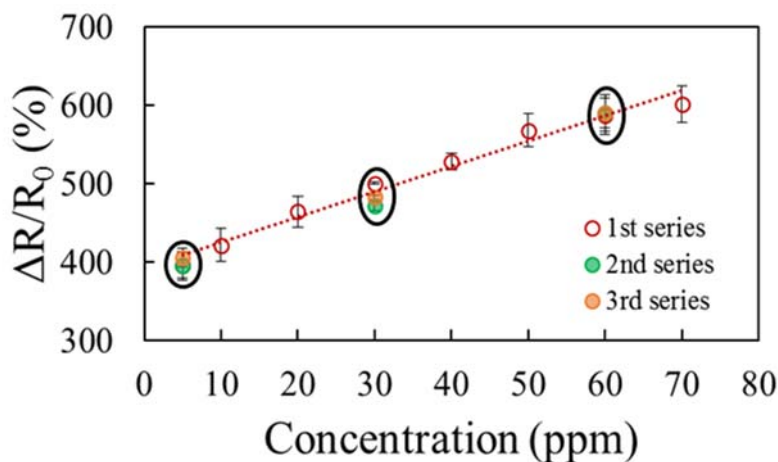
Figure 60: SWCNT-CuTPP sensor response in a first series of measurement ranging between 5 and 70 ppm (red), and two other successive series at 5, 30 and 60 ppm in green and orange, respectively. Black ellipses are only intended to help the reader to visualize replicate measurements performed at the same concentration level. Gas analyte: NH_3.

Reproducibility was also tested for TMA and compared to that of NH_3 as described in Figure 61. Figure 61 shows the average response of two replicate SWCNT-CuTPP sensors exposed for three consecutive times to 5, 20, 40 and 60 ppm of TMA and NH_3.
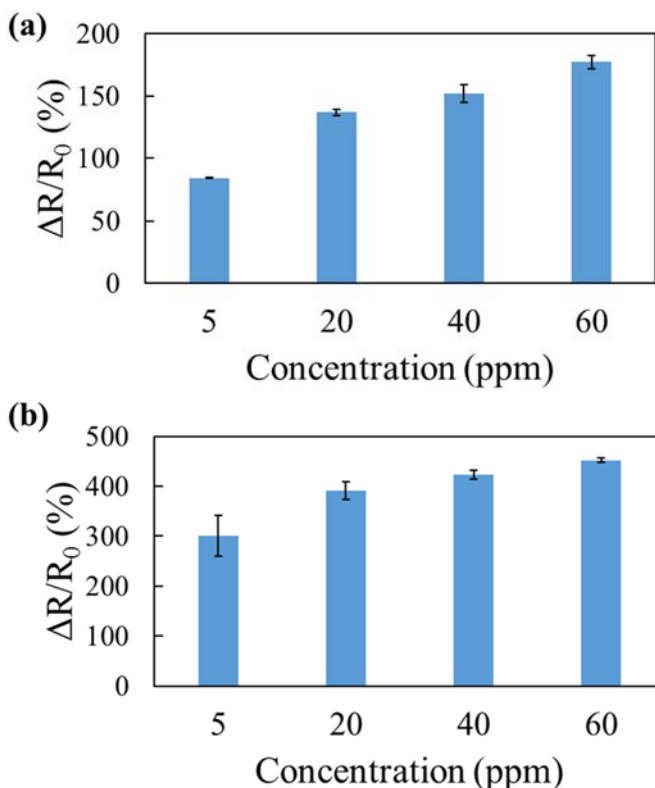
Figure 61: Example of the responses of SWCNT-CuTPP to three 15 minutes exposures of various concentrations of (a) TMA and (b) NH_3.

Figure 62 compares all results obtained by tests performed in semi-static conditions. At a first sight, it can be noted the high sensitivity and limited selectivity of SWCNT-CuTPP toward NH_3 and TMA.
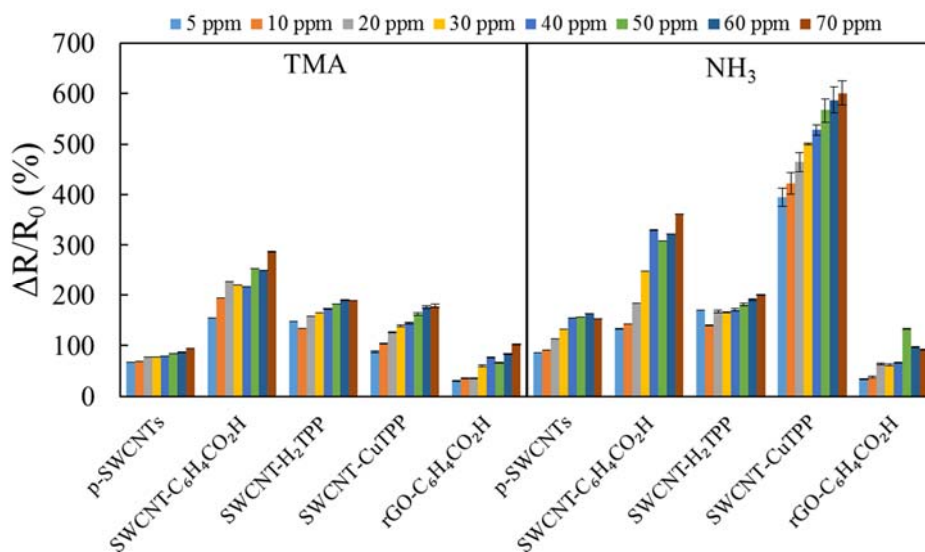
Figure 62: General comparison of results obtained for p-SWCNTs, SWCNT-$C_6H_4CO_2H$, SWCNT-H_2TPP and SWCNT-CuTPP tested with the following experimental conditions: 15 minutes exposure to gas analyte (response), 15 minutes vacuum for the recovery of the sensor (recovery), 13 minutes baseline collection, including 90 seconds to restore the pressure (baseline).

Looking closely at the graph, it is possible to observe the different behavior of the synthesized materials toward the detection of TMA and NH_3. SWCNT-$C_6H_4CO_2H$ showed a reliable response only up to 20 ppm for TMA and 40 ppm for NH_3, whereas SWCNT-CuTPP showed a linear trend until 70 ppm.

Water is usually the main interfering compound when measuring gaseous samples, and in our specific use case scenario, i.e. the sensor enclosed in a sealed package containing fish, the sensor is going to be exposed to 100% relative humidity (RH). For this reason, sensor response to water and to target analytes in the presence of high humidity levels was investigated.

Figure 63 shows the results of a test performed injecting alternately in the test chamber 3 µL of distilled water, 3 µL of TMA solution and 3 µL of NH_3 solution. Each test was carried out using freshly made sensors. Figure 63 shows that sensors based on porphyrins are less sensitive to water than sensors based on covalently functionalized SWCNTs and rGO.
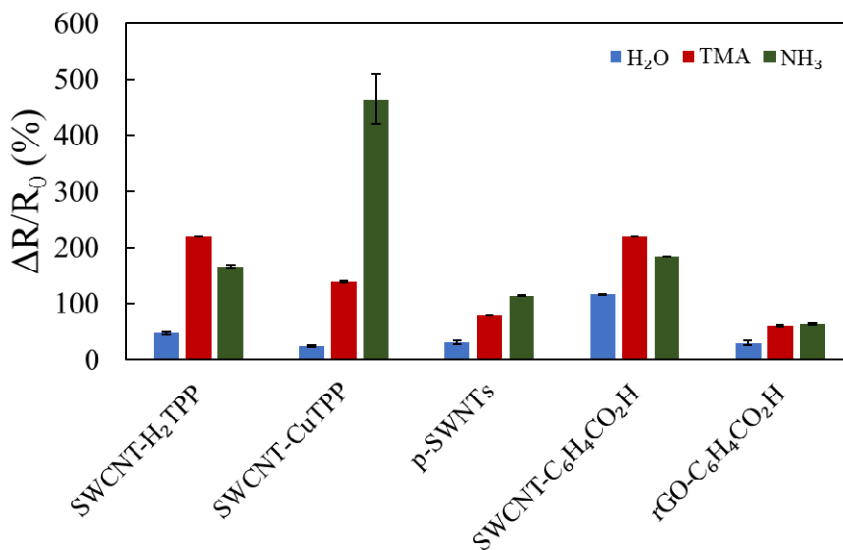
Figure 63: Responses of p-SWCNTs, SWCNT-$C_6H_4CO_2H$, rGO-$C_6H_4CO_2H$, SWCNT-H_2TPP and SWCNT-CuTPP to 3 µL of distilled water, 3µL of TMA solution and 3 µL of NH_3 solution.

SWCNT-H_2TPP- and SWCNT-CuTPP-based sensor response to volatile organic compounds and water was compared to the response of different volatile amines (trimethylamine, dimethylamine, methylamine and ammonia). A fresh device was used for each analyte and the concentrations investigated were 5, 20 and 40 ppm. Response of acetone, diethyl ether, ethanol, 2-propanol, methanol, hexane, acetonitrile, toluene, chloroform and ethyl acetate refer to measurements carried out in conditions of 100% RH. The other measurements, namely water, trimethylamine, methylamine, dimethylamine and ammonia, since they are already aqueous analytes, were performed without altering the environment of the test chamber. This decision was made to be consistent with the other results showed in the text about ammonia and trimethylamine. However, a qualitative study to evaluate the effect of moisture on the system was performed. Concentrations of 5 and 40 ppm of trimethylamine, methylamine, dimethylamine and ammonia were delivered on SWCNT-CuTPP and SWCNT-H_2TPP sensors both in dry and in humid conditions and we noted that the presence of moisture

did not negatively affect the response of the sensors. The only observed effect of moisture on the system was a slight increase of the baseline drift. Experimental results are showed in Figure 64.
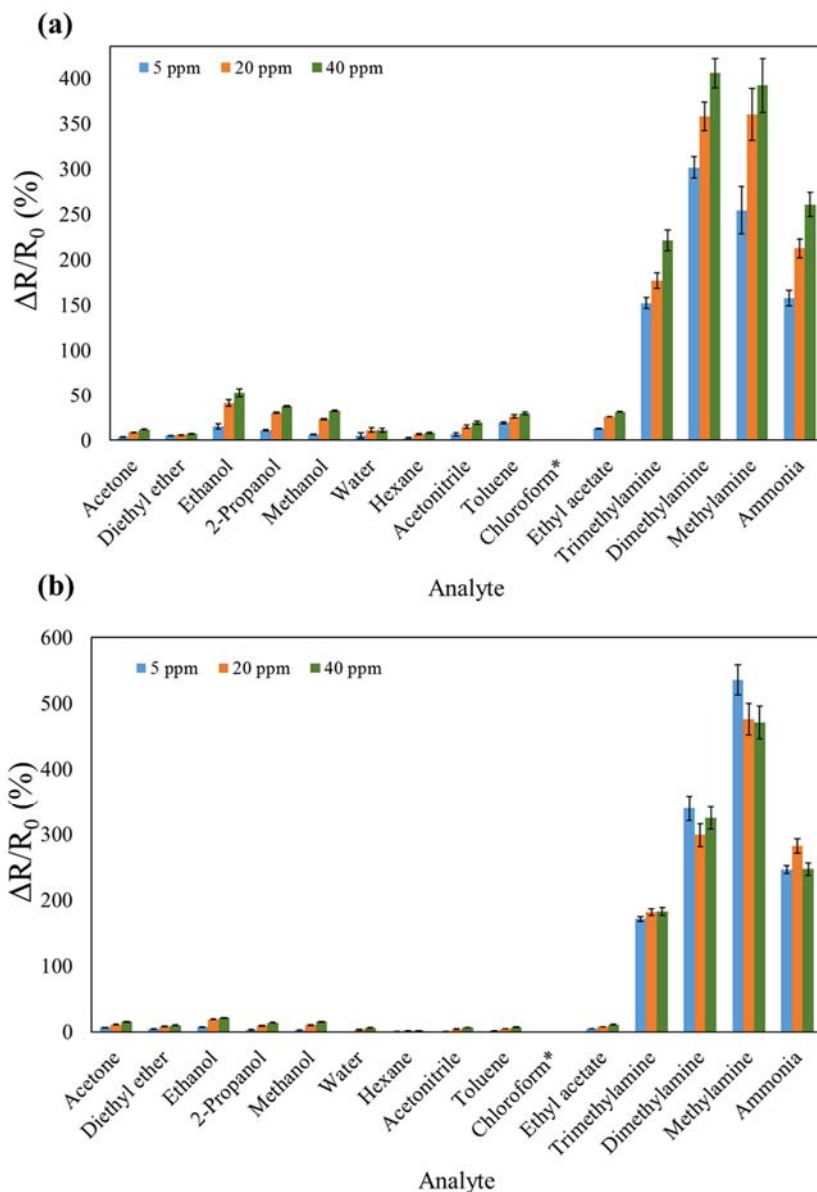
Figure 64: Responses of (a) SWCNT-CuTPP and (b) SWCNT-H₂TPP based sensors to 15 minutes exposures of various compounds' vapors at 100% RH. *the numerical response ($\Delta R/R_0$ (%)) of chloroform, not visible in the graph, was: n.d. (not detectable) for 5 ppm, -0.6 and -0.5 for 20 ppm and 40 ppm, respectively, for

SWCNT-CuTPP and -1.4 (5 ppm), -0.2 (20 ppm) and -0.1 (40 ppm) for SWCNT-H_2TPP. For water, trimethylamine, dimethylamine, methylamine and ammonia, the results reported were registered without altering the environment of the chamber test.

This plot shows that the sensor response to amines is far higher than response to the other volatile organic compounds. The functionalization selectively improved sensor sensitivity to the amines (at least, three-fold less than the amines response) but selectivity between different kind of amines remains an issue. However, from an application view point, the ageing of fish gives rise to a large number of volatile compounds and it is the whole process that needs to be monitored more than the emission of a single volatile chemical. For this reason, SWCNT-CuTPP-based sensor represents a credible candidate for the realization of the final device.

Finally, Figure 65 shows a schematic representation of the possible interactions of the volatile basic molecules with the functionalized and pristine carbon nanomaterials. Interactions are mostly due to Brønsted and Lewis acid/base interactions between the lone pair of the volatile analytes and the acid moiety and electron deficiencies of the carbon nanomaterials.

Figure 65: Schematic representation of the possible interactions between CNMs and volatile basic amines. For simplicity are herein reported only SWCNTs as

CNM and NH_3 as volatile basic compound. (a) SWCNTs covalently functionalized, (b) SWCNTs non-covalently functionalized. The symbol ⊕ depicts holes, namely electric charge carriers with a positive charge, present as majority carriers in the p-type semi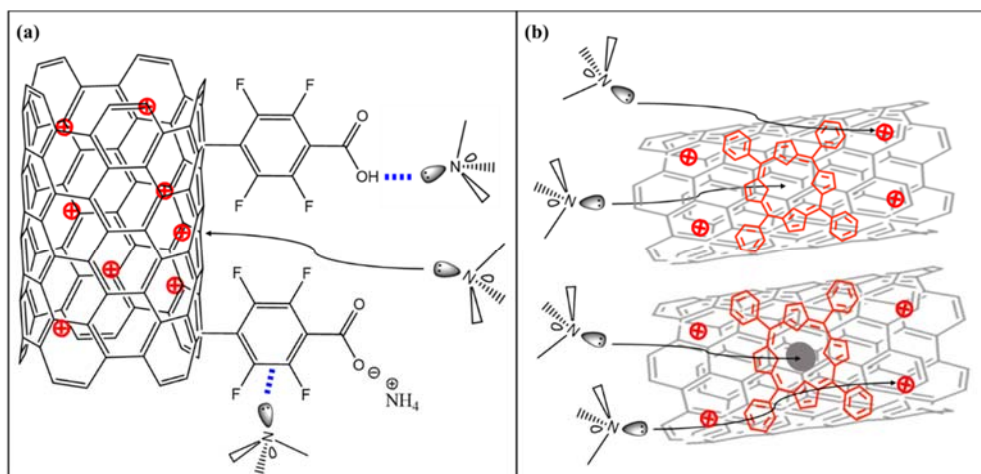conductor carbon nanotubes. The figure depicts the mechanism of gas sensing operating on p-type SWCNTs semiconductors with reducing type gases (NH_3).

6.4. Conclusions

In this chapter the gas sensing experimental results obtained with covalently and non-covalently functionalized SWCNTs and covalently functionalized MWCNTs and rGO were described. Both functionalizations led to more performing materials than the corresponding pristine. SWCNT-N-$C_6F_4CO_2H$, SWCNT-$C_6H_4CO_2H$ and rGO-$C_6H_4CO_2H$ were the best responsive materials obtained by covalent functionalization, whereas SWCNT-CuTPP was the best chemiresponsive material obtained by non-covalent functionalization. SWCNT-N-$C_6F_4CO_2H$ and rGO-$C_6H_4CO_2H$ were able to detect up to 40 ppm and 50 ppm of TMA and NH_3, respectively, by the dynamic tests. SWCNT-$C_6H_4CO_2H$ and rGO-$C_6H_4CO_2H$ examined by the semi-static test, turned out to be less sensitive toward TMA and NH_3 detection. In particular, SWCNT-$C_6H_4CO_2H$ detected up to 20 and 40 ppm of TMA and NH_3, respectively, whereas rGO-$C_6H_4CO_2H$ was able to detect only up to 10 ppm for TMA and 20 ppm for NH_3. On the other hand, SWCNT-CuTPP resulted to be sensitive to TMA up to 60 ppm and to NH_3 up to 40 ppm. Remarkably, the sensitivity to potentially interfering compounds was really low. Moreover, the test carried out with the wireless device paved the way for a future development of cost-effective onsite chemical RFID sensors for the detection of gas molecules. For example, the RFID approach could be used to provide a yes/no response, to determine if the fish is considered edible/inedible. Obviously, further studies are needed to evaluate the robustness of the sensor when exposed to different conditions of temperature and humidity. For a more versatile device, the

output range of the sensor should be improved as well as the capability of discrimination between different volatile amines.

Conclusions

This study suggests that the functionalization of pristine carbon nanomaterials improves the sensitivity of the sensors toward the detection of volatile amines and that the covalent functionalization allows to have materials with tunable characteristics. The main drawback of the covalent functionalization is the damage of the extended electronic states, which causes an increase in the baseline resistance of the material and consequently a possible loss of sensitivity for the detection of target analytes. However, a low degree of functionalization can at the same time preserve the integrity of the carbon nanomaterial electronic backbone and allow good sensing capabilities. A covalent functionalization creates more durable, reproducible and stable materials, whereas non-covalent functionalization is easier to perform and allows the maintenance of the π-conjugation of the carbon nanomaterial. The main disadvantage of this kind of non-covalent functionalization is the poor stability of the resulting materials, in part because these materials are physical mixtures. However, the use of large amounts of functionalizing molecule with respect to the carbon nanomaterial can avoid this problem. In this thesis, carbon nanomaterials covalently functionalized with perfluorinated molecules gave an irreversible response when exposed to different concentrations of NH_3 and TMA both in dynamic and semi-static measurement conditions. An irreversible response is not necessarily a drawback because such kind of sensors can be exploited to assess the presence or the absence of hazardous vapors above a given concentration threshold. The SWCNT-N-$C_6F_4CO_2H$-based sensor is an example of such single-use device that was capable to detect a concentration of NH_3 and TMA emitted up to 40 ppm. Even though the device was not able to clearly distinguish between the two analytes, considering TMA and NH_3 the prominent components emitted with the spoiling of fish, this system is ready to enable the development of cost-effective single-use onsite chemical sensors for the detection of gas molecules.

Opposite behavior was shown by sensors obtained by non-covalent functionalization. SWCNT-CuTPP, for its simple preparation, good selectivity

(respect to other non-amines substances) and good sensitivity, revealed to be a very promising material for the future development of the sensor. Its reversible behavior allowed to distinguish a wide range of concentrations (5-70 ppm) both for TMA and NH_3 without saturating the system.

Obviously, additional efforts have to be made to optimize the sensor performance, namely to improve the sensitivity of the sensitive material testing also lower gas analyte concentrations and performing tests also at lower temperatures. Then, an optimized method for the realization of the wireless device will have to be developed.

References

[1] Sotelo, C. G. (1995). Trimethylamine oxide and derived compounds' changes during frozen storage of hake (Merluccius merluccius). Food chemistry, 53(1), pp. 61–65.

[2] Özoğul, F. (2000). Comparision of methods used for determination of total volatile basic nitrogen (TVB-N) in Rainbow trout (Oncorhynchus mykiss). Turkish Journal of Zoology, 24(1), pp. 113–120.

[3] Chen, E. X. (2014). Highly Selective and Sensitive Trimethylamine Gas Sensor Based on Cobalt Imidazolate Framework Material. ACS applied materials & interfaces, 6(24), pp. 22871–22875.

[4] Mitsubayashi, K. (2004). Trimethylamine biosensor with flavin-containing monooxygenase type 3 (FMO3) for fish-freshness analysis. Sensors and Actuators B: Chemical, 103(1), pp. 463–467.

[5] Silverman, R. A. (1989). Effects of occlusive and semiocclusive dressings on the return of barrier function to transepidermal water loss in standardized human wounds. Journal of the American Academy of Dermatology, 20(5), pp. 755–760.

[6] Glibbery, A. B. (1992). pH in leg ulcers. Int J Microcirc Clin Exp, 2(109), 98.

[7] Melai, B. (2016). A graphene oxide pH sensor for wound monitoring. 38th Annual International Conference of the IEEE Engineering in Medicine and Biology Society (EMBC), Orlando, FL, USA, 16-20 August 2016, pp. 1898–1901.

[8] Calisi, N. (2015). Thermosensitive materials for disposable wearable sensors, Ph.D. thesis.

[9] The Compression Therapy Study Group. Compression, consensus document based on scientific evidence and clinical experiences. Torino: Minerva Medica Editions, 2009, pp. 8–18.

[10] Adam, H. (1991). Chemical sensors definitions and classification. Pure Appl. Chem, 63, 1274–1250.

[11]   Egashira, M. (1990). Trimethylamine sensor based on semiconductive metal oxides for detection of fish freshness, Sensors and Actuators B: Chemical., 1, pp. 108–112.

[12]   Marquis, B.T. (2001). A semiconducting metal oxide sensor array for the detection of NOx and NH_3. Sensors and Actuators B: Chemical, 77 pp. 100–110.

[13]   Sun, C. (2016). Selective detection of part per billion concentrations of ammonia using a p–n semiconducting oxide heterostructure. Sensors and Actuators B: Chemical, 226, pp. 156–169.

[14]   Lee, S.K. (2014). Gas sensors based on carbon nanoflake/tin oxide composites for ammonia detection. Journal of Hazardous Materials, 268, pp. 110–114.

[15]   Cui, S. (2013). Controllable synthesis of silver nanoparticle-decorated reduced graphene oxide hybrids for ammonia detection. Analyst, 138, pp. 2877–2882.

[16]   Sánchez, M. (2011). Ammonia sensors based on composites of carbon nanotubes and titanium dioxide, in: M. Naraghi (Ed.), Carbon Nanotubes – Growth and Applications, INTECH Open Access Publisher, pp. 457–470.

[17]   Su, H.C. (2014). Tin dioxide functionalized single–walled carbon nanotube (SnO2/SWCNT)-based ammonia gas sensors and their sensing mechanism. Journal of The Electrochemical Society, 161, pp. B283–B290.

[18]   Jayatissa, A.H. (2008). Multiwalled carbon nanotube-based hydrogen gas sensors, in Electro/Information Technology, IEEE International Conference, pp. 372–376.

[19]   Ndiayea, A.L. (2012). Elaboration of single wall carbon nanotubes-based gas sensors: Evaluating the bundling effect on the sensor performance. Thin Solid Films, 520, pp. 4465–4469.

[20]   Wang, L.C. (2011). A single-walled carbon nanotube network gas sensing device, Sensors, 11, pp. 7763–7772.

[21]   Calisi, N. (2013). Factors affecting the dispersion of MWCNTs in electrically conducting SEBS nanocomposites. European Polymer Journal, 49, pp. 1471–1478.

[22]   Abdulla, S. (2015). Highly sensitive, room temperature gas sensor based on polyaniline-multiwalled carbon nanotubes (PANI/MWCNTs) nanocomposite for trace-level ammonia detection. Sensors and Actuators B: Chemical., 221, pp. 1523–1534.

[23]   Pistone, A. (2013). Fe_3O_4–MWCNT–PhCOOH composites for ammonia resistive sensors. Sensors and Actuators B: Chemical, 186, pp. 333–342.

[24]   Iijima, S. (1991). Helical microtubules of graphitic carbon. Nature, 354(6348), pp. 56–58.

[25]   S. Senadheera, Electro-mechanical properties of Carbon Nanotubes.

[26]   Balasubramanian, K. (2005). Chemically functionalized carbon nanotubes. Small, 1(2), pp. 180–192.

[27]   Wepasnick, K.A. (2010). Chemical and structural characterization of carbon nanotube surfaces. Analytical and bioanalytical chemistry, 396(3), pp. 1003–1014.

[28]   Herrero, M.A. (2008). Recent advances in the covalent functionalization of carbon nanotubes. Molecular Crystals and Liquid Crystals, 483(1), pp. 21–32.

[29]   Chico, L. (1996). Pure carbon nanoscale devices: nanotube heterojunctions. Physical Review Letters, 76(6), p. 971.

[30]   Bandaru, P. R. (2007). Electrical properties and applications of carbon nanotube structures. Journal of nanoscience and nanotechnology, 7(4-5), pp. 1239–1267.

[31]   Banerjee K. (2009). Prospects of carbon nanomaterials in VLSI for interconnections and energy storage, in: EOS/ESD Symposium, IEEE, pp. 1–10.

[32]   Johnston, D.E. (2005). Electronic devices based on purified carbon nanotubes grown by high-pressure decomposition of carbon monoxide. Nature Materials, 4, pp. 589–592.

[33]   Wong, E.W. (1997). Nanobeam mechanics: elasticity, strength, and toughness of nanorods and nanotubes. Science, 277(5334), pp. 1971–1975.

[34]   Che, J. (2000). Thermal conductivity of carbon nanotubes. Nanotechnology, 11(2), p. 65.

[35]   Yi, W. (1999). Linear specific heat of carbon nanotubes. Physical Review B, 59(14), R9015.

[36]   Hone, J. (1999). Thermal conductivity of single-walled carbon nanotubes. Physical Review B, 59(4), R2514.

[37]   Kitiyanan, B. (2000). Controlled production of single-wall carbon nanotubes by catalytic decomposition of CO on bimetallic Co–Mo catalysts. Chemical Physics Letters, 317(3), pp. 497–503.

[38]   Thess, A. (1996). Crystalline ropes of metallic carbon nanotubes. Science, 273(5274), p. 483.

[39]   Arepalli, S. (2004). Laser ablation process for single-walled carbon nanotube production. Journal of nanoscience and nanotechnology, 4(4), pp. 317–325.

[40]   Jost, O. (2004). Single-walled carbon nanotube diameter. Journal of nanoscience and nanotechnology, 4(4), pp. 433–440.

[41]   Kumar, M. (2010). Chemical vapor deposition of carbon nanotubes: a review on growth mechanism and mass production. Journal of nanoscience and nanotechnology, 10(6), pp. 3739–3758.

[42]   Zhang, H. (2011). Separation and/or selective enrichment of single-walled carbon nanotubes based on their electronic properties. Chemical Society Reviews, 40(3), pp. 1324–1336.

[43]   Ismail, A.F. (2008). A review of purification techniques for carbon nanotubes. Nano, 3(03), pp. 127–143.

[44]   Haddon, R.C. (1988). pi.-Electrons in three dimensiona. Accounts of chemical research, 21(6), pp. 243–249.

[45]   Chen, Z. (2003). Reactivity of the Convex and Concave Surfaces of Single-Walled Carbon Nanotubes (SWCNTs) toward Addition Reactions: Dependence on the Carbon-Atom Pyramidalization. ChemPhysChem, 4(1), pp. 93–97.

[46]   Hamon, M.A. (2001). Effect of rehybridization on the electronic structure of single-walled carbon nanotubes. Journal of the American Chemical Society, 123(45), pp. 11292–11293.

[47]   Niyogi, S. (2002). Chemistry of single-walled carbon nanotubes. Accounts of Chemical Research, 35(12), pp. 1105–1113.

[48]   Zheng, G. (2006). Origin of the linear relationship between CH_2/NH/O-SWCNT reaction energies and sidewall curvature: Armchair nanotubes. Journal of the American Chemical Society, 128(47), pp. 15117–15126.

[49]   Lu, X. (2003). A theoretical exploration of the 1, 3-dipolar cycloadditions onto the sidewalls of (n, n) armchair single-wall carbon nanotubes. Journal of the American Chemical Society, 125(34), pp. 10459–10464.

[50]   Park, H. (2005). Distinct properties of single-wall carbon nanotubes with monovalent sidewall additions. Nanotechnology, 16(6), p. 635.

[51]   Joselevich, E. (2004). Electronic structure and chemical reactivity of carbon nanotubes: a chemist's view. ChemPhysChem, 5(5), pp. 619–624.

[52]   Cheng, F. (2006). Noncovalent functionalization and solubilization of carbon nanotubes by using a conjugated Zn–porphyrin polymer. Chemistry - A European Journal, 12, pp. 5053–5059.

[53]   Del Carmen Gimenez-Lopez, M. (2011). Functionalised endohedral fullerenes in single-walled carbon nanotubes. Chemical Communications, 47(7), pp. 2116–2118.

[54]   Abi, T.G. (2012). Proton transfer reactions in carbon nanotubes endohedrally functionalized with selected polar amino acid sidechains. Chemical Physics, 405, pp. 107–116.

[55]   Bamoharram, F.F. (2014). Endohedral functionalisation of multi-wall carbon nanotubes by acidic cesium salt of Preyssler in nanosize. IET Micro & Nano Letters, 9(3), pp. 198–201.

[56]   Novoselov, K.S. (2004). Electric field effect in atomically thin carbon films. Science, 306(5696), pp. 666–669.

[57]   Abbott's, I. E. (2007). Graphene: exploring carbon flatland. Physics today, 60(8), p. 35.

[58]   Randviir, E.P. (2014). A decade of graphene research: production, applications and outlook. Materials Today, 17(9), pp. 426–432.

[59]   Kelly, B.T. (1981). Physics of graphite.

[60]   Novoselov, K.S.A. (2005). Two-dimensional gas of massless Dirac fermions in graphene. nature, 438(7065), pp. 197–200.

[61]   Eda, G. (2008). Large-area ultrathin films of reduced graphene oxide as a transparent and flexible electronic material. Nature nanotechnology, 3(5), pp. 270–274.

[62]   Blake, P. (2008). Graphene-based liquid crystal device. Nano letters, 8(6), pp. 1704–1708.

[63]   Nair, R.R. (2008). Fine structure constant defines visual transparency of graphene. Science, 320(5881), pp. 1308–1308.

[64]   Lee, C. (2008). Measurement of the elastic properties and intrinsic strength of monolayer graphene. science, 321(5887), pp. 385–388.

[65]   Gómez-Navarro, C. (2008). Elastic properties of chemically derived single graphene sheets. Nano letters, 8(7), pp. 2045–2049.

[66]   Soldano, C. (2010). Production, properties and potential of graphene. Carbon, 48(8), pp. 2127–2150.

[67]   Hummers Jr, W.S. (1958). Preparation of graphitic oxide. Journal of the American Chemical Society, 80(6), pp. 1339–1339.

[68]   Schniepp, H.C. (2006). Functionalized single graphene sheets derived from splitting graphite oxide. The Journal of Physical Chemistry B, 110(17), pp. 8535–8539.

[69]   Stankovich, S. (2007). Synthesis of graphene-based nanosheets via chemical reduction of exfoliated graphite oxide. Carbon, 45(7), pp. 1558–1565.

[70]   Liu, L.H. (2010). Derivatization of pristine graphene with well-defined chemical functionalities. Nano letters, 10(9), pp. 3754–3756.

[71]   Han, J. (2010). Functionalization of carbon nanotubes and other nanocarbons by azide chemistry. Nano-Micro Letters, 2(3), pp. 213–226.

[72]   Salice, P. (2014). An insight into the functionalisation of carbon nanotubes by diazonium chemistry: Toward a controlled decoration. Carbon, 74, pp. 73–82.

[73]   Melai, B. (2016). A graphene oxide pH sensor for wound monitoring. Engineering in Medicine and Biology Society (EMBC), 38th Annual International Conference of the IEEE, Orlando (USA), 16-20 Agosto.

[74]   Keana, J.F. (1990). New reagents for photoaffinity labeling: synthesis and photolysis of functionalized perfluorophenyl azides. The Journal of Organic Chemistry, 55(11), pp. 3640–3647.

[75]   Mamane, V. (2014). Chemi-vs physisorption in the radical functionalization of single-walled carbon nanotubes under microwaves. Beilstein journal of nanotechnology, 5(1), pp. 537–545.

[76]   Zhang, W. (2009). Modular functionalization of carbon nanotubes and fullerenes. Journal of the American Chemical Society, 131(24), pp. 8446–8454.

[77]   Wepasnick, K.A. (2010). Chemical and structural characterization of carbon nanotube surfaces. Analytical and Bioanalytical Chemistry, 396(3), pp. 1003–1014.

[78]   Ferrari, A.C. (2007). Raman spectroscopy of graphene and graphite: disorder, electron–phonon coupling, doping and nonadiabatic effects. Solid state communications, 143(1), pp. 47–57.

[79]   Bokobza, L. (2012). Raman spectroscopic characterization of multiwall carbon nanotubes and of composites. Express Polymer Letters, 6(7), pp. 601–608.

[80]   Dresselhaus, M.S. (2005). Raman spectroscopy of carbon nanotubes. Physics reports, 409(2), pp. 47–99.

[81]   Ferreira, F.V. (2016). Functionalizing Graphene and Carbon Nanotubes: A Review. Springer. DOI 10.1007/978-3-319-35110-0

[82]   Giambastiani, G. (2011). Functionalization of multiwalled carbon nanotubes with cyclic nitrones for materials and composites: addressing the role of CNT sidewall defects. Chemistry of Materials, 23(7), pp. 1923–1938.

[83]   Ghini, G. (2009). Can nitrones functionalize carbon nanotubes?. Chemical Communications, 46(2), pp. 252–254.

[84]   Grassi, G. (2012). A facile and ecofriendly functionalization of multiwalled carbon nanotubes by an old mesoionic compound. Chemical Communications, 48(54), pp. 6836–6838.

[85]   Falk, J.E. (1964). Porphyrins and metalloporphyrins (Vol. 2, pp. 72–93). Amsterdam: Elsevier.

[86]   Gouterman, M. (1961). Spectra of porphyrins. Journal of Molecular Spectroscopy, 6, pp. 138–163.

[87]   Murakami, H. (2003). Noncovalent porphyrin-functionalized single-walled carbon nanotubes in solution and the formation of porphyrin–nanotube nanocomposites. Chemical Physics Letters, 378(5), pp. 481–485.

[88]   Adler, A.D. (1967). A simplified synthesis for meso-tetraphenylporphine. The Journal of Organic Chemistry, 32(2), 476–476.

[89]   He, C. (2010). Turn on fluorescence sensing of vapor phase electron donating amines via tetraphenylporphyrin or metallophenylporphrin doped polyfluorene. Chemical Communications, 46(40), pp. 7536–7538.

[90]   Basiuk, E.V. (2007). Noncovalent functionalization of carbon nanotubes with porphyrins: meso-tetraphenylporphine and its transition metal complexes. Journal of nanoscience and nanotechnology, 7(4-5), pp. 1530–1538.

[91]   Banerjee, K. (2009, August). Prospects of carbon nanomaterials in VLSI for interconnections and energy storage. In EOS/ESD Symposium, 2009 31st (pp. 1–10). IEEE.

[92]   Johnston, D.E. (2005). Electronic devices based on purified carbon nanotubes grown by high-pressure decomposition of carbon monoxide. Nature Materials, 4(8), pp. 589–592.

[93]   Friddle, R.W. (2007). Single functional group interactions with individual carbon nanotubes. Nature nanotechnology, 2(11), pp. 692–697.

[94]   Potyrailo, R.A. (2012). Battery-free radio frequency identification (RFID) sensors for food quality and safety. Journal of agricultural and food chemistry, 60(35), pp. 8535–8543.

[95]   Smits, E. (2012). Development of printed RFID sensor tags for smart food packaging, 14th International Meeting on Chemical Sensors, Germany, pp. 403–406.

[96]   Occhiuzzi, C. (2011). RFID passive gas sensor integrating carbon nanotubes. IEEE Transactions on Microwave Theory and Techniques, 59, pp. 2674–2684.

[97]   Azzarelli, J.M. (2014). Wireless gas detection with a smartphone via rf communication. Proceedings of the National Academy of Sciences, 111(51), pp. 18162–18166.

[98]   Chen, E.X. (2014). Highly selective and sensitive trimethylamine gas sensor based on cobalt imidazolate framework material, ACS Applied Materials & Interfaces, 6, pp. 22871–22875.

[99]   Mitsubayashi, K. (2004). Trimethylamine biosensor with flavin-containing monooxygenase type 3 (FMO3) for fish-freshness analysis, Sensors and Actuators B: Chemical., 103, pp. 463–467.

[100]   Cho, W.S. (2005). Multiwall carbon nanotube gas sensor fabricated using thermomechanical structure. IEEE electron device letters, 26(7), pp. 498–500.

[101]   Rizzo, G. (2011). Synthesis, Characterization, and Ammonia Sensing Properties of Vanadium Pentoxide Nanocrystals. In Sensors and Microsystems (pp. 131-136). Springer Netherlands.

Publications

Baldoli[¥], T. Mazzocchi[¥], C. Paoletti, L. Ricotti, P. Salvo, V. Dini, C. Laschi, F. Di Francesco, A. Menciassi, Pressure mapping with textile sensors for compression therapy monitoring, Proceedings of the Institution of Mechanical Engineers, Part H: Journal of Engineering in Medicine, 230(8) (2016), pp. 795-808.

 [¥] These authors contributed equally to this work

B. Melai, P. Salvo, N. Calisi, L. Moni, A. Bonini, C. Paoletti, T. Lomonaco, V. Mollica, R. Fuoco, F. Di Francesco, A graphene oxide pH sensor for wound monitoring, 2016 38th Annual International Conference of the IEEE Engineering in Medicine and Biology Society (EMBC), Orlando, FL, USA, 16-20 August 2016, pp. 1898-1901.

N. Calisi, P. Salvo, B. Melai, C. Paoletti, A. Pucci, F. Di Francesco, Effects of thermal annealing on SEBS/MWCNT temperature-sensitive nanocomposites for the measurement of skin temperature, Materials Chemistry and Physics, 186 (2017), pp. 456-461.

P. Salvo, N. Calisi, B. Melai, V. Dini, C. Paoletti, T. Lomonaco, A. Pucci, F. Di Francesco, A. Piaggesi, M. Romanelli, Temperature- and pH-sensitive wearable materials for monitoring foot ulcers, International Journal of Nanomedicine, 12 (2017), pp. 949-954.

P. Salvo, N. Calisi, B. Melai, B. Cortigiani, M. Mannini, A. Caneschi, G. Lorenzetti, C. Paoletti, T. Lomonaco, A. Paolicchi, I. Scataglini, V. Dini, M. Romanelli, R. Fuoco and F. Di Francesco, Temperature and pH sensors based on graphenic materials, Biosensors and Bioelectronics, 91 (2017), pp. 870-877.

Manuscripts submitted to scientific journals

C. Paoletti, M. He, P. Salvo, A. Pucci, T.M. Swager, F. Di Francesco, Room temperature amine sensors enabled by sidewall functionalization of carbon nanotubes, Sensors and Actuators B: Chemical.

P. Salvo, B. Melai, N. Calisi, C. Paoletti, F. Bellagambi, A. Kirchhain, M. G. Trivella, R. Fuoco, F. Di Francesco, Graphene-, graphene oxide- and reduced graphene oxide-based devices to measure pH, Biosensors and Bioelectronics, Review Article.

Patents

F. Di Francesco, N. Calisi, B. Melai, L. Moni, C. Paoletti, P. Salvo, Un sensore di misurazione del pH in grafene ossido, Domanda brevetto italiano FI2015A000130, depositata il 05/05/2015.

Abstract in congresses and posters

F. Di Francesco, B. Melai, N. Calisi, P. Salvo, C. Paoletti, V. Dini, M. Romanelli, G. Matzeu, A. Giuliani, A. Pucci, "Nanocomposite-based wearable temperature sensors", NanotechItaly 2014, Venice 26-28 November 2014.

P. Salvo, B. Melai, S. Bianchi, N. Calisi, V. Dini, M. Romanelli, V. Castelvetro, C. Paoletti, C. Politino, F. Di Francesco, Non-invasive sensors for wound monitoring and therapy, 37th Annual International Conference of the IEEE Engineering in Medicine and Biology Society, Milano, August 25-29 2015. (Poster).

N. Calisi, B. Melai, P. Salvo, C. Paoletti, S. Bianchi, L. Moni, C. Politino, A. Pucci, V. Castelvetro, V. Dini, M. Romanelli, R. Fuoco and F. Di Francesco,

Wearable sensors for the remote monitoring of chronic wounds, EuroAnalysis 2015, Bordeaux, 6-10 September 2015 (Orale).

N. Calisi, B. Melai, P. Salvo, C. Paoletti, L. Moni, C. Politino, A. Ceccarini and F. Di Francesco, Disposable sensors for the remote monitoring of chronic wounds, Pittcon 2016, March 6 - 10, 2016 Georgia World Congress Center, Atlanta, USA.

N. Calisi, B. Melai, P. Salvo, C. Paoletti, R. Fuoco, V. Mollica and F. Di Francesco, Graphene and graphene oxide sensors for monitoring chronic wounds, CIMTEC 2016, 5-9 Giugno 2016, Perugia, Italy (Orale).

B. Melai, P. Salvo, N. Calisi, C. Paoletti, V. Dini, M. Romanelli, A. Paolicchi, V. Castelvetro, R. Fuoco and F. Di Francesco, A smart wearable and autonomous negative pressure device for wound monitoring, CIMTEC 2016, 5-9 Giugno 2016, Perugia, Italy (Poster).

N. Calisi, B. Melai, C. Paoletti, P. Salvo, A. Pucci, V. Mollica, A. Ceccarini, A. Paolicchi, S. Bianchi, V. Castelvetro, R. Fuoco and F. Di Francesco, Flexible sensors for a continuous monitoring of chronic wounds, Biosensors 2016, Goteborg (Oral).

N. Calisi, B. Melai, C. Paoletti, P. Salvo, A. Pucci, V. Mollica, A. Ceccarini, A. Paolicchi, S. Bianchi, V. Castelvetro, R. Fuoco and F. Di Francesco, Flexible sensors for a continuous monitoring of chronic wounds, Biosensors 2016, Goteborg (Oral).

B. Melai, P. Salvo, N. Calisi, L. Moni, A. Bonini, C. Paoletti, T. Lomonaco, V. Mollica, R. Fuoco, F. Di Francesco, A graphene oxide pH sensor for wound monitoring, 38th Annual International Conference of the IEEE Engineering in Medicine and Biology Society (EMBC'16), August 16-20, 2016, Orlando, USA. (Conference paper, Oral).

B. Melai, P. Salvo, N. Calisi, C. Paoletti, E. Herrera, V. Dini, M. Romanelli, A. Paolicchi, V. Mollica, A. Ceccarini, R. Fuoco, F. Di Francesco, Disposable sensors for the continuous monitoring of temperature and pH of the wound bed, 5th Congress of WUWHS, Florence, September 25-29 2016 (Abstract, Oral).

C. Paoletti, P. Salvo, N. Calisi, B. Melai, A. Pucci, F. Di Francesco, Room temperature chemoresistive sensor for the detection of ammonia and trimethylamine, XXVI Congresso della Divisione di Chimica Analitica Italiana, 18-22 Settembre 2016, Giardini Naxos (Abstract, Poster).

B. Melai, N. Calisi, P. Salvo, C. Paoletti, E. Herrera, V. Mollica, R. Fuoco and F. Di Francesco, Flexible, biocompatible and disposable ph and temperature sensors based on carbon nano-structured materials, XXVI Congresso della Divisione di Chimica Analitica Italiana, 18-22 Settembre 2016, Giardini Naxos (Abstract, Oral).

B. Melai, N. Calisi, P. Salvo, C. Paoletti, E. Herrera, A. Kirchhain, V. Mollica, R. Fuoco and F. Di Francesco, SWAN-ICARE: a smart wearable and autonomous negative pressure device for wound monitoring, XXVI Congresso della Divisione di Chimica Analitica Italiana, 18-22 Settembre 2016, Giardini Naxos (Abstract, Poster).

Schools and international stages

- Scuola Mario Farina 2014 XXXV edizione "Caratterizzazione di materiali polimerici: tecniche per polimeri in soluzione". Gargnano (BS), 19-23 May 2014.

- XVIII Scuola Nazionale di Scienza e Tecnologia dei Materiali "Carbon-based nano-structured materials: graphene as a new player. Technologies, characterization, applications". Ischia (NA), 16-20 July 2014.

- ISMEC2016 International symposium of metal complexes. Barcelona (Spain), 7-10 June 2016.

- XXVI Congresso della Divisione di Chimica Analitica della Società Chimica Italiana (SCI). Giardini Naxos (ME), 18-22 September 2016.

In the framework of the MIT-UNIPI project I spent 6 months at the Massachusetts Institute of Technology (MIT) working as visiting scientist.